EXAFS Studies of La-Ga Metallic Glasses

Thesis by

David Verge Baxter

In Partial Fulfillment of the Requirements

for the Degree of

Doctor of Philosophy

California Institute of Technology

Pasadena, California

1984

(submitted May 8, 1984)

To the Memory of

Howard B. Tye

ACKNOWLEDGEMENTS

The appreciation that I have for the support and encouragement provided by Professor William L. Johnson throughout the course of this work cannot be overstated. Bill's keen physical insight, constant production of new ideas, and even his great outside jump shot have helped to make the last four years a truly rewarding and enjoyable educational experience. The contribution of Dr. Art Williams to this work has also been one which is difficult to exaggerate though not to assess. Truly this work would not have been possible had it not been for his fabulous spectrometer and his earlier diffraction experiments.

Various members of the third floor Keck group, both past and present, have also been most helpful. In particular discussions with Professor Pol Duwez, Dr. Mike Tenhover, Madhav Mehra, and Bob Schulz have constantly served to remind me that there is more to metallic glasses than X-ray edges, and that there is more to life than metallic glasses! The technical support provided by Concetto Geremia was invaluable and very much appreciated . The work presented in chapter 5 of this thesis owes a great deal to discussions with Craig Lindberg and Lowell Hazelton, and I am very grateful to both. In preparing this manuscript the aid provided by Dr. Karl Unruh, Madhav Mehra, and especially Mrs. Angela Bressan was instrumental and is most gratefully acknowledged.

I must also thank my parents and siblings for their constant understanding and support of the black sheep of the family. Finally the friendship and stability of Bob and Susie Cave and Claudia Troesch during the trial by fire that was candidacy is most appreciated.

Financial support during the course of this work was received from NSERC of Canada, Standard Oil, the United States Department of Energy, and Bell Laboratories and was greatly appreciated.

ABSTRACT

Extended X-ray Absorption Fine Structure (EXAFS) measurements have been performed on the Ga edge of several La-Ga metallic glasses, using an in-lab spectrometer. The results obtained are compared with earlier experiments on the same materials where X-ray diffraction and isomorphous substitution were used to determine partial pair correlation functions. This is, therefore, a rigorous test of the EXAFS technique when applied to strongly disordered systems, such as metallic glasses. It is found that the glass $La_{80}Ga_{20}$ has a comparatively simple local Ga environment and that the EXAFS for this glass can be described very well with a single asymmetric shell of La atoms surrounding the Ga. As the Ga concentration is increased, however, it is found that the local Ga environment becomes more complicated. Traditional methods of EXAFS analysis, based on nonlinear least squares curve fitting, are then unable to distinguish between several different possible local Ga environments. Finally a new, essentially non-parametric, method of analyzing EXAFS data is discussed and tests are conducted to demonstrate the circumstances under which this new method could prove advantageous over the more traditional methods.

CONTENTS page

LIST OF TABLES

LIST OF FIGURES

1 INTRODUCTION

1.1 MOTIVATION

From the time that the early hominids first started to fashion Acheulian tools, mankind has had an abiding interest in the structure of the materials he uses. With the development of modern science this interest has gone beyond such practical problems as the construction of a better hand axe, to more esoteric questions regarding the nature of the fundamental building blocks of matter and the way that these are arranged inside various materials. More recently however these questions, which had been primarily of academic interest, have become essential to the continued development of so-called "high technology" industries, and an increased fundamental understanding of the properties of materials is once again needed for the continued improvement of our life style.

The understanding of the material properties of any solid must start with an understanding of its atomic structure. In crystalline materials, X-ray or neutron diffraction measurements can provide exceptionally detailed information about the atomic structure. However materials of practical interest are rarely, if ever, perfect crystals, and although diffraction can still provide useful information about departures from perfect crystallinity, often simple diffraction experiments fail to provide a complete structural picture. As a consequence of this, therefore, additional structural probes may be required in order to obtain the structural information desired.

An important class of materials for which diffraction experiments provide incomplete information on the atomic structure are the metallic glasses, or more generally, amorphous metals. This thesis

will discuss a particular structural probe which has recently been used as a technique to compliment diffraction experiments in studies on a number of materials, metallic glasses among them. The technique in question is known as Extended X-ray Absorption Fine Structure (or EXAFS) spectroscopy, and is introduced in chapter 2. The following sections of this first chapter will introduce the reader to the field of metallic glasses in order to provide a understanding of the types of questions which EXAFS might be able to answer, as well as pointing out why diffraction techniques are inadequate for answering many of these questions.

1.2 METALLIC GLASSES

Amorphous metals are solids which have the usual metallic properties, but which possess no long range atomic periodicity, as is found in the more common crystalline metals. A sub-class of this type of material is formed by the so-called metallic glasses, which are distinguished from the broader class by the fact that they are produced by rapidly quenching an equilibrium liquid to a temperature at which the sample becomes configurationally frozen.

The first metallic glass was produced by Duwez and co-workers almost 25 years ago when a Au-Si alloy was "splat-quenched" on a copper substrate[1.1]. An X-ray diffraction pattern taken on the resulting flakes of material using a Debye-Scherrer camera showed only a broad diffuse band, rather than the sharp rings expected for a crystalline sample. An example of the diffraction pattern obtained from such a material is given in figure 1.1.

While a diffraction pattern such as that shown in figure 1.1

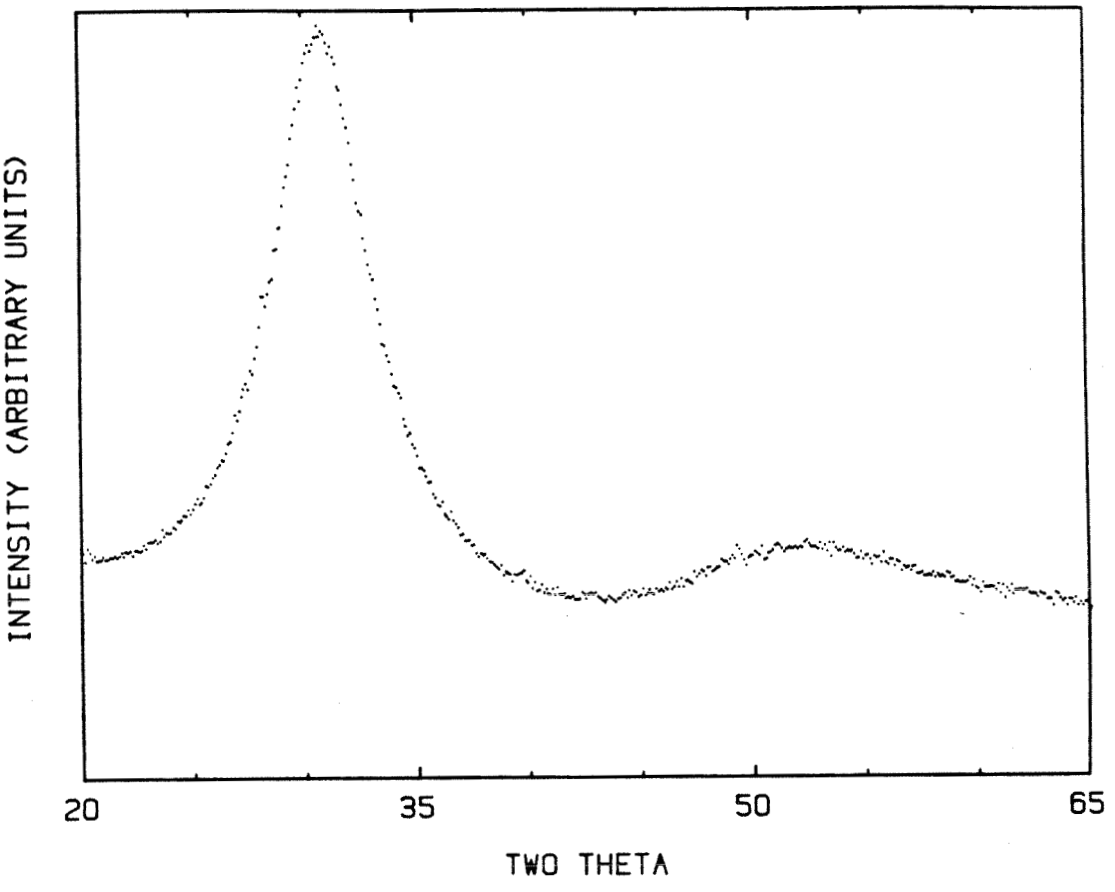

Figure 1.1 X-ray diffraction pattern for an amorphous $La_{76}Ga_{24}$ alloy. Cu K_{α} radiation was used and the scattering angle is given in degrees.

clearly indicates that the sample contains no significant crystalline domains, it does not provide a great deal of information about the structure which is present in the sample. As a result of this lack of detailed information early attempts to describe the structure of metallic glasses centred on two quite different pictures. The first of these considered the glass to be a "failed crystal", which was composed of an assembly of very small, but well defined, micro-crystallites. The second view, on the other hand considered the glass to be a configurationally frozen liquid. Both of these models would produce a diffraction pattern consistent with the broad band seen in figure 1.1, although the width of the observed band puts an upper bound on the size (s) of any micro-crystallites which might be present in the sample, through the Scherrer formula[1.2]:

$$s \approx \frac{0.9\ \lambda}{\Delta\theta_B \cos\theta_B} \tag{1.1}$$

Using this formula, (with $\Delta\theta_B$ being the measured width of the diffraction peak), diffraction patterns such as figure 1.1 place an upper bound of 30 to 50 A on the size of the micro-crystals.

If a far more detailed diffraction pattern is taken, the interference function (I(k) ; see section 1.3 and/or reference 1.3) for the scattering event may be computed (if X-rays are used then the effects of Compton scattering and the k dependance of the atomic form factor must first be properly accounted for in order to accurately compute I(k)[1.3]). The measured I(k) can then be used for a more detailed comparison with a theoretical I(k) calculated for a given model of the structure. Cargill performed such an analysis of the

I(k) measured for amorphous Ni-P alloys and was thereby able to show that the micro-crystalline models for the glass structure were incompatible with the experimental results[1.4]. Additionally, from the measured structure factor he was able to compute the Radial Distribution Function (or RDF) for the materials by taking the Fourier transform of the reduced interference function [1.3] (see section 1.3 below). The resulting RDF compared favourably with that computed for a Dense Random Packing of Hard Spheres (or DRPHS) model, originally proposed for liquids by Bernal and his students [1.5] as shown in figure 1.2. As a result of this comparison the DRPHS has been taken as the canonical first approximation to the atomic structure of metallic glasses.

There are, however, several objections to a dense random packing model for the structure of these materials. In the first place, all metallic glasses are alloys of at least two atomic species, usually of considerably disparate radii. This objection has been addressed more recently by considering packings of spheres of two different sizes [1.6], however certain aspects of the phenomenology of the materials are still unanswered by such models. An example of this is related to the universal occurrence of a deep eutectic in the equilibrium alloy phase diagram near the glass forming region of these systems. This indicates a negative heat of mixing in the liquid alloy as compared with the heat of mixing in competing crystalline phases, and is completely ignored by models based on a random packing of hard spheres, irrespective of the size distribution used. More recently, the formation of apparently amorphous metallic films by the solid state reaction of multilayer sandwiches of pure metallic elements

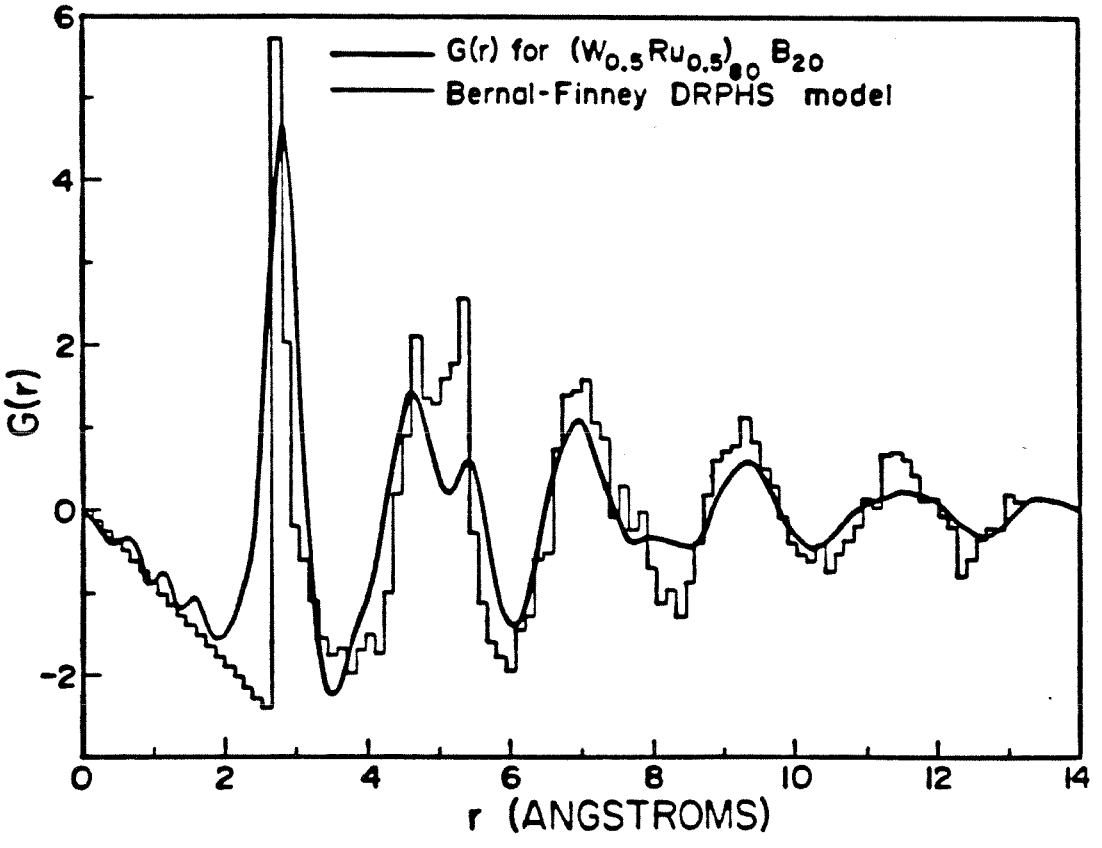

Figure 1.2 Comparison of a Radial Distribution Function measured for a $(W_{0.5}Ru_{0.5})_{80}B_{20}$ metallic glass with an appropriately scaled DRPHS model. (Taken from reference 1.3).

indicates[1.7] that the local atomic arrangement of these materials cannot be truly random, but rather must be, under certain circumstances, energetically favourable, even with respect to certain crystalline morphologies. Thus the chemistry of the constituent atoms in the glass must also be important, and must be understood for any general description of the properties of these materials.

In addition to these general objections, random packing models also fail to predict specific results found in experiments. Specifically, the experimentally observed density is invariably much higher than is the density of any of the hard sphere packing models proposed to this date. Also the position and relative heights of various peaks in experimental RDF's differ somewhat from those found in the most detailed hard sphere packing models.

The introduction of soft interatomic potentials in order to allow relaxation of the structure obtained in a hard sphere packing has resulted in an improvement in the agreement with experiment, although the agreement is still not entirely satisfactory [1.3]. Yet another alternative to spherical packing models has been the so-called stereochemical models. The two most prominent of these are the trigonal prismatic model of Gaskell[1.8] and the icosahedral microcluster model of Briant and Burton[1.9]. The former of these suggests that the local arrangement of atoms in the so-called metal-metalloid glasses is dominated by a trigonal prismatic arrangement of the larger metal atoms about the smaller metalloid atom. The motivation for this model is the ubiquitous occurrence of such an arrangement of atoms in the equilibrium crystal structures of the alloy systems which form this kind of glass. The icosahedral microcluster model on the other hand

is suggested by the fact that isolated assemblies of small numbers of atoms have been found to exhibit an energetic preference for such an arrangement. Furthermore the presence of five-fold symmetry in such a cluster precludes the formation of a crystal based on such a structural unit. This latter concept of the frustration of the formation of a crystalline lattice by the local atomic configuration has been extended more recently into quite elegant and complex topological theories of glass structure[1.10]. However space does not allow the discussion of such theories here.

One question regarding the structure of metallic glasses is not directly addressed by any of the aforementioned topological models (with the exception of the picture proposed by Gaskell), this being the question alluded to earlier of how the chemically different atomic species arrange themselves with respect to each other on whatever topological network may be present in the material. Given the affinity the constituent atoms generally have for each other (as evidenced by the deep eutectics in the phase diagrams), this question of Chemical Short Range Order (CSRO) is just as important as the Topological Short Range Order (TSRO) discussed above in the determination of the physical properties of the material.

Indeed, it has been suggested that a number of the observed phenomena involving the relaxation behaviour of metallic glasses could be explained in terms of changes in the CSRO of the material[1.11]. Specific observations are the changes in resistivity of many metallic glasses upon annealing at temperatures below that required for spontaneous crystalization and the change in the lifetime observed in positron annihilation experiments upon similar annealing treatments.

The reversible behaviour of the Curie temperature of certain ferromagnetic metallic glasses with various annealing treatments[1.12] has also been suggested as evidence for changes in the local short range order in these materials. In order to determine whether or not these observations are in fact due to changes in the CSRO it is necessary to have a method for measuring the degree of such order in a given sample.

Another set of observations which appear to require some knowledge of the CSRO in the material for their understanding are some of the changes seen in material properties when the composition of the glass is varied. Specific examples of this type of effect are seen in the resistivity of Pd-Ni-P as a function of phosphorus concentration and the small, but abrupt, change seen in the Debye temperature of La-Ga glasses near 24% Ga. As with the relaxation phenomena discussed earlier it would be most advantageous to have a structural probe which is capable of detecting and describing any changes in the local structure which might accompany these changes in material properties.

Keeping in mind that the question of whether the above described changes are related to changes in the chemical or topological structure of the material, the next section addresses the problem of how the chemical short range order may be measured.

1.3 MEASUREMENT OF CSRO

As indicated in the previous section, one of the questions which first presents itself when a metallic glass is considered is the presence or absence of chemical short range order in the material, and the question of how this order may change as a function of annealing

treatment or variation in composition of the glass. In order to understand why it is difficult to obtain this kind of information from diffraction experiments it is useful to consider the general expression for the interference function for diffraction of X-rays by a non-crystalline, multi-component assembly of atoms. This expression is given in reference 1.3 as:

$$(1.2) \qquad I(k) = 1 + \frac{1}{k} \sum_{ij} W_{ij}(k) \int_0^\infty 4\pi R \, (\rho_{ij}(R)/C_j - \rho_o) \sin kR \, dR$$

In the above formula the quantities $\rho_{ij}(R)$ give the atomic density of atoms of type j at a distance R from an atom of type i, and the factors W_{ij} describe the effective contribution of pairs of type i-j to the observed diffraction. The other variables in the expression are the wave vector of the momentum transfer in the scattering event (k), the average atomic density of the sample (ρ_o), and the concentration of species j (c_j). For the specific case of X-ray diffraction the factors W_{ij} are given by the expression:

$$(1.3) \qquad W_{ij}(k) = C_i C_j \frac{f_i(k) \, f_j^*(k)}{|\langle f(k) \rangle|^2}$$

Here $f_i(k)$ is the atomic form factor for the species i.

The form given for the interference function (equation 1.2) was chosen because the W_{ij} are approximately independent of k. For neutron scattering an analogous expression may be given but in that case the approximation of constant W_{ij} is much more exact.

In order to address the question of CSRO, the quantities needed from equation (1.2) are the $\rho_{ij}(R)$. Often it is more convenient to introduce the so-called reduced partial pair correlation functions, defined by the relation:

$$G_{ij}(R) = 4\pi R\ (\rho_{ij}(R)/C_j - \rho_o) \tag{1.4}$$

In analogy to these quantities, the partial reduced interference function may be introduced in order to write the key equations in a more compact form.

$$I(k) = 1 + \sum_{ij} W_{ij}(k)\ i_{ij}(k) \tag{1.5}$$

where:

$$i_{ij}(k) = \frac{1}{k} \int_0^\infty G_{ij}(R)\ \sin kR\ dR \tag{1.6}$$

This equation makes it obvious that a single experiment is able to provide only a complicated linear combination of the various partial pair correlation functions, not the individual functions themselves. However, the same equation indicates how the individual correlation functions may be obtained by performing several different diffraction experiments, such that the W_{ij} vary from one experiment to the next, while the $i_{ij}(k)$ remain the same. Considering a binary alloy for the moment, if three different scattering experiments are performed then three different I(k) functions will be found. Each of these will be given by a linear combination of the same three

functions $i_{ij}(k)$ ($i_{ij}(k)$ and $i_{ji}(k)$ are simply related to each other and therefore are not independent) with different weights in each case. Provided the matrix relating these three different total interference functions to the three independent partial interference functions is sufficiently well conditioned, this matrix may be inverted and the $i_{ij}(k)$ may be determined for each k. From these the individual $G_{ij}(R)$'s may be found using equation (1.6).

The best way to accomplish this deconvolution of the partial interference functions is by performing neutron scattering experiments on several different samples which have been identically prepared, with the exception that the isotopic distributions of the constituent elements used varies from sample to sample. As a result of this isotopic variation from one sample to the next, the various partial correlation functions will be weighted differently in the various samples. This type of experiment can be very expensive however, since it requires the purchase of rather substantial amounts of isotopically pure elements. In addition not all elements have an appropriate selection of isotopes with sufficiently different scattering lengths.

As an alternative to the the above mentioned technique of isotopic substitution it is also possible to combine neutron and X-ray scattering experiments (although it is not possible to combine either of these with electron diffraction [1.12]). More recently the introduction of synchrotron radiation sources has allowed the small changes in X-ray form factors for photons whose energy is near that of one of the absorption edges of the scattering atom to provide independent diffraction experiments simply by tuning the radiation taken from the intense synchrotron source to appropriately selected energies[1.13].

This technique is still in its infancy, however it holds great promise for being quite powerful in the future, particularly as the sources become more intense. This alternative has the distinct advantage of being applicable to a very wide variety of materials, although its ability to determine the environment of very light metalloid atoms such as B and Si is quite limited.

A final alternative, and one that has been employed in one series of experiments performed in this lab, is to select a number (two or three) of atoms which are very similar chemically, but differ quite markedly in their atomic number (and therefore in their X-ray form factors)[1.3]. This technique is called "isomorphous substitution" and was applied to La based metallic glasses, where Au, Ga or Al was used as the alloying element. It will be recalled from the discussion of the previous section that one of these three alloys (La-Ga) exhibits a marked change in the Debye temperature as the composition varies around 24% Ga. The results obtained in this earlier study which are most important for the current discussion are summarized in table 1.1. The relevant parameters are the composition (x), the number of La atoms about each Ga (N_{La}), and the postition and full width at half maximum of the first peak in the Ga-La distribution function (R_{La} and ΔR_{La} respectively).

TABLE 1.1

Selected results from isomorphous substitution X-ray diffraction experiments on La based metallic glasses.

x	N_{La}	R_{La}	ΔR_{La}
20	7.8 ± 0.9	3.27 ± 0.05	0.13 ± 0.01
24	9.7 ± 0.9	3.22 ± 0.05	0.14 ± 0.01
28	9.6 ± 0.9	3.25 ± 0.05	0.15 ± 0.01

In all cases the values given in this table refer to quantities seen for the local environment of the M atoms in the material, where M is Al, Au or Ga. The full width at half maximum of the measured peak in the partial pair distribution function is denoted by R_{La} in this table. It should be noted that in this experiment no evidence was seen for any M-M nearest neighbours at any of the three compositions studied (the experiment puts an upper bound on the coordination number of M atoms around other M atoms at 1). However, due to the small atomic number of Ga and Al with respect to La, the information regarding M-M coordinations comes almost exclusively from the La-Au glasses and so it is possible that a slightly different picture prevails in the other two systems.

In addition to the above noted evidence for strong chemical short range order in these La-M glasses, table 1.1 also presents evidence for a structural change near the composition where the anomaly in the Debye temperature was seen. This then demonstrates that this kind of detailed structural study can indeed provide information of the type

which the previous section indicated might be useful for the understanding of various phenomena associated with metallic glasses. However, it is clear that a large amount of work is needed in order to obtain this kind of information using diffraction techniques. The performance of several time consuming experiments at a national facility on numerous samples with slightly different compositions or thermal history is a very laborious task.

As mentioned previously the technique of EXAFS spectroscopy holds some promise for being able to provide information similar to that obtained from multiple diffraction experiments, but hopefully requiring somewhat less involved experimental work. The remainder of this thesis presents a test of this technique's ability to provide such information through the analysis of spectra collected for samples in the La-Ga glass system. In chapter 4 the results obtained using the EXAFS technique are compared with those given in table 1.1. However first the necessary background theory and experimental details are outlined in the following two chapters.

2 THEORETICAL BACKGROUND

2.1 HISTORY

The appearance of "edges" in X-ray absorption spectra has been known at least since 1908 when Barkla and Sadler conducted experiments using fluorescence radiation from various metals to measure the absorption of "homogeneous X-rays" of various penetrating power (with respect to Al) by certain substances[2.1]. These early experiments were truly remarkable, occuring as they did some 4 years before the discovery of X-ray diffraction in crystals by von Laue[2.2].

Thanks largely to the simple explanation given by Bragg [2.3] for von Laue's discovery, the diffraction phenomenon was soon used to perform X-ray spectroscopy[2.4]. Naturally an early application was to the detailed study of the energy dependence of the absorption of X-rays. It was immediately discovered that the "absorption edges" could be quite complicated when viewed on a fine enough scale. In particular, "secondary edges" were observed on the short wavelength (i.e. high energy) side of the edge. Early explanations of this discovery centred on the excitation of one or more electrons to unoccupied "optical levels" as a result of the absorption event[2.5,2.6]. However later experiments on Ar showed that such explanations did not tell the whole story[2.7]. In these experiments, as well as later ones on metallic vapours it was discovered that the secondary structure existed only for a few tens of eV's beyond the edge at most. In contrast to this, the secondary structure seen in some metallic solids was known to persist up to several hundred eV from the edge. Kronig first proposed an explanation of this more extended structure seen in the solid state in terms of forbidden bands of electron propagation

which would be expected along certain symmetry directions in a crystal[2.8].

The observation of extended structure in the absorption coefficient of molecular species, however, led a number of authors (starting with Kronig himself in 1932[2.9]) to consider theories which would not rely on the long range order of a crystal. These so-called short range order (SRO) theories differ in a fundamental way from the earlier explanations in that they attribute the fine structure to variations in the transition probabilities, whereas the earlier work concentrated on the effect of variations in the final density of states. These SRO theories consider the final state wave function of the photo-electron and how the presence of the coordination shell surrounding the absorbing atom modifies this state from what it would be for absorption by an atom isolated in free space. Until 1970 the most detailed of the SRO theories was given by Kozlenkov[2.10]. He considered the final state to be one which is scattered off of a spherically averaged potential of the neighbouring atoms. This scattered wave will interfere with the outgoing wave function in the region of the initial core state, and this interference is the source of the observed oscillations. Using this picture Kozlenkov was able to derive the following expression for the oscillations.

$$\chi(k) = -\sum_{s} \frac{N_s}{R_s^2} \sin\left[2kR_s + 2\delta_1\right] \tag{2.1}$$

Here the sum is over the various shells of neighbours, which contain N_s atoms at a distance of R_s, k is the wave vector of the photo-electron and $2\delta_1$ is the phase shift imposed on the photo-

electron wave function by the potential of the absorbing atom. Using an expression such as this Kozlenkov was able to reproduce the position of the peaks and valleys of the fine structure measured for Cu metal[2.11]. The agreement obtained for the peak positions was reasonably good, however the overall shape of the calculated spectrum was significantly different from the experimental observation.

The reason for the deficiencies of Kozlenkov's treatment lies primarily in the way it deals with the scattering of the photo-electron. However more sophisticated treatments were not presented until after 1971. In that year Sayers, Stern and Lytle had the insight to realize that the phase shift imposed by the scattering of the photo-electron by the atoms in the solid was nearly linear in k, and therefore the Fourier transform of the "EXAFS" oscillations might provide useful information about the atomic arrangements in the solid. Indeed, they noted that the various peaks observed in the transform corresponded to the various shells of neighbours surrounding the absorbing atom. With this realization, that the observation of the phenomenon might provide useful information, came renewed interest in the explanation of the fundamental physics involved in the absorption event. As a result several elaborate treatments of the problem appeared in the mid-1970's. The more salient features of these more sophisticated treatments will be discussed in the following section.

2.2 MODERN THEORETICAL DESCRIPTION

For all cases of relevance to current experimental work in the field of X-ray absorption, the absorption event itself may be treated

in the dipole approximation.[2.12] This fails to be valid only when the binding energy of the electron being excited is so great that relativistic corrections are needed. At such high energies the experiments become very difficult due to a lack of resolution and photon flux. Therefore, for the purposes of the current work it will be assumed here that the cross section for absorption at a deep lying shell is given by:[2.13]

$$\sigma = 4\pi^2 \alpha \omega \left| \langle i | \hat{\varepsilon} \cdot \underset{\sim}{R} | f \rangle \right|^2 N(\omega) \tag{2.2}$$

When the absorbing atom is isolated the final state will simply be an outgoing spherical wave $|k_o\rangle$, and the cross-section will be a smooth function of k (the final state wave vector). If the absorbing atom has one or more neighbours however, then the final state will be modified in a manner which can be thought of as a scattering event much as envisioned by Kozlenkov. A more rigorous treatment is to note that the final state wave function must satisfy the Lippmann-Schwinger equation (i.e. the integral form of the Schrodinger equation):

$$|f\rangle = |k_o\rangle + G_o^- T^- |k_o\rangle \tag{2.3}$$

Here G_o is the free space propagator and T is the t-matrix describing the interaction of the propagating electron and the atoms in the sample (including both the neighbours and the absorbing atom itself). If this t-matrix is expanded in terms of single site scattering processes then the resulting series for $|f\rangle$ can be inserted back into

(2.2) to give a series expression for the cross-section. To get a useful expression from this process requires a large amount of algebra which will not be reproduced here, however the interested reader is refered to Boland et al.[2.14] for a very readable account. If all multiple scattering terms involving more than one neighbour are ignored then the end result of this algebra is the equation:

$$\sigma \sim \frac{1}{3}|M|^2 - \sum_j |M|^2 \, (\hat{\varepsilon}\cdot\hat{R}_j)^2 \, \frac{1}{kR_j^2} \, \mathrm{Im}\left[f_j(k,\pi)\, e^{2i(kR_j + \delta_1)}\right] \tag{2.4}$$

Here $|M|^2$ is the dipole matrix element between the initial state and the unmodified final state and the sum is over all neighbouring atoms. Consequently $|M|^2$ is proportional to the absorption coefficient expected for a free atom, which, as mentioned earlier, should be a smooth function of k. If this relation between $|M|^2$ and μ_o is used then the above may be rewritten in a more conventional form.

$$\chi(k) := \frac{\mu - \mu_o}{\mu_o} = -\frac{3}{k} \sum_j \frac{(\hat{\varepsilon}\cdot\hat{R}_j)^2}{R_j^2} \, \mathrm{Im}\left[f_j(k,\pi)\, e^{2i(kR_j + \delta_1)}\right] \tag{2.5}$$

This last expression is very similar to the one given by Kozlenkov, except for the presence of the polarization factor and the scattering amplitude. Except for studies of oriented crystals using polarized beams the polarization factor will average out, and consequently this factor will play no role in the work of this thesis. The presence of the scattering amplitude, however, requires some special consideration. The most crucial assumption used in the derivation of equation (2.5) is that the scattering off of the neighbouring atoms

can be treated in an approximation where both the incident and scattered waves have definite momenta (i.e. they are plane waves). This is only a reasonable assumption for reasonably large photo-electron momenta (say $k > 3.5\ A^{-1}$). Below such a value for the momentum the curvature of the photo-electron wave front and the finite size of the scattering atom must be accounted for. However, at lower momenta other problems, not addressed in (2.5), such as many body effects and multiple scattering become important as well. Consequently it is common practice to simply apply (2.5) only to the high k region of the spectrum where it is thought to be reasonably accurate. It is this restriction to the high k regime that is responsible for the "Extended" in the phrase "Extended X-ray Absorption Fine Structure."

There are, however, certain many body effects which must be accounted for in real applications, even though they do not appear in (2.5). These are the effect of relaxation of the other "passive electrons" on the absorbing atom, and the finite lifetime imposed on the final photo-electron state by inelastic interactions with other electrons. The first of these effects may be accounted for mathematically by computing the overlap integral between the states of the passive electrons before and after the creation of the core hole. Physically this corresponds to absorption events involving the shake-up or shake-down of one or more of the passive electrons. If such an event takes place the ionized electron loses coherence and therefore such an event cannot contribute to the interference which produces the fine structure. For this reason when calculated values are used for $|f(k,\pi)|$, equation (2.5) invariably gives an amplitude which is 30 to 50% larger than that observed experimentally. The most common method

for dealing with the second many-body effect mentioned above is to introduce a phenomenological damping term in which the photo-electron is assigned an effective mean free path. Under this assumption the final, useful form of the expression for the EXAFS function is:

$$\chi(k) = -\sum_j \frac{3(\hat{\varepsilon}\cdot\hat{R}_j)^2}{k\,R_j^2} e^{-2R_j/\lambda}\, S_o^2(k)\, |f_j(k,\pi)| \cdot \sin(2kR_j + 2\delta_1 + \phi_j(k)) \tag{2.6}$$

The sum in (2.6) is still over individual atoms, λ is the phenomenological mean free path mentioned earlier and $S_o^2(k)$ is the overlap integral contribution of the passive electrons on the central atom.

As pointed out by Eisenberger and Lengeler [2.15] the mean free path treatment is not an entirely satisfactory way of treating the inelastic effects. This is particularly true for atoms in hard sphere contact such as those which will be discussed in this thesis. Consequently herein the mean free path factor will be incorporated into the two factors $S_o^2(k)$ and $|f(k,\pi)|$ for the remainder of this work. Keeping this in mind the following expression will be taken as the starting point for all future discussions.

$$\chi(k) = -\sum_i \frac{4\pi S'}{k} |f_i(k,\pi)| \int_o^\infty \rho_i(k) \sin(2kR + \alpha_i(k))\, dR \tag{2.7}$$

In this equation the sum is now only over different types of atoms, the atomic density function $\rho_i(R)$ has been introduced in order to establish a connection with the earlier discussion of diffraction experiments in disordered solids, and $\alpha(k)$ has been introduced to combine $2\delta_i + \phi(k)$ into a single term. The most apparent simplifica-

tion of (2.7) over the equivalent expression for diffraction (equation (1.2)) is that there is now only a single summation. This reflects the fact that in an X-ray absorption experiment the central atomic species is known by virtue of the experimenter's choice of photon energy. In addition, however, the fact that $|f(k,\pi)|$ varies significantly with atomic number implies that some information about the various $\rho_i(R)$'s in the summation may be obtained even from just a single absorption experiment. For this reason it was hoped that EXAFS might provide a very powerful tool for the investigation of the local structure of amorphous materials. The discussion will now turn to the manner in which equations such as (2.6) or (2.7) are actually used in extracting information about the material under study.

2.3 BASIC ANALYTICAL PROCEDURES

It must be realized from the outset that the discussion of the previous section was all in terms of a single mechanism for absorption. Naturally, in an actual experiment, any electron whose binding energy is less than that of the incident photon will contribute to the measured absorption coefficient. Hence, once an absorption coefficient has been computed from the measured incident and transmitted intensities, the first stage of the analysis must be to isolate the absorption due only to the event discussed in section 2.2 (i.e. the resonant absorption) from all other events. To accomplish this the absorption coefficient is typically measured from a few hundred eV below the edge of interest, to at least several hundred eV above that edge, as shown in figure 2.1. The pre-edge region defines a trend for the absorption due to all non-resonant

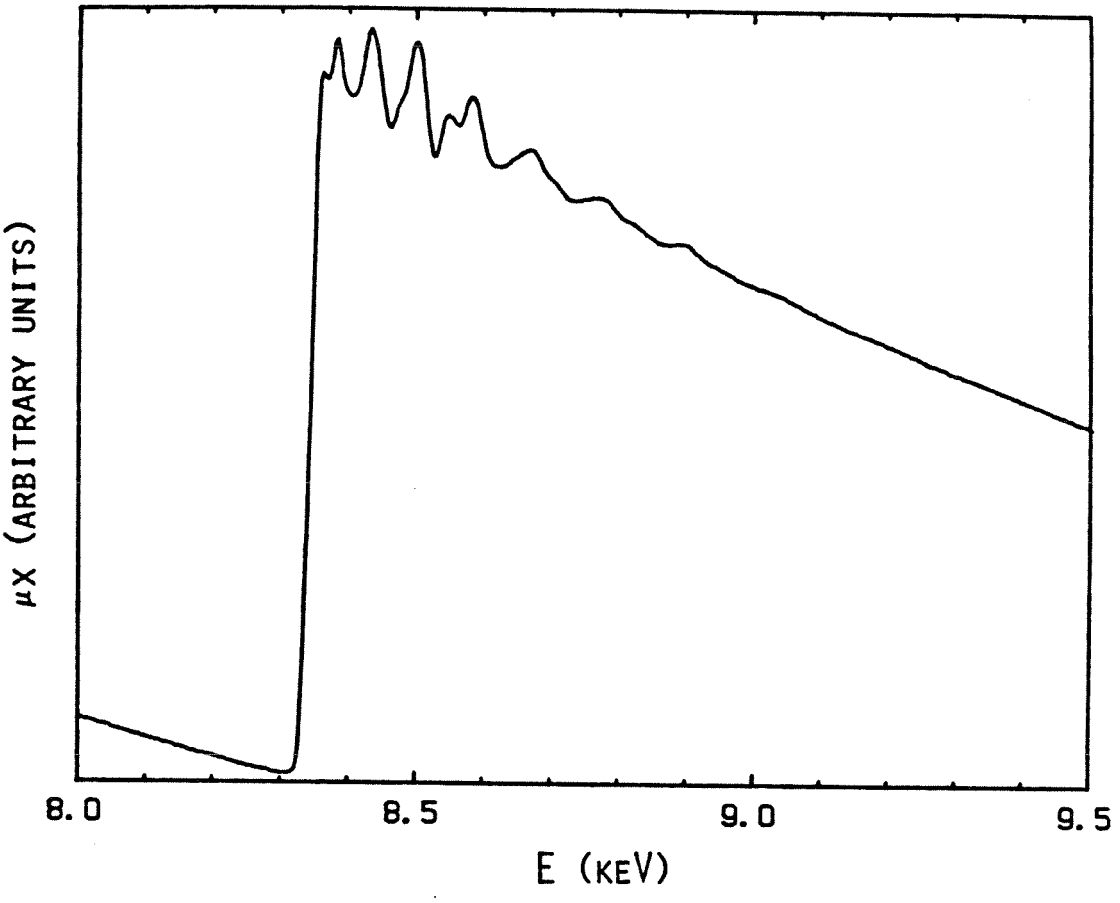

Figure 2.1 Measured absorptance (μx) of a metallic Ni foil at room temperature.

events, and these events are approximately eliminated in the analysis by extrapolating this trend into the post-edge region. This is done using a modified Victoreen functional form [2.16]:

$$\mu = A + B E^{-3} + C E^{-4} \qquad (2.8)$$

The original form proposed by Victoreen did not include the constant term; however it was found necessary to incorporate such a term in order to compensate for the arbitrary overall gain of the detection system (see section 3.2). Using a form such as that shown above ignores the energy dependence of the detection gain, and therefore the extrapolation has systematic errors built into it. However the error involved is a smooth function of photon energy and therefore will be compensated for at a later stage of the analysis (see below).

With the resonant absorption isolated as described above, the non-oscillatory "free atom" absorption must be removed from the measured data, as indicated in equation (2.5). For a variety of reasons (ranging from modification of the initial state due to neighbouring atoms to the above mentioned systematic errors in removing the non-resonant absorption events), it is impractical to use a separate measurement, or tabulation, of the absorption of a monatomic gas to define the free atom contribution to the absorption. Consequently this contribution is derived from the measurement made on the condensed phase sample by fitting to the measured coefficient with a curve which has insufficient degrees of freedom to follow the fine structure. In this work this is accomplished by using a least squares cubic spline of 3 to 5 knots[2.17], starting from just above the edge

and running up to the high E end of the data set. Typically the knots are taken to be uniformly spaced on this interval although it was found that the results obtained did not depend significantly on the precise positions chosen for the knots. Other methods of fitting have been proposed but that described above seems to offer a very satisfactory compromise between performance and ease of implementation for most applications. For systems where the neighbouring atoms are of small atomic number Boland et al.[2.18] have presented an alternative procedure which seems to perform well in spite of the added difficulties encountered in such systems due to the weak scattering and short radial distances involved. The cubic spline fit is somewhat more easily implemented than that of Boland et al. however, and consequently the former procedure has been used in this work.

The μ_o computed as outlined above should not be used for the normalization of the data however. The reason for this is the errors encountered in the somewhat lengthy extrapolation of the Victoreen background into the EXAFS region of the absorption coefficient. Such errors can lead to significant error in the fall off of the resonant absorption with energy and subsequently artificially enhance or suppress the high k region of the EXAFS. For this reason the parametrized free atom cross-sections given by McMaster et al. [2.19] are used in normalizing the difference between the measured coefficient and the cubic spline fit. Thus the actual computation of the EXAFS function, χ , is performed according to the relation:

$$\chi = \frac{\mu - \mu_o}{\mu_M} \qquad (2.9)$$

where μ_o is computed from the spline fit and μ_M is taken from the McMaster compilation, appropriately scaled to match the measured edge discontinuity.

The above then defines the experimentally determined function which is to be analyzed on the basis of equation (2.7). Here too a number of different procedures have been used for extracting physical information from the data, using this equation as a basis. The earliest procedure is that initially proposed by Sayers, Stern and Lytle, which is simply to look at the position of the peaks in the magnitude of the Fourier transform of the data and taking this as the position of the given shell, shifted by an a known amount due to the presence of the term $\alpha(k)$ in the argument of the sinusoid in (2.7). Although this method may still be found in the current literature [2.20], it is not satisfactory since it provides no information about the number of atoms in the shell and it does not account for a number of possible systematic errors which will be discussed below. A more satisfactory, and far more widely used, method is to assume a specific functional form for the density function which is described in terms of a small number of variable parameters. For the vast majority of EXAFS work the form chosen is a Gaussian peak shape at the position of each of the various shells. If such a form is substituted into equation (2.7) the result may be written as:

$$\chi(k) = -\sum_j \frac{N_j 4\pi S'}{k R_j^2} |f_j(k,\pi)| e^{-2\sigma_j^2 k^2} \sin(2kR_j + \alpha_j(k)) \qquad (2.10)$$

In this equation the sum is over shells of N_j identical atoms at a

distance given by R_j. The data are then Fourier analyzed to isolate the contribution of a specific shell of neighbours, and then the parameters appropriate for that shell are determined from a least squares fit. As pointed out by Lee et al. (2.21) the Fourier analysis may be used to isolate the phase and amplitude of individual terms in the sum of (2.10), in which case the parameters may be determined by a number of linear least squares fits. This practice can run into difficulties in some circumstances however, and therefore the more general procedure of using nonlinear least squares to fit the contribution of a given shell directly to the above form may have to be employed.

Naturally, if accurate values are to be obtained for the parameters defining the density function, then some knowledge of the scattering functions must be available. This may be done using either previous experiments on known samples, or by computing the scattering function explicitly in some approximation which will hopefully be valid for the material being investigated. More will be said of this point in chapter 4. The various stages of the analysis described in this section are outlined graphically on the following pages.

In these figures it should be noted that the data are weighted by k^3 prior to the computation of the Fourier transform. This is designed to compensate for the k^{-1} in equation (2.10), as well as the fall off due to $|f(k,\pi)|$ and the damping due to disorder. Operationally the effect is simply to increase the resolution of the transform, thereby limiting the effects of a shell on those around it. If the effects of a single shell are to be truly isolated in applying a window to the transform then it is essential that some type of weighting scheme be applied to enhance the high k region of the spectrum.

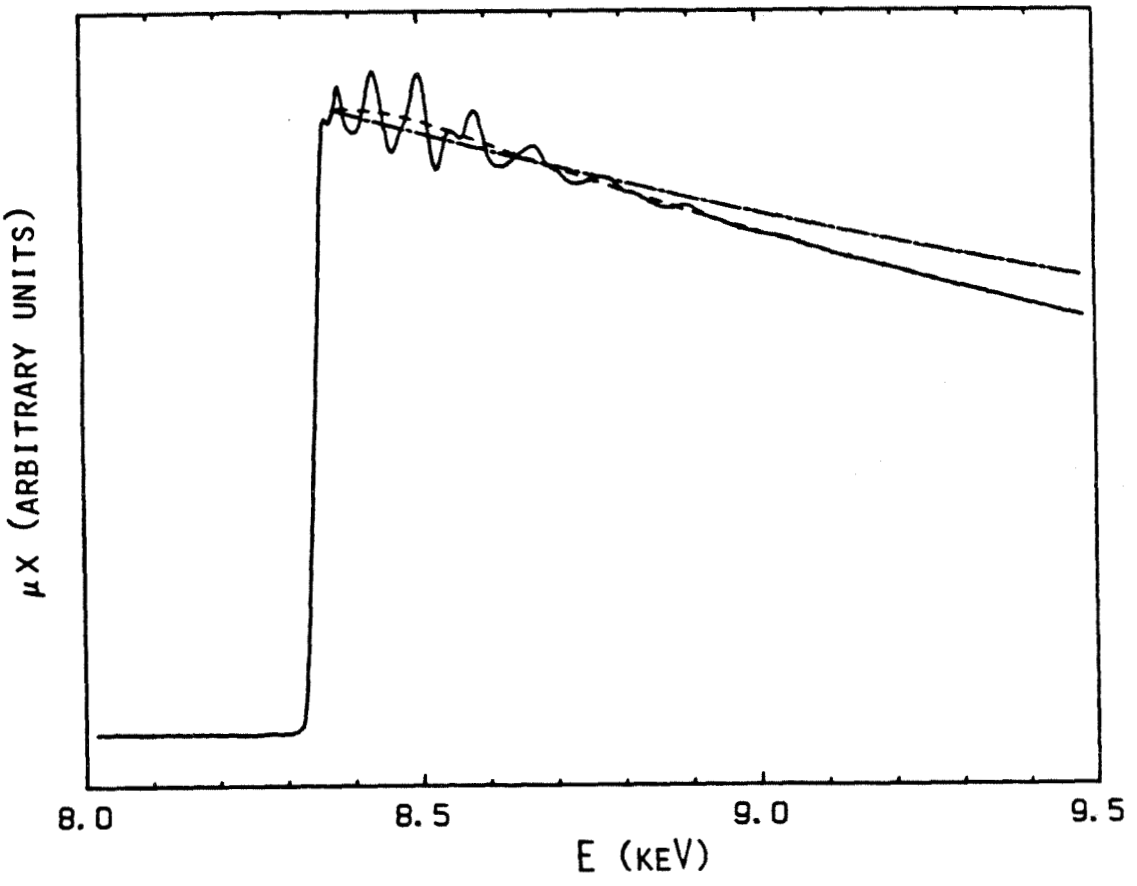

Figure 2.2 Resonant contribution to the absorptance at the K-edge of metallic Ni. Dashed line (---) is the μ_o defined by the spline fit. Dot dashed line (-·-·-·-) is the scaled McMaster absorption coefficient.

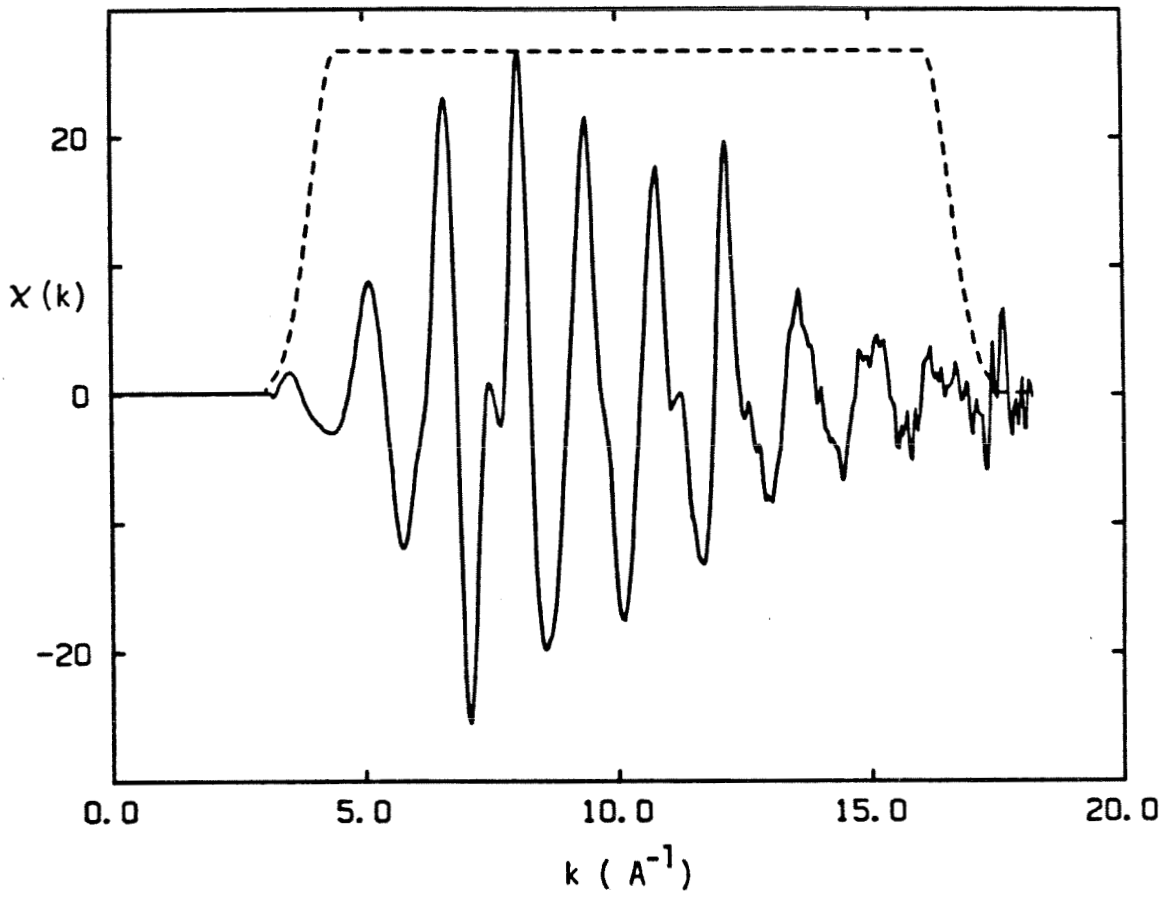

Figure 2.3 EXAFS spectrum $\chi(k)$ for metallic Ni. Dashed line shows the window applied to the data before the Fourier transform is computed.

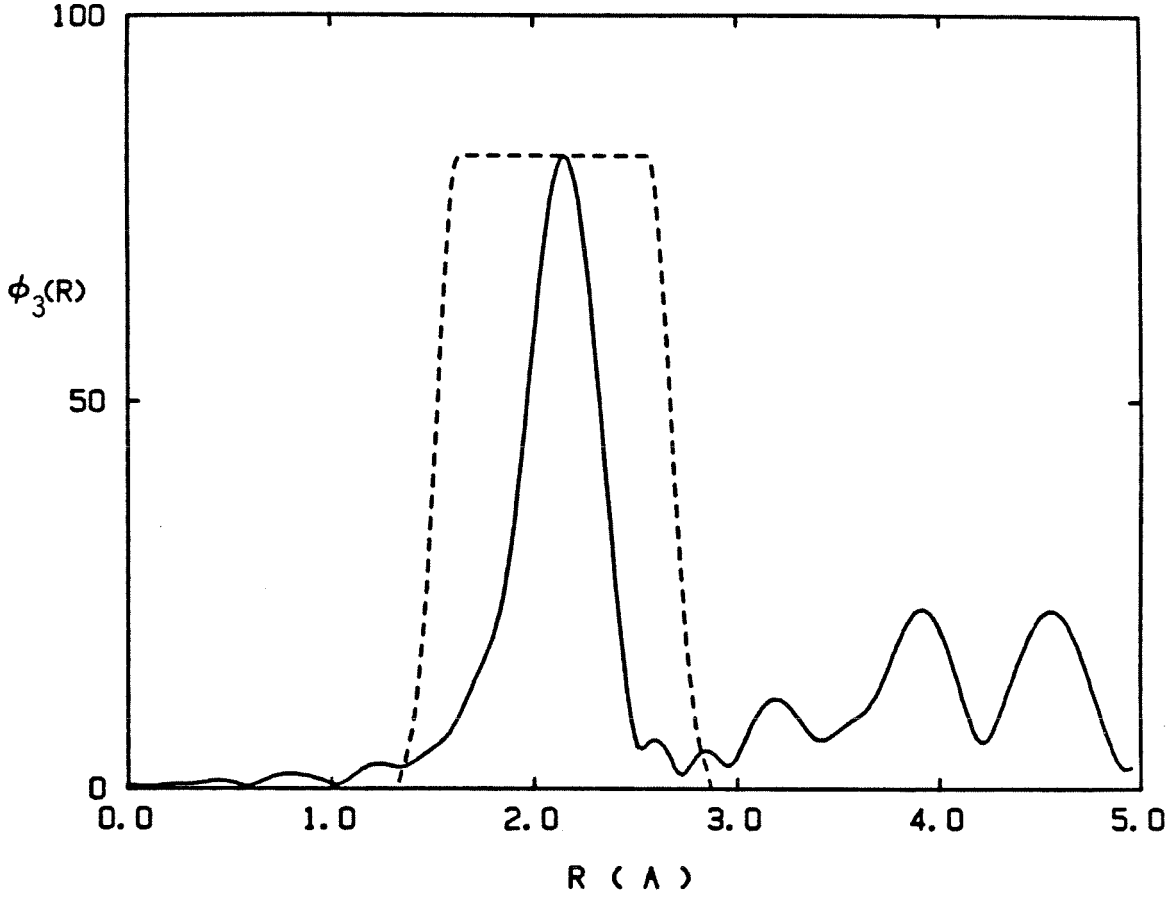

Figure 2.4 Magnitude of the Fourier transform of metallic Ni EXAFS. k^3 weighting was applied to the data before the transform was computed. Dashed line shows the window used to isolate the contribution of the first shell.

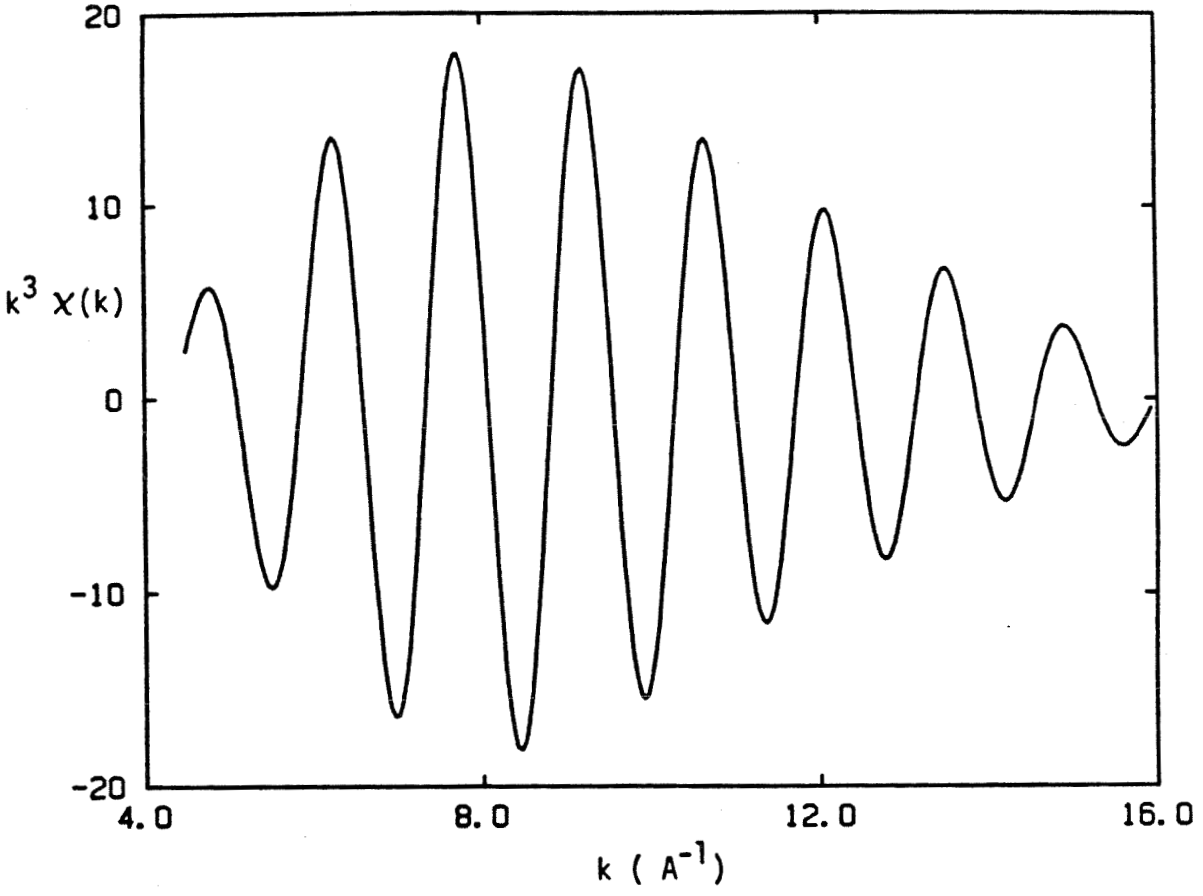

Figure 2.5 EXAFS due to the first shell of neighbours for metallic Ni.

It should also be noted that the window applied to the data before the computation of the transform is not simply a rectangle, but rather it is tapered at both its high and low k ends. This taper is used to suppress the side lobe structure found on either side of the main peaks in the Fourier spectrum. For a more complete discussion of the finer points of computing such transforms the interested reader is referred to the power spectrum estimation section of any book on digital signal processing (such as ref (2.22), for example). The magnitude of the discrete Fourier transform of a "time series", such as a weighted EXAFS spectrum, is called the periodogram of the time series. Since this is a quantity which is used a great deal in EXAFS analysis, a conventional notation has been developed for this function. Therefore, throughout the remainder on this thesis the notation $\phi_n(R)$ will be used to denote the periodogram (i.e. estimated power spectrum) of an EXAFS spectrum which has been pre-weighted by a factor k^n.

2.4 ASYMMETRY

There have been a number of studies where analysis of EXAFS data based on equation (2.10) has produced unphysical values for the parameters. Most notably Eisenberger and Brown's experiments on Zn for various temperatures, in which this type of analysis indicated a decrease in both the number of nearest neighbours and in the radial distance to these neighbours as the temperature was increased[2.23]. This is in disagreement with the known behaviour of the density and the thermal expansion coefficient with temperature. An explanation for this anomalous behaviour was found in the asymmetric nature of the

distribution caused by anharmonicity in the pair potential of the solid. If the Fourier transform of a distribution such as that shown in figure 2.6 is considered then it becomes clear that the long tail is produced by comparatively low frequency Fourier components. Therefore, since the distribution function and measured EXAFS spectrum are approximately Fourier conjugate functions, such a tail should influence the EXAFS primarily at low values of k. However, as has already been discussed, the experimentally determined spectrum does not follow equation (2.10) at low values of k. Hence the information contained in the tail will be severely degraded in the experimental spectrum. The actual effect that asymmetry can have on the spectrum can best be appreciated by considering another way of rewriting equation (2.7), as first suggested by Eisenberger and Brown.

$$\chi(k) = C(k) \sqrt{A^2(k) + S^2(k)} \sin\left(2k\bar{R} + \alpha(k) + \Sigma(k)\right) \tag{2.11}$$

where:
$$A(k) = \int_{-\infty}^{\infty} f(\bar{R} + x) \sin(2kx)\, dx$$

$$S(k) = \int_{-\infty}^{\infty} f(\bar{R} + x) \cos(2kx)\, dx$$

and
$$\Sigma(k) = \tan^{-1}\left[\frac{A(k)}{S(k)}\right]$$

Therefore the effect of modeling the EXAFS spectrum obtained from an asymmetric distribution with a Gaussian, is equivalent to fitting to the above expression under the assumption that A(k), and therefore $\Sigma(k)$, is zero. This can obviously lead to serious problems. To avoid these problems it is easiest to assume some form for the peak shape other than a Gaussian, one which exhibits some asymmetry. This has been done in a number of ways, but the one which will be considered

here is described by the equation below.

$$(2.12) \qquad \rho(R) = A\,(R - R_o)^n\, e^{-(R - R_o)/\sigma}$$

This form has been used in the literature for the cases n=0 and n=2. The first of these gives a very unphysical peak shape and therefore shall not be used in this work. The second alternative (n=2), on the other hand, has been shown to provide a shape which is a reasonable approximation to that seen in the first peak of the radial density function of a liquid [2.24], and therefore will be used.

Using equation (2.12) with n=2 implies the following relations for $(S^2(k)+A^2(k))^{1/2}$ and $\Sigma(k)$:

$$(2.13) \qquad S^2 + A^2 = \frac{2A\sigma^3}{(1 + (2k\sigma)^2)^{3/2}}$$

$$\Sigma(k) = 3\,\tan^{-1}(2k\sigma)$$

Naturally any fit based on equation (2.11) using the relations (2.13) must still be made only on an interval starting at about $4\ A^{-1}$. However fits based on these relations have been successfully applied to EXAFS studies of disordered systems[2.25], and will be used in this work.

2.5 THE THRESHOLD ENERGY

One point which has been side-stepped up to this point in the discussion is the fact that all of the relations derived from the

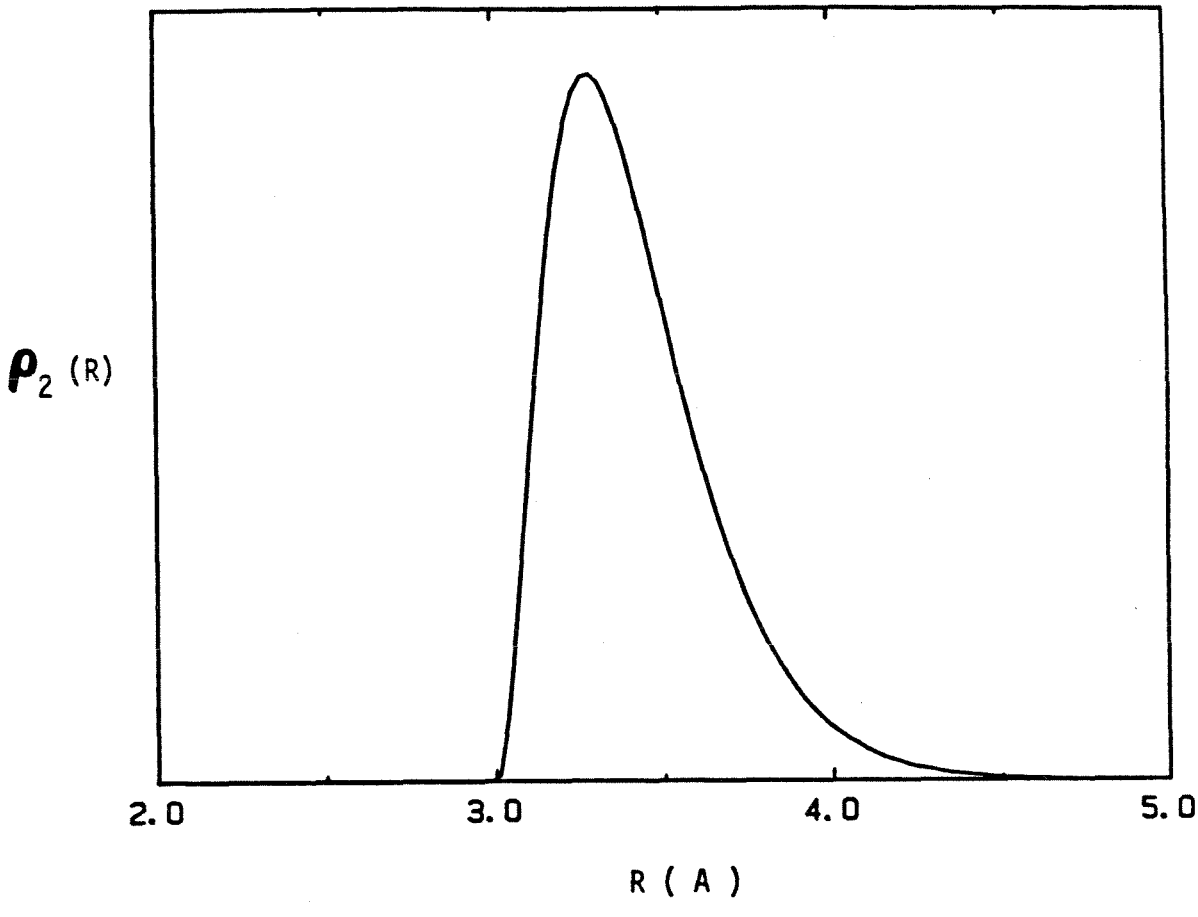

Figure 2.6 Asymmetric peak shape given by equation (2.12) for n=2.

theory for explaining the fine structure are based on the photoelectron wave vector, k, which is not directly measurable from the experiment. On the other hand, the experiment naturally provides the energy of the incident photon which is related to k through the following relation.

$$k = \sqrt{2m(E - E_o)/\hbar^2} \tag{2.14}$$

However the value of E_o is also not a quantity which can be unambiguously determined from experiment. Nevertheless, once a spectrum has been collected in terms of photon energy, a wave vector axis must be constructed on the basis of the above equation for some value of E_o if use is to be made of the equations discussed in section 2.2. Since E_o is not known precisely, the effect of using the equations of section 2.2 with a k axis which is in error must be considered. First it will be noted that if E_o is in error, then the k axis will be affected primarily at low k where the theory is not applicable in any case. However, even if the functional form of the argument of the sinusoid is not changed explicitly at all for large k, a change in that argument at low k will result in a constant phase offset at large k. In a fitting procedure which does not explicitly take such an offset into account, the value obtained for R will have to deviate somewhat from its true value in order to compensate for the offset. In other words an incorrect value for E_o will introduce yet another contribution to the nonlinear part of the sinusoid phase, a contribution which will remain even if the effects of $\alpha(k)$ and $\Sigma(k)$ have been properly accounted for. Hence it is clear that some method of selecting E_o in

a reasonably accurate manner must be an integral part of any attempt to obtain accurate physical parameters from EXAFS measurements.

In an ideal case where a core state is excited in a true single particle transition, and no unoccupied bound states exist between the initial core level and the continuum, E_o will simply be the binding energy of the initial core state. Furthermore in this idealized case the edge transition will have the shape of an arc-tangent function whose inflection point appears at precisely the energy E_o [2.26]. In real experiments, however, unoccupied Rydberg-type states and many body effects will invariably distort the simple arc-tangent shape of the edge, and consequently the inflection point of the measured edge will rarely, if ever, coincide with the single particle continuum threshold energy E_o (see figure 2.7). Nevertheless Boland, Halaka and Baldeschwieler have suggested that the position of the edge may be obtained by convolving it with a Gaussian "resolution function" of sufficient breadth to smear out all of the sharper features related to many body and bound state transitions.[2.18] The key to this method is that the inflection point of the curve resulting from the convolution of an arc-tangent with a Gaussian is at the same position as the inflection point of the original curve itself. Consequently, if a series of Gaussians of progressively increasing width are considered, then the inflection point of the convolved curve should appear at a constant position once the width is sufficient to wipe out all features in the original curve except the underlying arc-tangent. This method has apparently been used with success for spectra collected at the edges of a number of the 3d transition metal elements. However during the course of the present work it was found to be

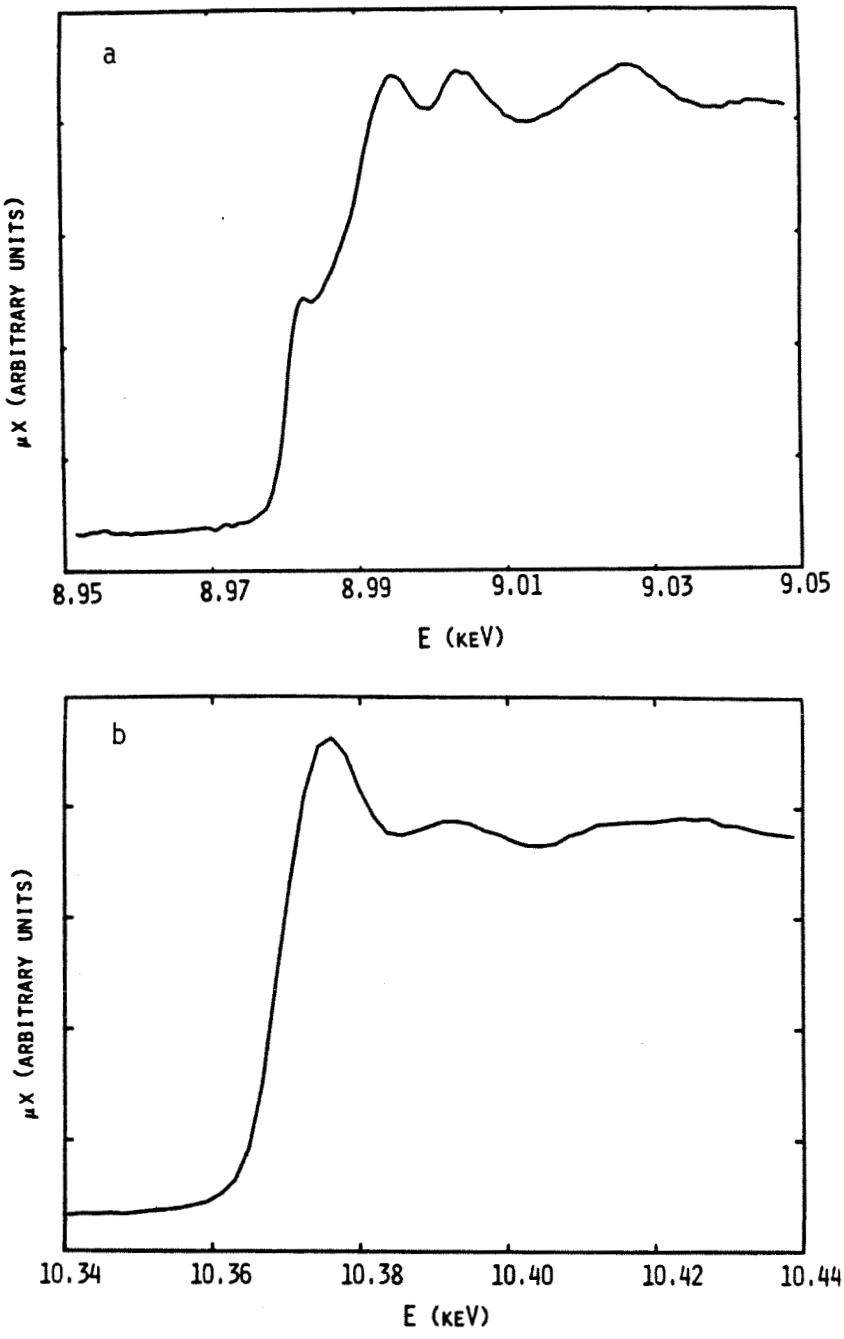

Figure 2.7 Complicated nature of the edge discontinuity for real materials. a). Metallic Cu, showing band structure effects. b). Crystalline Ga_2La showing a "white line" excitation to a Rydberg-like 4P state on the Ga.

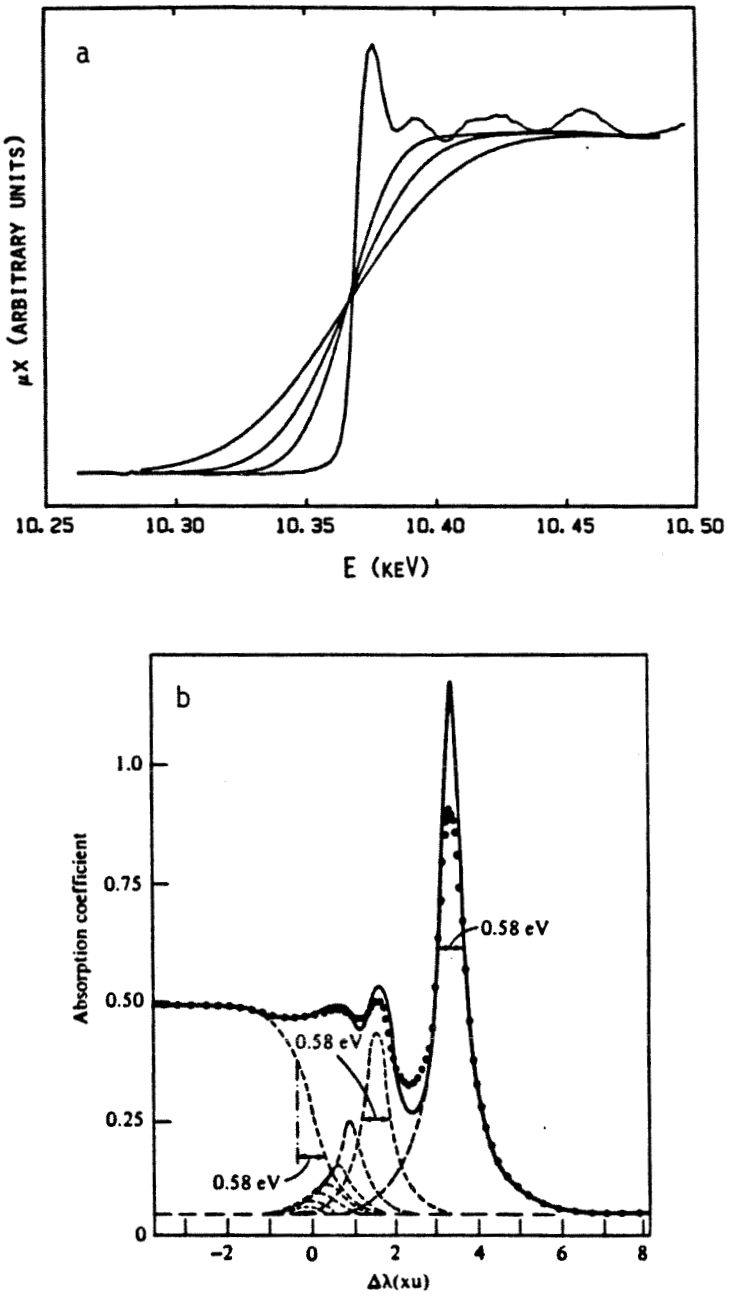

Figure 2.8 a). Absorption edge of Ga_2La and the same edge convolved with Gaussians of 36, 54 and 80 eV width. b). Absorption edge for Ar, and its interpretation in terms of a continuum excitation plus several Rydberg-like bound excited states. (taken from reference (2.24)).

unsatisfactory when applied to the Ga edge which exhibits a strong "white line" (due to excitation to a bound 4-p state). Figure 2.8b displays the results of convolving the Ga edge measured for Ga_2La with Gaussians of various widths. From this figure it would be tempting to take 10.366 keV as the "isosbestic" (sic) point to which Boland et al. refer. However, by considering the analogous edge shown in figure 2.8a, it becomes clear that E_o should be at an energy which is higher than the position of the inflection point in the original spectrum, whereas the point suggested by figure 2.8b is actually lower in energy than the inflection point of the original edge! A solution to this problem would be to go to still wider Gaussians, however soon the convolved curves would be making very shallow angles with the energy axis and therefore the accurate determination of their point of intersection would be most difficult. Consequently it is the opinion of this author that, while this method of selecting E_o may be appropriate for many edges it is impractical to apply it to edges which show strong white lines.

Most alternative methods of selecting E_o, with one exception, rely on the assumption that $\Sigma(k)$ (from equation (2.11)) is zero, and that $\alpha(k)$ is well known, either from theory or from experiments on known standard samples. Under these circumstances, any nonlinearity which remains in the difference between the measured phase function and the known phase shift $\alpha(k)$, must be due to an incorrect selection of E_o. Therefore the value of E_o is changed to make this difference a linear function and the value which accomplishes this is taken as the correct one. These methods must obviously fail in the case where the distribution function is asymmetric (unless the problem has already

been solved and the function $\Sigma(k)$ is known!).

The final method which has been proposed in the literature is to simply treat E_o as another free parameter in the fitting procedure (2.21). It is argued that an artificially good fit should not be obtained for an incorrect value of R when this procedure is used, because E_o changes the phase primarily for low k, whereas a change in R influences the phase more as k increases. This method of selecting E_o is not as susceptible to the problems described above as the other methods, however care should be taken to make sure that changes in E_o are not allowed to mask changes in $\Sigma(k)$ caused by differences in the atomic distribution functions of two materials. This point will be discussed at greater length in chapter 4.

3 EXPERIMENTAL PROCEDURES

3.1 SAMPLE PREPARATION

All alloys used in this thesis were produced by levitation melting the appropriate ratio of bulk elemental material on a water cooled silver boat in a purified Ar atmosphere. The starting materials for the $La_{1-x}Ga_x$ alloys were La rod (99.9% metallic purity) and Ga chips (99.999% pure). Typically ingots of 1.5 to 2 grams were produced at a time. Homogeneity of these ingots was ensured by remelting each several times, breaking them open for visual inspection, then remelting them once more. Weight loss during alloying were generally less than 0.05%, and in all cases the compositions quoted are the nominal ones.

Due to its highly reactive nature the La was given special treatment. After a piece of appropriate size was cut from the parent rod, a steel brush was used to remove most of the surface oxide. The La was then melted on the silver boat and all slag was worked to one end of the ingot. The slag was then removed and depressions drilled in the ingot in order to form a boat of La. This La boat was then Ti getter cleaned for several days by sealing it in an evacuated fused silica tube along with some Ti strips which were heated to approximately 850 C, while the La was kept at about 200 C. The end result of this process was a La boat with a visibly shiny metallic surface. During alloying the Ga had to be placed on top of this La boat and care taken to ensure that the pure Ga did not come into contact with the silver levitation boat, since such an event would have resulted in the formation of a Ga-Ag alloy and a ruined silver boat.

All amorphous samples used were prepared by rapidly quenching small droplets of molten alloy with a piston and anvil apparatus[3.1]. The resulting samples were in the form of foils, typically 1 to 2 cm. in diameter and 30 to 40 μm thick. After quenching, the samples were checked for signs of crystallinity with a Norelco vertical diffractometer scanning at a rate of 1 deg per minute and using Cu K radiation. Any samples showing a trace of crystalline inclusions at this stage were discarded. All samples used in subsequent absorption experiments were further examined, after the completion of the absorption experiment, by step scan X-ray diffraction measurements with a minimum of 4000 to 5000 photons collected per channel. The results reported in chapter 4 of this work were based on samples which showed no distinct crystalline peaks in this more detailed X-ray scan as well. Some samples, however, did exhibit diffraction peaks, corresponding to Ga_3La_5 crystalline inclusions, in the more detailed X-ray scan, even though none were detected in the previous "rough scan." The absorption spectra for a few of these latter samples were also analyzed in the normal way to see if this amount of a crystalline phase would change the results obtained. It was found that the physical parameters obtained did not change measurably for samples where X-ray diffraction showed a clear indication of about 5 to 10% crystals in the amorphous matrix. This lends support to the conclusions that the physical parameters quoted in chapter 4 are those of the amorphous material and are not influenced by any possible microcrystalline inclusions present below the detectable level of the X-ray diffraction test.

The as-quenched foils were too thick to be appropriate for

absorption experiments and therefore had to be thinned. This was accomplished by mechanical polishing with diamond pastes of 1/4 to 6 μm grit size[3.2]. The samples were typically thinned to 15 to 20 μm, or about 1.5 absorption depths, representing a compromise between the conflicting desires of optimizing the signal to noise ratio[3.3] and reducing the "thickness" effect[3.4]. After polishing the samples became extremely reactive, and would visibly tarnish in a matter of minutes if left in air. For this reason they were immediately placed in a sample chamber which was subsequently purged with He and then evacuated for the duration of the experiment. As a result of this precaution the surface of the sample suffered no further degradation during the course of the experiment.

Each sample was used in a total of 12 individual measurements of the absorption coefficient in the region around the Ga K edge, each individual scan lasting about 5 hours. These 12 scans were then combined together in order to provide a form of signal averaging, as well as to directly provide an estimate of the statistical errors associated with the measurement.

The crystalline Ga_2La samples were prepared by powdering a portion of an ingot, produced as described above, with a tungsten carbide mortar and pestle. Ga_2La is extremely brittle, making the production of a very fine powder quite straightforward. The powder produced was easily passed through a 400 mesh screen, indicating that the vast majority of the powder particles were significantly smaller than the 38 μm maximum dimension passed by the screen. An optical microscope was used to confirm the fact that most of the particles were closer to 15 or 20 μm than 38 μm in diameter. In order to facilitate the

production of uniform powder samples of various thicknesses, various quantities of Ga_2La powder were mixed with 30 to 50 mg of MgO which acted as a filler. The resulting mixture was then pressed in a 1/2 inch die to a pressure of about 23,000 psi, thus producing a solid, though fragile, disk of a thickness appropriate for X-ray absorption measurements. These disks were then sandwiched between two pieces of Scotch tape in order to provide a degree of mechanical integrity to the specimen. X-ray diffraction measurements on the final powder compact confirmed that neither the powdering nor the pressing induced any measurable change in the structure or the lattice constants of the material away from the published values.

3.2 DESCRIPTION OF THE EQUIPMENT

All absorption spectra were collected using a prototype "in-lab" X-ray spectrometer designed by Art Williams[3.5]. This spectrometer is displayed schematically in figure 3.1 which is taken directly from reference 3.5. The key feature of this spectrometer, although it is by no means unique to this design, is the use of a Johansson geometry focussing crystal monochromator. The use of this crystal may best be described with reference to the diagram in figure 3.2, where the optics are described in two dimensions.

The crystal is ground and bent in such a way that its surface defines a circle of radius R, while its crystal planes lie on circles of radius 2R (neglecting for the moment any variation from one plane to the next). The circle of radius R is called the Rowland circle (in analogy with the terminology used in the applications of curved diffraction gratings) and both the source (S) and the detector slit (D)

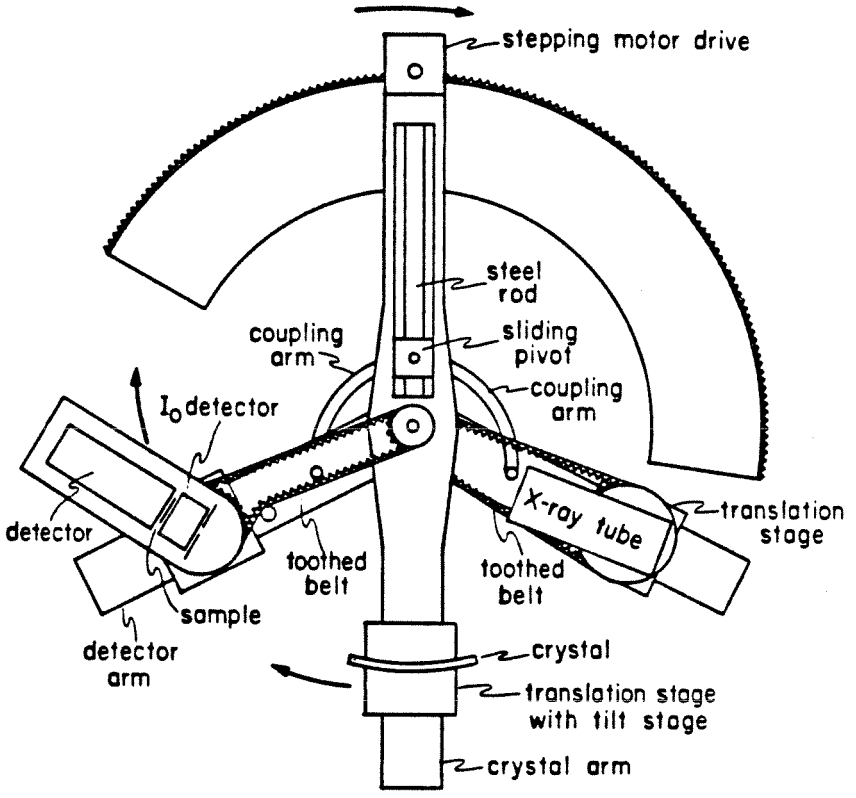

Figure 3.1 Schematic diagram of the Johansson geometry X-ray spectrometer used. (Taken from reference (3.5)).

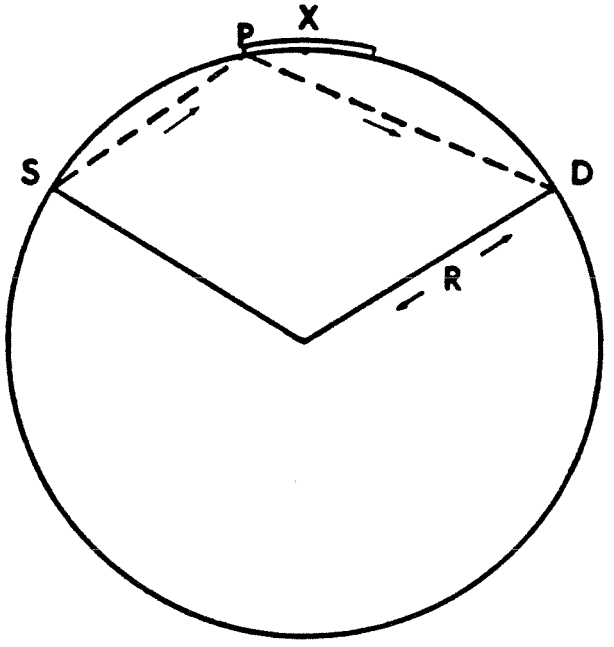

Figure 3.2 Ray diagram for a Johansson geometry focussing monochromator.

must lie on this same circle. It is a simple geometrical exercise to show that any angle $\widehat{SPD}$ inscribed in the Rowland circle will be the same, irrespective of the position of the point P. Hence all rays originating from S and scattering from the crystal surface to the point D will be scattered through the same angle. If the planes in the crystal can be configured in such a way as to ensure that these same rays make an angle with the crystal planes which does not depend on the position of incidence along the crystal, then it is clear that all rays of a given energy (specified by the angle of incidence with respect to the crystal planes) emitted from S and hitting the crystal, will be focussed onto the point D (assuming that the arcs SX and XD are held equal so that the Bragg angle is simply 1/2 of the scattering angle). It is not difficult to show that this latter condition is satisfied by having the crystal planes lie on circles of radius 2R, and that in this configuration the relevant Bragg angle for reflection is given by 1/4 of the angle $\widehat{SXD}$.

The great advantage of this type of monochromator, over a simple flat crystal monochromator, is that it allows a very large solid angle to be accepted from the source with only a marginal sacrifice in resolution. Thus this device has been used to deliver on the order of 3×10^6 photons per second into a 10 eV window at about 9 keV, using a fixed anode Mo X-ray tube operating at 20 kV and 24 mA. Although the fluxes and resolution of current synchrotron sources are significantly superior to that obtained here, the fact that this spectrometer can be used as a dedicated facility means that such spectrometers may have a definite place in research labs where X-ray absorption may be desired as a standard tool.

Referring once again to figure 3.1 it is seen that the energy focussed by the crystal may easily be changed using a single stepping motor motion to change the angle $\widehat{SX}$. The mechanical linkage shown ensures that the two angles $\widehat{SX}$ and $\widehat{XD}$ are kept equal, allowing the focussing condition to be maintained over a large angular range (Bragg angles between 9 and 61 degrees can be easily accommodated).

The spectrometer used has a Rowland circle radius of 40 cm and an angular resolution of approximately 2.7 μrad (or .6 arc sec) in the drive. Play in the mechanical linkage as well as in the drive itself, results in a backlash of approximately 6.8 mrad. However, for a given experiment, position reproducibility is better than 20 μrad. Near the Ga K edge, where the majority of the measurements reported in this work were taken, this corresponds to an energy setting reproducibility of better than 1 eV from one run to the next. This level of reproducibility is important if the practice of adding the results of several runs together is to be used for signal averaging.

The spectrometer was calibrated by measuring the intensity of the radiation provided by the X-ray tube as a function of energy over an energy interval of one or two keV. Invariably a number of characteristic lines from the numerous impurities in the anode of the tube would be seen in such a scan. A subset of these lines (typically the 4 to 7 most intense lines) would be identified and their known angular positions computed from tabulated values for their energies [3.6]. Since the drive is linear in the Bragg angle a linear least squares fit was then made to the above set of angles and an energy scale corresponding to this angular scale was computed. This done, the deviations of the drive from perfect linearity were investigated by

recording the position of all lines in the scan with respect to the newly constructed energy axis. In no case was the energy of a line computed from this procedure found to differ by more than 2 eV from the published energy for that line. In fact most deviations were less than 1 eV except for lines which were very faint. A sample calibration scan used for measurements of Ga edges is shown in figure 3.3.

The spectrometer alignment is a comparatively straightforward, though rather time consuming procedure. First an alignment jig is used to set the detection stage at a distance of 40.0 cm, and the crystal and anode postions at a distance of about 40 cm., from the central axis of the machine. The in-plane tilt angle of the crystal is then adjusted for maximum intensity at the detector, for a given energy setting, say E_1. A different energy, E_2 , is then selected (typically one which differs by about 150,000 motor steps from E_1) and the position of the source (along its arm from the spectrometer axis) is varied until the maximum intensity is seen at the detector. If a change in the source position of δS is required then a new source position is selected as $-0.3\ \delta S$ from the setting used at energy E_1. The spectrometer is then reset to energy E_1 and the process is repeated. Typically this procedure will converge after only a few iterations, and the result is that the source and detector slit will now be at the same distance from the spectrometer axis. Obviously the distance between E_1 and E_2 should be increased as the alignment improves since this will increase the sensitivity of the procedure. Equally obviously, both energies should be chosen to lie in a flat part of the source spectrum (i.e. well away from any characteristic lines).

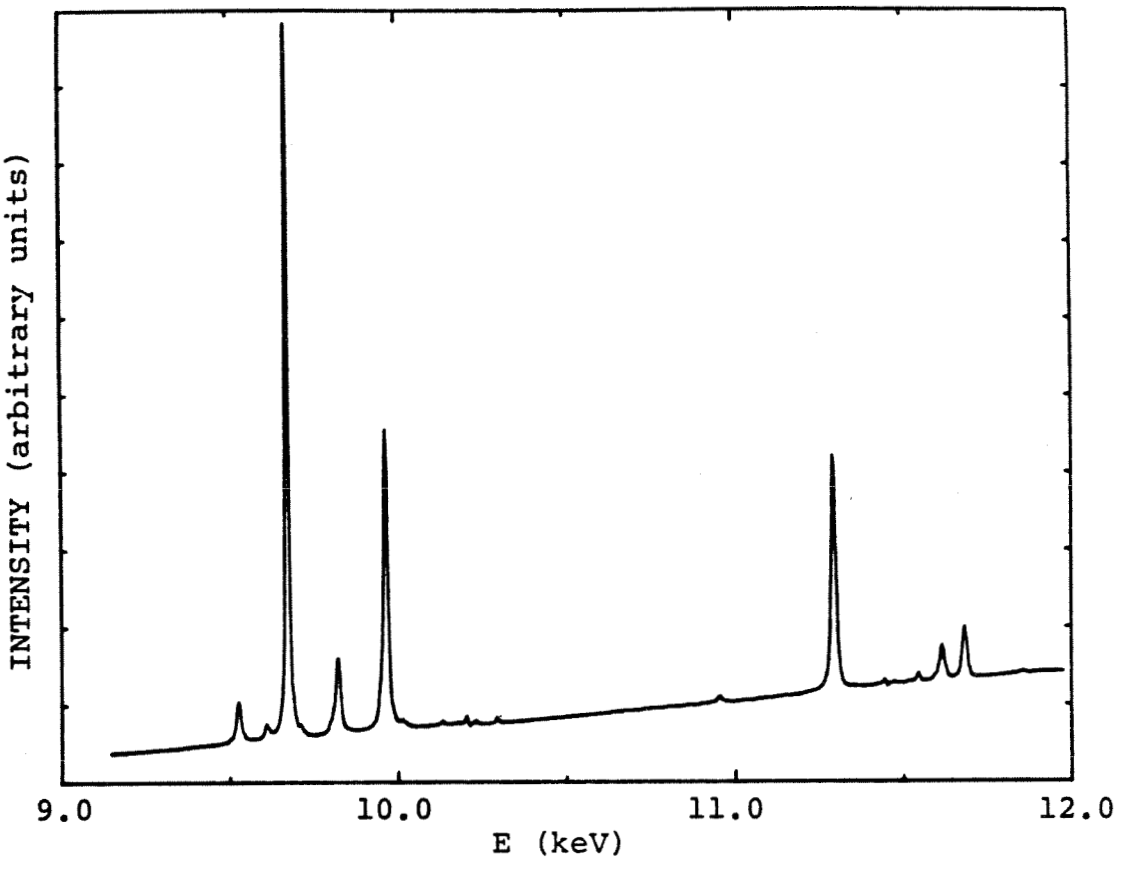

Figure 3.3 Energy dependence of photon flux from the Mo X-ray tube used for measurements of Ga EXAFS. The two groups of lines are W L_β and W L_γ, and the Ga edge occurs at an energy of about 10.37 keV.

After the source and detector positions have been determined as outlined above, the position of the crystal should be varied to optimize the intensity or resolution, depending on the requirements of the particular experiment. The final stage of the alignment requires moving the source, crystal, and detector stages in or out uniformly in case the crystal used has a radius which differs slightly from the specified 40.00 cm. This last stage of alignment is the most time consuming and has generally been found to produce only slight differences in the spectrometer performance.

The source used in this work was a standard 1.8 kW Mo anode sealed X-ray tube with a long fine focus beam geometry (focal spot 0.4x12 mm). The average take-off angle was roughly 6° which gives a projected source width of only 0.04mm. The detector slits were typically 0.075 to 0.15 mm wide, and using this information a rough estimate of the energy resolution of the spectrometer may be computed from the following relation, which was given by Knapp [3.7] for a similar spectrometer.

$$(3.1) \qquad \Delta E = \frac{E^3 D^2}{2RH^2C^2}\left[(W_s + W_d)^2 + \left(\frac{hc\ell n2}{\mu dE}\right)^2 A + \frac{1}{A}\left(\frac{h^2}{8R}\right)^2 \right]^{\frac{1}{2}}$$

$$\text{where} \qquad A = \cos^2\theta_B = \frac{4d^2E^2 - h^2C^2}{4d^2E^2} \approx 1.0$$

Here W_s and W_d are the widths of the source and the detector slits respectively. H is the height of the source and the detector slits which is taken to be the same in both cases, R is the Rowland circle radius, θ_B is the Bragg angle, and μ is the absorption coefficient of the crystal. Figure 3.4 displays the results of this calculation,

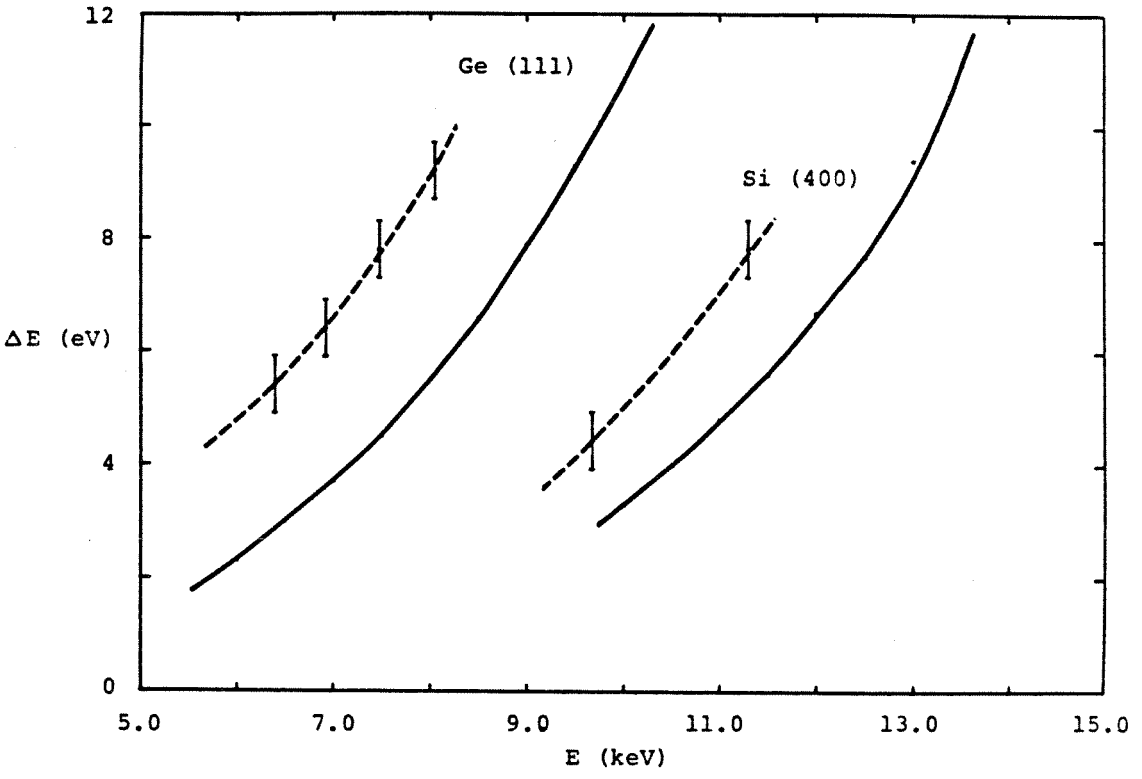

Figure 3.4 Energy resolution of the spectrometer. Solid curves give the result of calculations based on equation (3.1) for Ge(111) with a .003" detector slit and for Si(400) with a .006" detector slit. Dashed curves are provided to aid the eye in following the trend defined by the experimental points.

along with the actual resolution obtained, for the various crystals used. As should be expected the resolution obtained is significantly worse than that predicted on the basis of equation 3.1, since this equation is based on an ideal geometry which ignores all crystal imperfections and errors in the alignment of the spectrometer.

The resolution of the spectrometer was measured by carefully recording the profiles of the characteristic lines from the impurities in the anode. Assuming that these profiles are due to a Lorentzian line of known width, convolved with a Gaussian resolution function of unknown width, the resolution was determined by varying the width of the Gaussian until a best fit was obtained[3.8].

The crystals used in this thesis are listed below in table 3.1, along with their useful energy ranges, when used in first order. This useful range is determined by such considerations as available flux, and resolution, the minimum anode potential available for the source (15 kV), and the physical constraints of the spectrometer's angular range.

TABLE 3.1

Useful energy range for the crystals used in this work

CRYSTAL	E_{min}	E_{max}
Ge(111)	6.0 keV	10.5 keV
Si(400)	10.0 keV	14 keV (?)

It is seen that the Ge(111) crystal is appropriate for measurements on

3d transition element compounds, and indeed this crystal has been used for measurements of the edges of Fe, Ni and Cu. For this crystal the lower energy limit is set both by a decreasing intensity and the 15 kV minimum potential setting of the source. Although an ideal crystal of this orientation has an extinct second order reflection, the distortions produced by the curvature of the crystal are sufficient to allow a very weak second order reflection to exist. The intensity of this second order reflection is approximately 0.1% of the primary beam. Nevertheless, this may be sufficient to cause problems in regions near strong characteristic lines in the spectrum of the source. For this reason it may be desirable to run the source at a potential less than 2 times the energy of interest, rather than the 3 times one might expect, if the region being investigated contains some characteristic lines in the source spectrum. The upper limit of the energy range of this crystal is set primarily by the rapidly decreasing energy resolution at energies near 10 keV.

The Si(400) crystal has been used successfully for measurements at the Ga K edge (10.4 keV), but could not be used at energies less than this due to insufficient flux. At higher energies the resolution starts to drop off due to the small absorption coefficient of Si. By carefully limiting the vertical divergence of the beam, it may be possible to extend the range of this crystal up to the edge of Br (13.5 keV), however this has not yet been demonstrated.

The spectrometer is controlled by a prototype "black-box" based on a 6502 microprocessor, and designed by Douglas Whiting. This controller is able to record both incident and transmitted intensities at up to 1024 different energy settings, which may or may not be evenly

spaced in angle. Intensity is recorded as a number which is either equal to, or proportional to, the number of photons detected during the channel dwell time. The recording time taken for each energy setting may be determined by either a predetermined length of time, or by the time it takes to accumulate a predetermined number of counts in the transmitted beam detector. Upon completion of the experiment the recorded data may be transferred to a host computer over a standard RS-232 data link.

The X-rays are detected using either an ionization chamber or a NaI(Tl) scintillation detector, depending on the available flux of photons. If the detector sees at least $5x10^4$ photons per second then an acceptable level of noise is obtained using an ionization chamber. At lower fluxes the noise in the current to frequency converter used in conjunction with the chamber (see fig 3.5) dominates the statistical noise, and therefore discrete photon counting is required. The NaI(Tl) detector is used with an Ortec model 579 "fast filter" nuclear amplifier. With the shaping times of this amplifier set to 100 nsec the measured dead time of the total photon counting circuit is approximately 1.3 μsec. Even at count rates of $5x10^4$ this leads to a dead time correction of only 6% and hence the useable ranges of the two types of detectors compliment each other nicely. Naturally an ionization chamber was always used to monitor the incident beam intensity.

The ionization chambers used were constructed using 6061 aluminum parts to limit the effect of possible fluorescence from the walls and teflon insulation was used throughout to limit leakage currents. Great care was taken during assembly to remove all grease from the

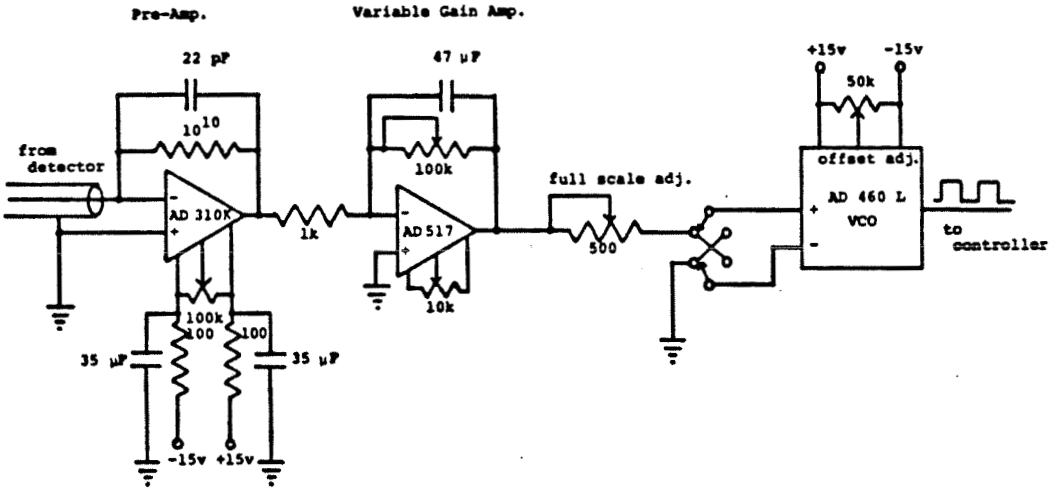

Figure 3.5 Electronics used to convert the pico-amp currents provided by the ionization chambers to the TTL pulse train measured by the controller.

inside of the detectors to keep leakage to a minimum as well. Generally Ar was used as a fill gas as a compromise between detector thickness and cost. The incident beam chamber was charged with sufficient pressure to absorb between 20 and 40% of the beam. Under ideal circumstances the incident chamber should only absorb about 20% of the beam for optimal signal to noise[3.3], however, a slightly thicker detector was sometimes needed in order to maintain a count rate of $5x10^4$. The ionization chambers were biased with at 235V battery and they were connected to the current to frequency converters through special low noise coaxial cables (amphenol 21-537) as recommended by Spokas and Meeker[3.9].

The current to frequency converters used with the ionization chambers are described in figure 3.5. The 10^{10} ohm resistors used in the preamplifiers for the current to frequency converters were obtained form Victoreen Nuclear and the capacitor in parallel with this resistor uses polystyrene as a dielectric in order to provide sufficiently low leakage. The Analog Devices model 310K op amps used in the preamplifier are designed to have extremely high input impedence, low voltage drift and low input bias current. These characteristics are necessary since the currents being measured are typically on the order of pico-amps. After preamplification the signal is fed into a variable gain amplifier and thence into a 0-10V, 1 MHz voltage controlled oscillator (VCO). The output from the VCO is then fed directly into the input of the controller which has TTL counters acting as a high speed front end to the 6502 microprocessor.

When the scintillator detector was used for the transmitted beam a single channel analyzer was required to discriminate against noise

pulses and cosmic rays and to provide TTL compatible pulses, suitable for processing by the microprocessor. In addition with this type of detector, a multi-channel analyzer was used to determine the maximum allowed potential on the source anode. The potential used was chosen so that no indication of a peak corresponding to a harmonic reflection was seen at the minimum energy setting of the spectrometer used in the experiment of interest.

One of the most troublesome problems encountered when measuring EXAFS on in-lab spectrometers is the appearance of characteristic lines in the source spectrum, and the effect these lines have on the measured absorption coefficient. An analogous problem arising from glitches in the monochromator output has also plagued synchrotron users.(3.10) Although the response of the electronics used in the ionization chamber is highly linear with respect to changes in measured intensity, small offsets can lead to significant effects in the region around a strong line in the source spectrum. In addition, it should be noted that the appearance of a line in the source is not simply equivalent to an increase in source intensity! This inequivalence is due to the finite energy resolution of the spectrometer and the fact that, for a given energy setting, different areas of the sample will be sampling slightly different energies. If all portions of the beam were treated identically this would still not present a problem. However, invariably some portions of the beam will have slightly different effective gains in the two detectors. These variations in effective gain could be due to such effects as variations in sample thickness, or fluorescence off of the detector slit, sample holder or back wall of the I_t ionization chamber.

To see the result of the above discussed effect, consider the following simplified model. Assume that the two detectors have nominal gains $G_o(E)$ and $G_t(E)$ respectively, and that for a given spectrometer setting the beam is composed of the centre energy plus a small amount of flux at an energy which differs from this by a small amount (say $E+\delta E$). Furthermore assume that the transmitted beam detector has a slightly different effective gain for the second component of the beam than it has for the primary component (e.g. as would happen if a small part of the upper extremity of the sample was slightly thinner than the rest). In what follows this difference in effective gain is accounted for by a factor α . If M_o and M_t are the measured intensities (expressed as a total number of counts in a given time), then the measured absorption coefficient will be obtained from the ratio:

$$\frac{M_o}{M_t} = \frac{G_o(E)}{G_t(E)} \frac{I_o(E) + \alpha_o I_o(E + \delta E)}{I_t(E) + \alpha_t I_t(E + \delta E)} \tag{3.2}$$

which may be rewritten as :

$$\frac{M_o}{M_t} \approx \frac{G_o(E)}{G_t(E)} \frac{I_o(E)}{I_t(E)} \left(1 + \frac{\alpha_o}{G_o(E)} \frac{I_o(E + \delta E)}{I_o(E)} - \frac{\alpha_t}{G_t(E)} \frac{I_t(E + \delta E)}{I_t(E)} \right) \tag{3.3}$$

If the variation of the absorption coefficient with energy can be neglected, then the above expression reduces to:

$$\frac{M_o}{M_t} \approx \frac{G_o I_o}{G_t I_t} \left(1 + (\beta_o - \beta_t) \frac{I_o(E + \delta E)}{I_o(E)} \right) \tag{3.4}$$

Here the explicit E dependence of the G's and I's has been suppressed, and a new variable $\beta = \alpha / G$ has been introduced for notational convenience. The above finally implies that the measured absorption coefficient will be:

$$(3.5) \qquad \mu_m(E)\, x = \mu(E)\, x + (\beta_o - \beta_t) \left(1 + \frac{dI_o}{dE} \frac{\delta E}{I_o} + \frac{G_o(E)}{G_t(E)} \right)$$

Generally $\frac{G_o(E)}{G_t(E)}$ will be a smooth function of the photon energy and this will not influence the experiment as such variations are removed in the analysis (see section 2.3). However the derivative of I_o can be significant in the region of a characteristic line, and so the relevant equation is:

$$(3.6) \qquad \mu_m(E)\, x = \mu(E)\, x + (\beta_o - \beta_t) \frac{dI_o}{dE} \frac{\delta E}{I_o}$$

It is comparatively simple to limit this second term to order 1% of the first, although reduction below this level can be quite difficult in the vicinity of a characteristic line. However, at a sufficient distance from the edge the variations in the absorption coefficient of interest can also be significantly less than 1% of the total absorption, and therefore serious contamination of the data can arise from the presence of characteristic lines in the incident spectrum.

A demonstration of this problem is given in figure 3.6. Here the absorption coefficient of Cu was measured near the WL quartet, which is 600 to 1000 eV above the Cu K edge. The difference between the

various curves is the amount of lead tape placed in the peripheral regions of the sample. The derivative shape predicted by equation 3.6 is clearly seen. Note that in some cases even comparatively weak lines can produce sizeable effects.

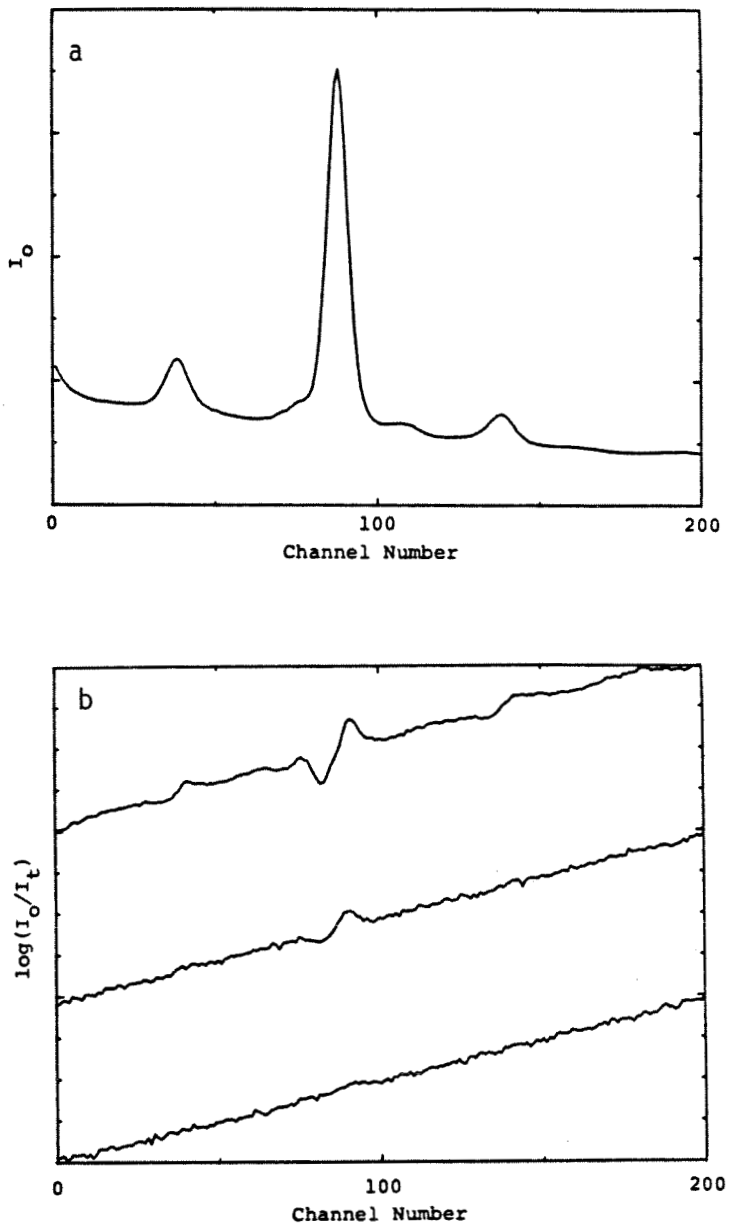

Figure 3.6 Detector nonlinearities in the region of the W L multiplet. a). Incident intensity as a function of energy. b). Unscaled absorptance. Different curves correspond to different amounts of lead tape at the periphery of the sample.

4 EXPERIMENTAL RESULTS AND ANALYSIS

4.1 La-Ga ALLOY SYSTEM

The bulk of the work for this thesis has been performed on binary metallic alloys from the La-Ga system. The phase diagram for this system is typical of a large number of glass forming systems and is shown in figure 4.1. The canonical deep eutectic appears at a composition of 20 % Ga, and, with the exception of the phase La_3Ga, all crystalline compounds in the system have at least some of the constituent Ga atoms in the trigonal prisms of La atoms used by Gaskell in his model of amorphous metallic structure. The glass forming region of this system has been reported to extend from 16 to 28% Ga [4.2], and the current study investigates glasses with 20, 24 and 28% Ga. The theoretical scattering functions tabulated by Teo and Lee[4.3] have been used in the analysis of the EXAFS spectra collected for these amorphous samples. However, first a study of one of the crystalline compounds of this system was undertaken to determine the function $S_o^2(k)$ and an appropriate value for the threshold energy E_o.

The compound Ga_2La was chosen since, among those in the phase diagram, it is the easiest to work with experimentally. This compound has the Al_2B structure which is described diagrammatically in figure 4.2. In line with what was mentioned above, the basic structural unit of this compound is a pair of La trigonal prisms, sharing a common face, with a Ga atom situated in each prism. In this structure each Ga atom has three in-plane Ga neighbours as well as the six La neighbours forming the trigonal prism. The Ga neighbours are at a distance of 2.494 A, indicating a degree of covalency in the bonding between these atoms, whereas the La atoms are at a distance of 3.331A

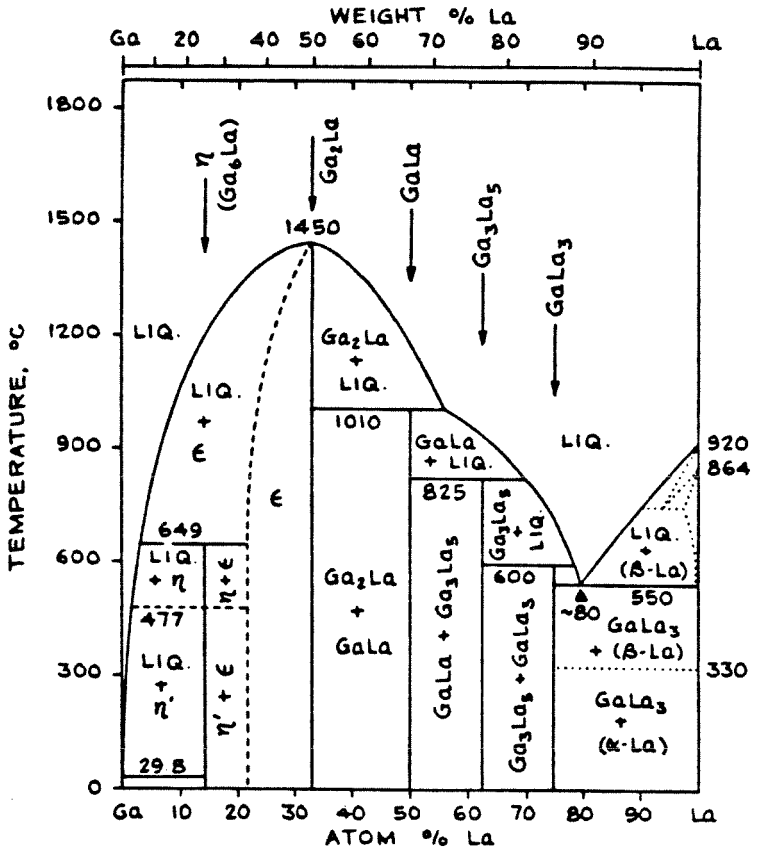

Figure 4.1 Phase diagram for the La-Ga alloy system. (Taken from reference 4.1).

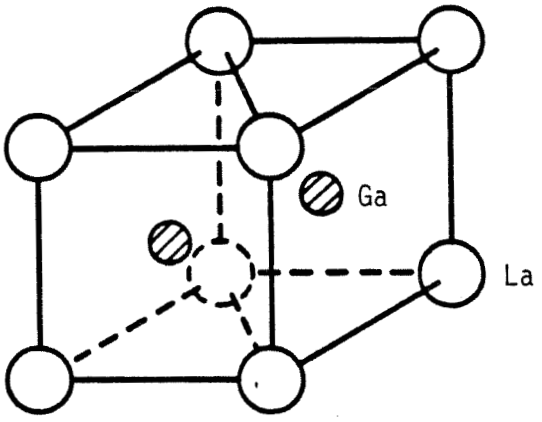

(a)

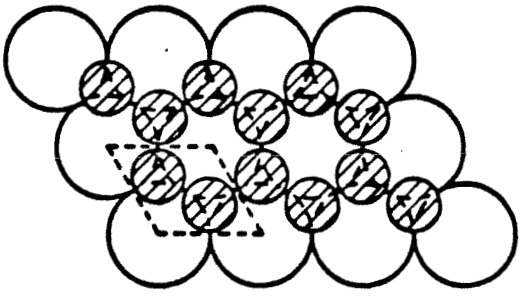

(b)

Figure 4.2 Basic unit, and arrangement of these units, in x-Ga_2La (AlB_2 structure).

which is roughly the sum of the Goldschmidt radii of the two atoms.

EXAFS spectra for this material were measured on powder samples whose preparation was described in chapter 3. The resulting spectrum is displayed in figure 4.3 along with the window applied to the data before computation of the Fourier transform. The wave vector axis used in this figure was constructed with the threshold energy set equal to 10.376 keV, which is 7 eV above the inflection point of the measured absorption edge. Figure 4.4 displays the magnitude of the Fourier transform obtained from the data given in figure 4.3. It is apparent from this figure that the La peak at about 3.0 A could be seriously contaminated by the side lobe contributions from the main Ga peak at 2.3 A, even though the input to the transform was weighted with k^2 and a tapered window was applied to the spectrum before computing the transform. For this reason the measurement of $S_o^2(k)$ and E_o was based on the Ga shell in Ga_2La, even though the Ga EXAFS in the glasses was expected to be dominated by La neighbours.

The contribution of the Ga shell to the measured EXAFS was isolated using the window shown in figure 4.4, and the resulting band pass filtered EXAFS spectrum is shown in figure 4.5, along with the fit obtained for this spectrum using equation (2.10) and the scattering functions of Teo and Lee[4.3]. In performing this fit the resolution of the spectrometer was accounted for in the approximate manner suggested by Lengeler and Eisenberger [4.4]. The selection of optimal values for the parameters in the model used was achieved using the general "Variable Metric" algorithm of Fletcher and Powell[4.5]. It was found that the fitting procedure used could easily become trapped in local minima. Care must therefore be taken to investigate

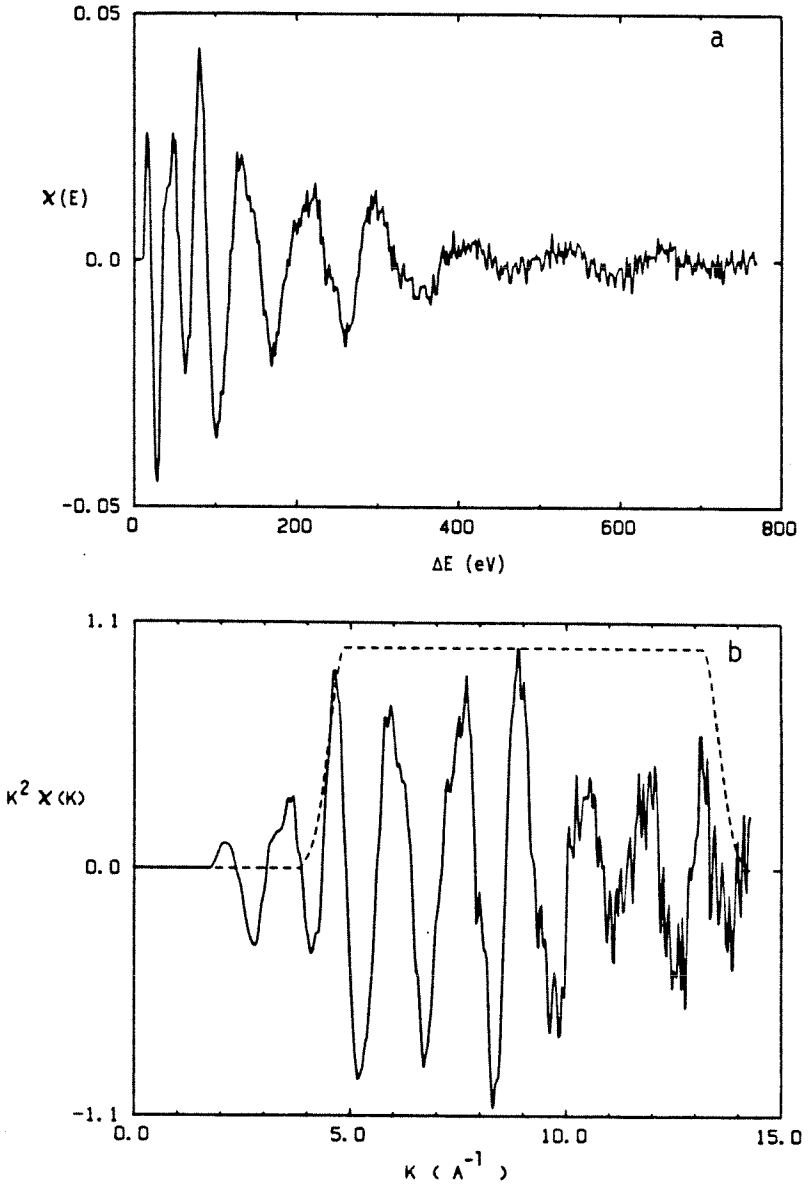

Figure 4.3 Ga edge EXAFS spectrum found for crystalline Ga_2La. a). χ as measured. b). $k^2\chi(K)$ assuming that E_o = 10.376 keV. Dashed line in b). shows the window applied before computation of the periodogram.

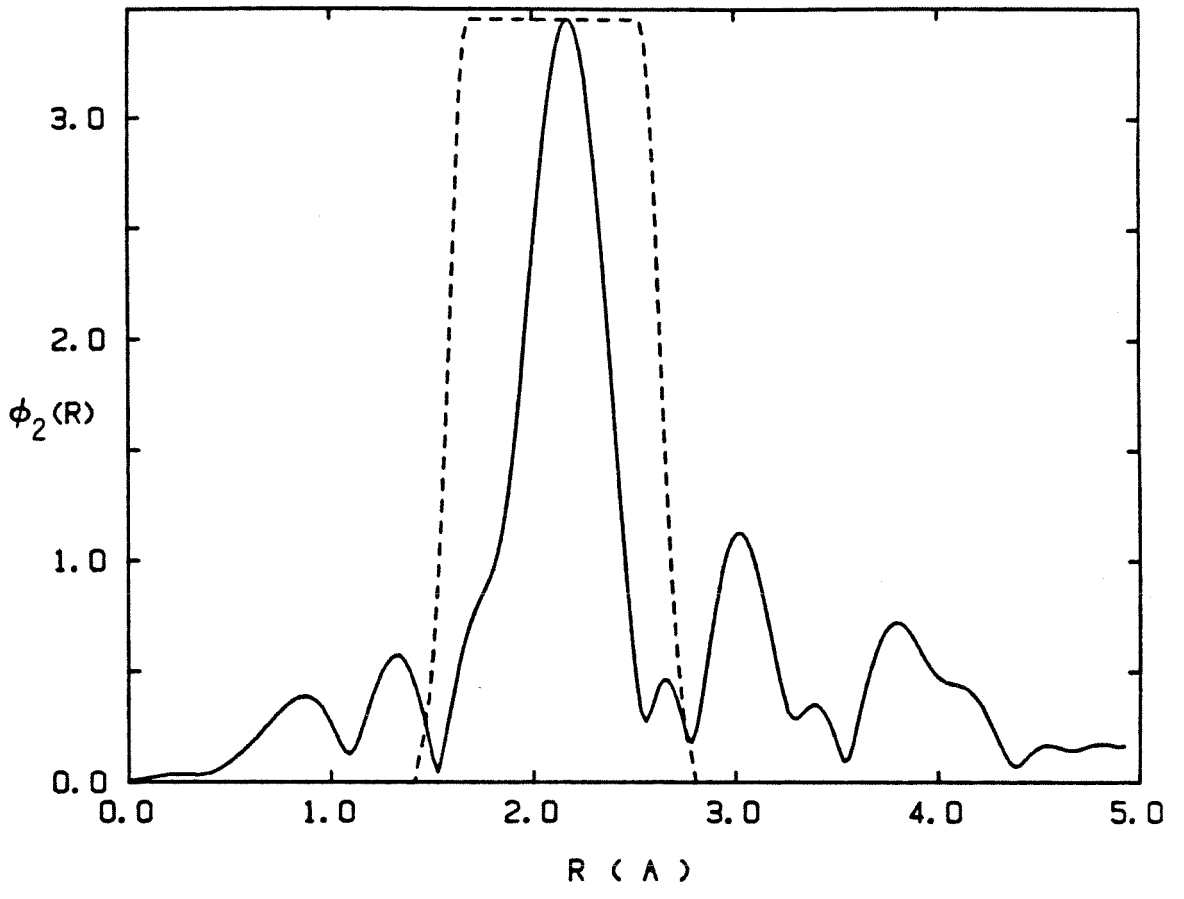

Figure 4.4 Magnitude of the Fourier transform (periodogram) of the EXAFS for Ga_2La, computed after k^2 weighting was applied to the spectrum of figure 4.3.

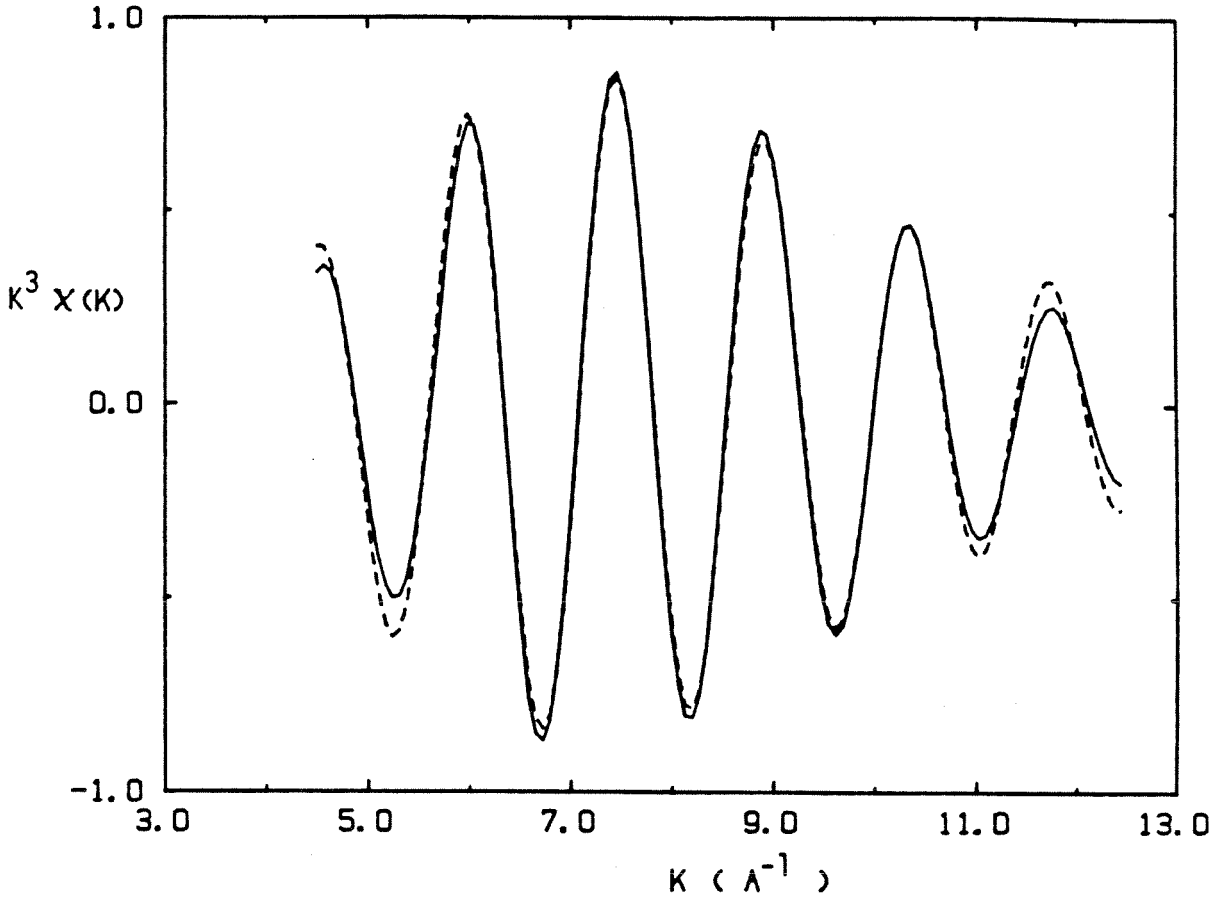

Figure 4.5 EXAFS due to first shell of 3 Ga neighbours in x-Ga_2La (dashed line), and fit obtained with the parameter values given in table 4.1 (solid line).

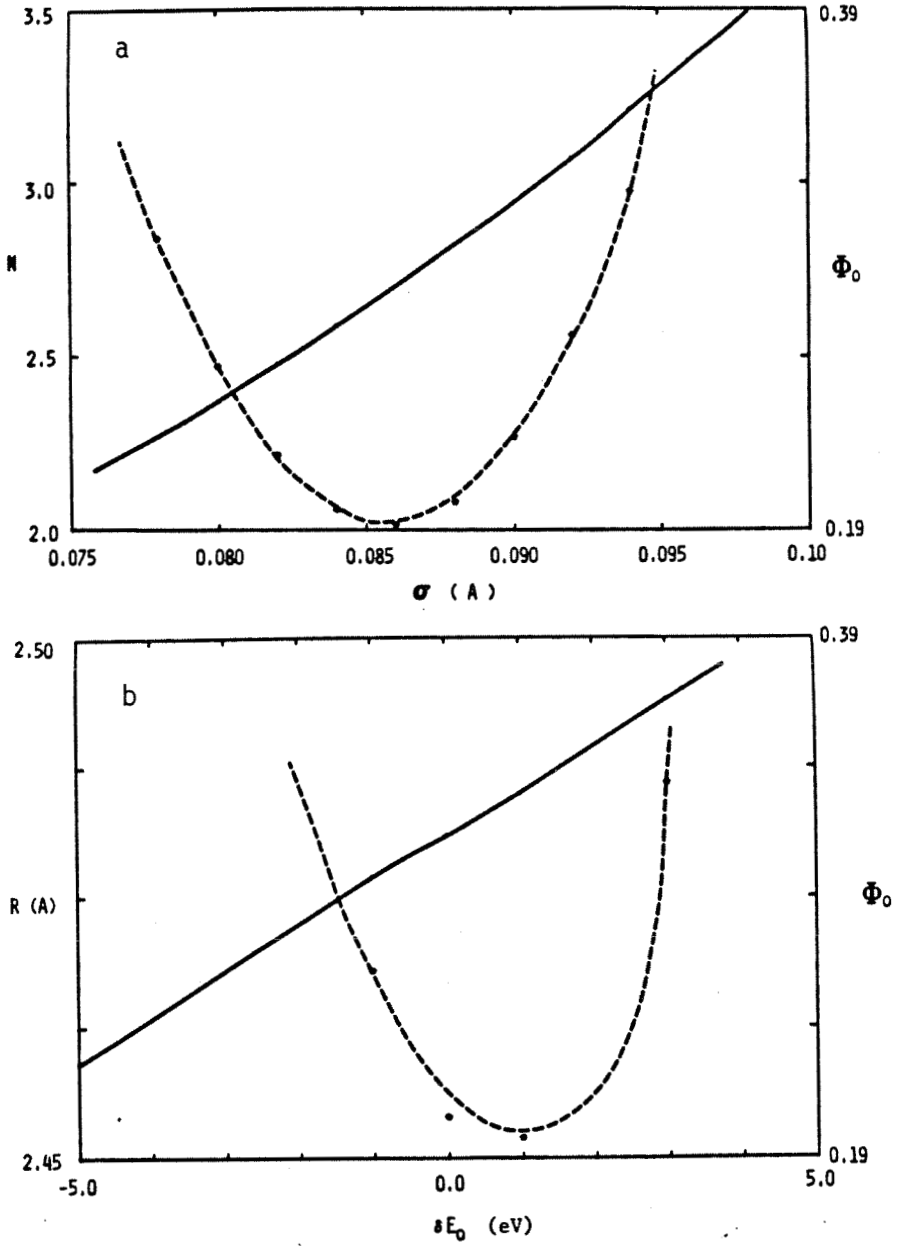

Figure 4.6 Parameter correlation in x-Ga_2La. a). Solid line gives optimal N as a function of σ. Dashed line gives the variation of the fit functional.
b). Solid line gives the optimal R as a function of δE_o. Dashed line shows variation of the fit functional.

a large area of parameter space by systematically choosing various initial parameter values for the search. To facilitate this it was found most useful to keep the values of σ and E_o fixed during any given fit, and to let the program find the optimal values of N and R corresponding to the selected values of σ and E_o. Under these circumstances the fit was found to be far less susceptible to local minima, and as a result the physically meaningful region of parameter space could be searched quite efficiently by selecting a wide range of values for σ and E_o. An indication of the correlation between the various parameters in the fit is also directly obtained in this type of search. As expected for a symmetric shell there is virtually no correlation between the width and the position of the peak, with some correlation being noted between E_o and R, and a great deal of correlation between σ and N. Figure 4.6 displays this correlation and the behaviour of the error in the fit (measured as simply the sum of squared errors for a subset of the data) as a function of σ and E_o.

At the time that the optimal values for the physical parameters are determined, the data are expressed as a function of a wave vector (k), computed with respect to a threshold energy which was selected at an earlier stage of the analysis (say E_{th}). Therefore in the optimization program a parameter δE_o is used to construct a perturbed k axis that is equivalent to an axis which would be found from using a value of $E_o = E_{th} + \delta E_o$ at that earlier stage of the analysis. The discussion that follows will use either the notation E_o or δE_o interchangeably.

The results of this procedure are summarized in table 4.1, which appears on the following page.

TABLE 4.1

Parameters obtained for the Ga shell of neighbours in x-Ga_2La

N	σ	R_o	δE_o
2.7	0.086	2.485	1.0

For these results the functional used in determining the fit was: $\Phi_o = \sum_i (f_i - d_i)^2$, where the sum is over every other data point, d_i. This type of decimation of the data was used in order to save computer time and was generally found not to affect the results significantly. It should be noted at this time that the distance given in the above table is within 0.01 A of the known Ga-Ga distance in this material, and the value found for N is 10% smaller than the known value of 3 for the coordination number. These discrepancies are a reflection of the accuracy of the Teo and Lee computations for the phase shifts and of the many body effects mentioned in chapter 2.

As mentioned in section 2.3, it is possible to extract separately the amplitude and phase functions for a given shell's contribution to an EXAFS spectrum. Figure 4.7 compares the results of performing this extraction, using the known values of 3 and 2.494 for N and R respectively, with the functions computed by Teo and Lee for a Ga-Ga pair of atoms. The computer program used in computing the phase from an experimental spectrum introduces an essentially arbitrary additional term equal to a multiple of π, corresponding to a selected branch of

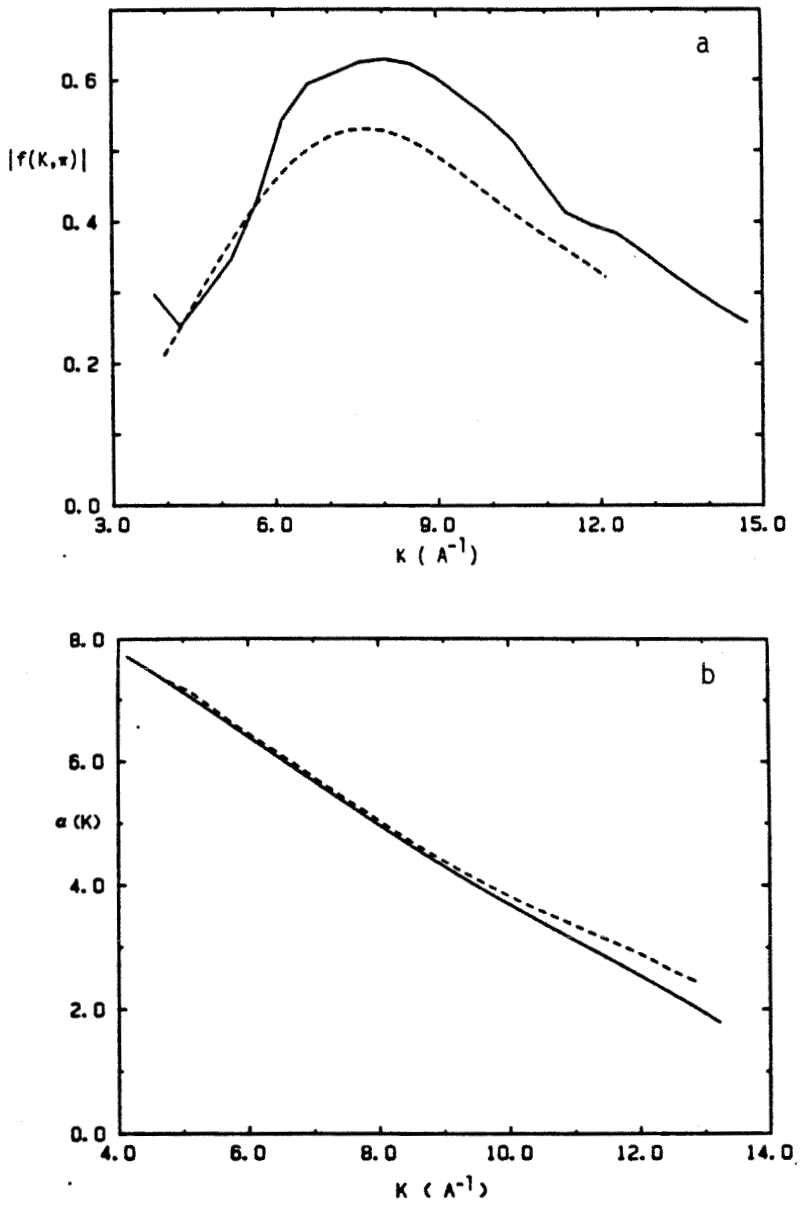

Figure 4.7 Comparison of experimental (dashed lines), and theoretical (solid lines) scattering functions.

a). Ga back-scattering amplitude $|f(k,\pi)|$.

b). Ga-Ga pair phase shift $\alpha(k)$.

the arctangent, and hence some multiple of π must in general be added to an experimentally determined phase function before it is compared to a given calculation. After such a term has been added, figure 4.7 displays excellent agreement between the calculated and measured phases. As should be expected, the agreement is not as good for the amplitudes, and it is assumed that the discrepancy is entirely due to the factor $S_o^2(k)$.

Looking at the comparison of amplitudes given in figure 4.7, it is clear that $S_o^2(k)$ must be smaller at large k than it is at small k, since the experimental curve falls below the theoretical one as k increases. If the consequences of this are considered it becomes clear that the results given in table 4.1 undoubtedly overestimate the value for σ (since it is the only parameter in the fit controlling the drop off at large k). Hence, in computing $S_o^2(k)$ for future use a value of σ will be chosen which is somewhat less than that given in table 4.1. In fact two values were considered, 0.084 and 0.079. Figure 4.8 displays $S_o^2(k)$ curves computed assuming each of these two values for σ. The shape of the curve is very similar for both cases but it should be noted that the curve corresponding to σ =0.084 actually takes on unphysical (i.e. greater than 1) values near 6 A^{-1}. Although the experimental error is of the same order as the amount by which this curve exceeds the physical limit of 1, using this curve in future computations would seem imprudent at best since it would obviously result in a systematic underestimate of coordination numbers. Furthermore, the curve corresponding to σ =0.079 has a peak value very similar to that found by Stern et al.[4.6] in measurements on GaAs samples. Consequently this latter curve is the one that will

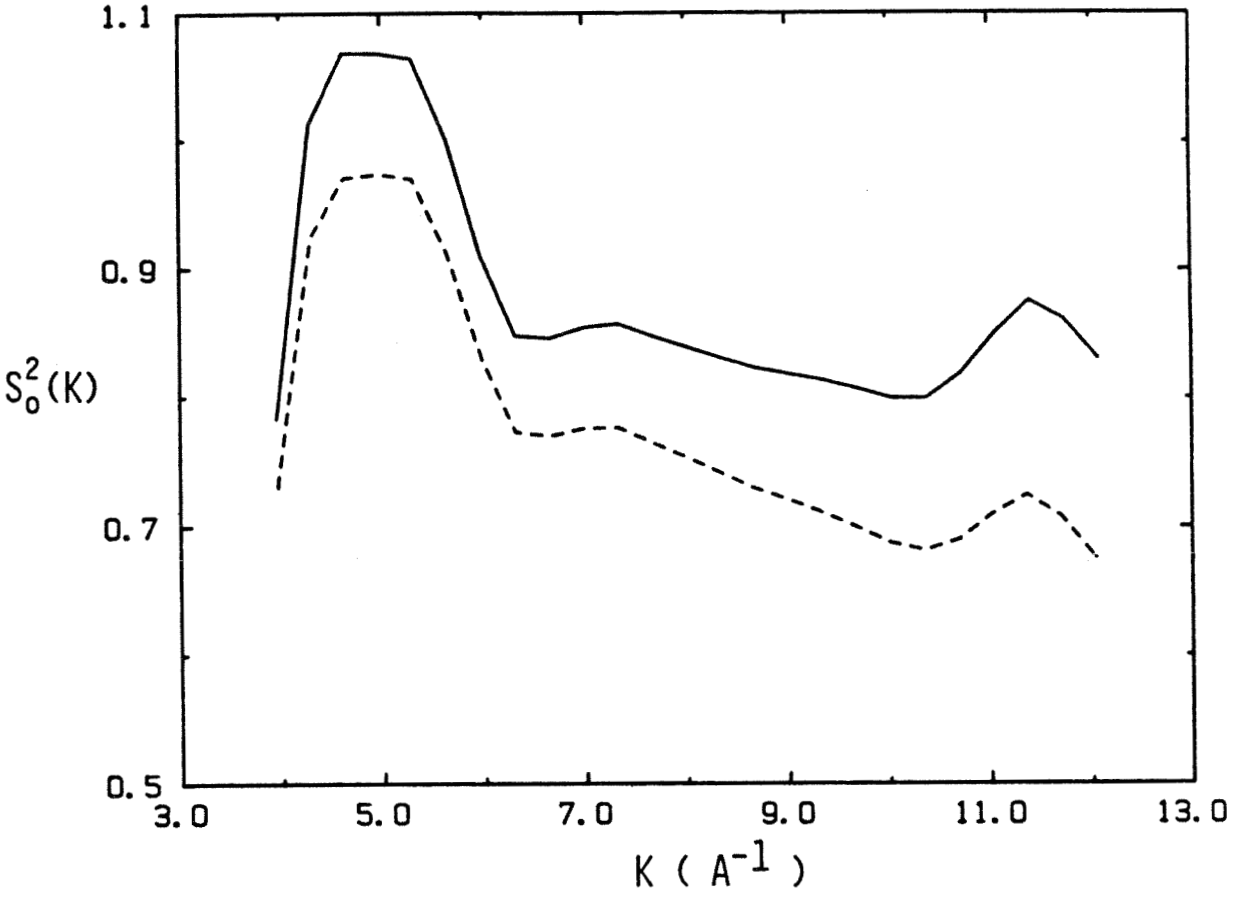

Figure 4.8 Overlap integral, $S_o^2(k)$, computed for Ga edge in Ga_2La assuming $\sigma = 0.084$ (solid line), and $\sigma = 0.079$ (dashed line).

be taken to define $S_o^2(k)$ in the analysis that follows.

4.2 $La_{1-x}Ga_x$ GLASSES: SINGLE SHELL MODEL

Figure 4.9 displays the spectra obtained for glasses of all 3 compositions studied. In subsequent discussion these spectra will be referred to by using the notation x=n to indicate the Ga concentration of the sample under consideration. Although the three curves look very much alike it will be seen that significant differences can be found between them. For the moment, however, the discussion will focus only on the data for x=20.

The first thing to note in comparing the data for the amorphous samples (figure 4.9) with that shown earlier for the crystalline compound Ga_2La is that the amplitude of the spectra for the amorphous samples fall off much more rapidly with energy than did the spectrum for the crystalline compound Ga_2La. This is a confirmation of the inability of the micro-crystalline models to correctly describe the structure of metallic glasses. Since EXAFS is truly a local probe of the structure, if any significant fraction of the Ga atoms in the sample were in identical, well-defined sites, as would occur in a micro-crystalline picture of the structure, then the observed spectrum should not be as strongly damped as figure 4.9 shows it to be.

The Fourier transform of the data for this composition (computed after the application of a k^3 weighting factor) is shown in figure 4.10a. Comparing this figure to figure 4.4 it would be natural to assume that the peak near 3.0 A indicates a shell of La neighbours while that near 2.2 A indicates a shell of Ga neighbours. However, this simple interpretation of the transform is seen to be inadequate

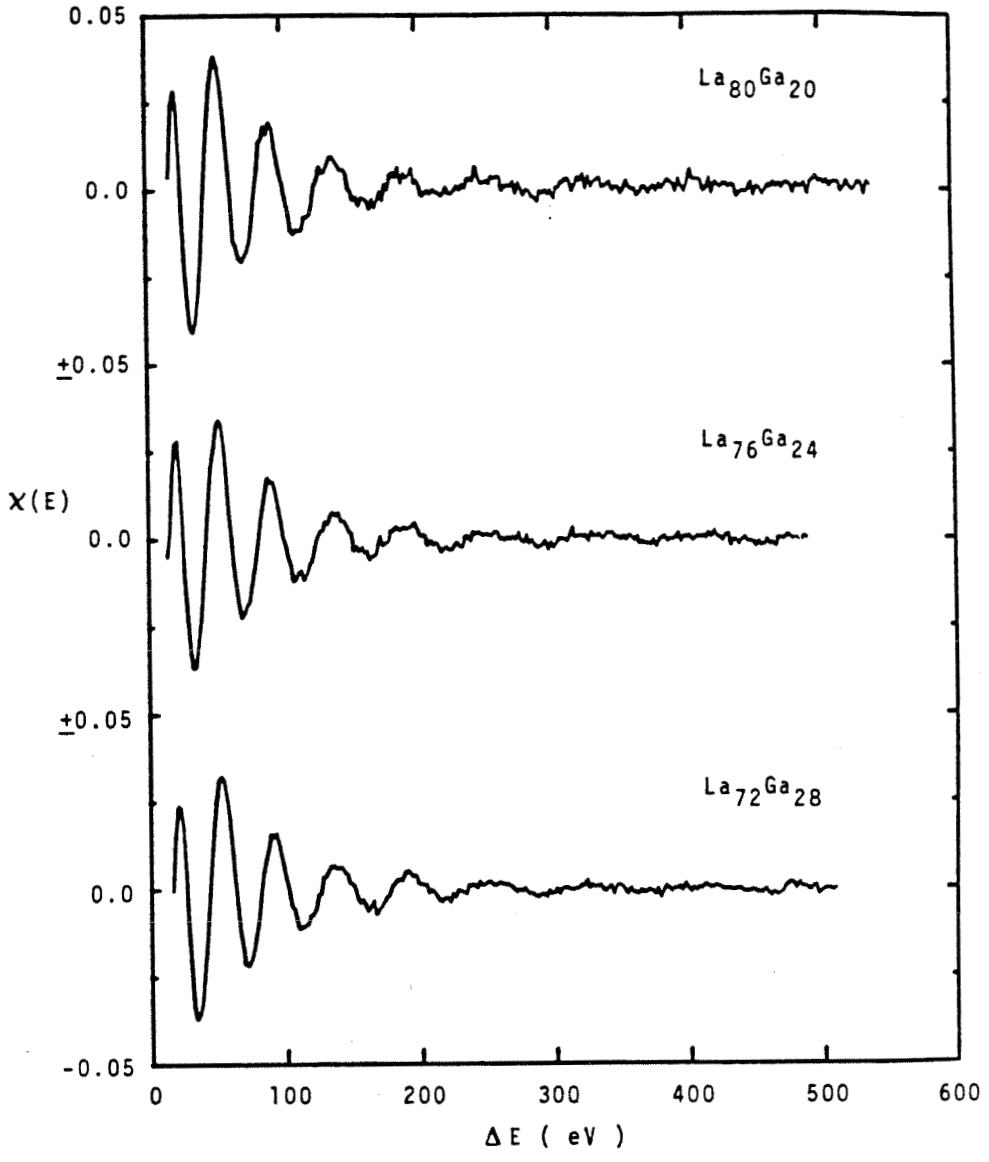

Figure 4.9 EXAFS spectra as a function of energy above the initially selected threshold of 10.3765 keV.

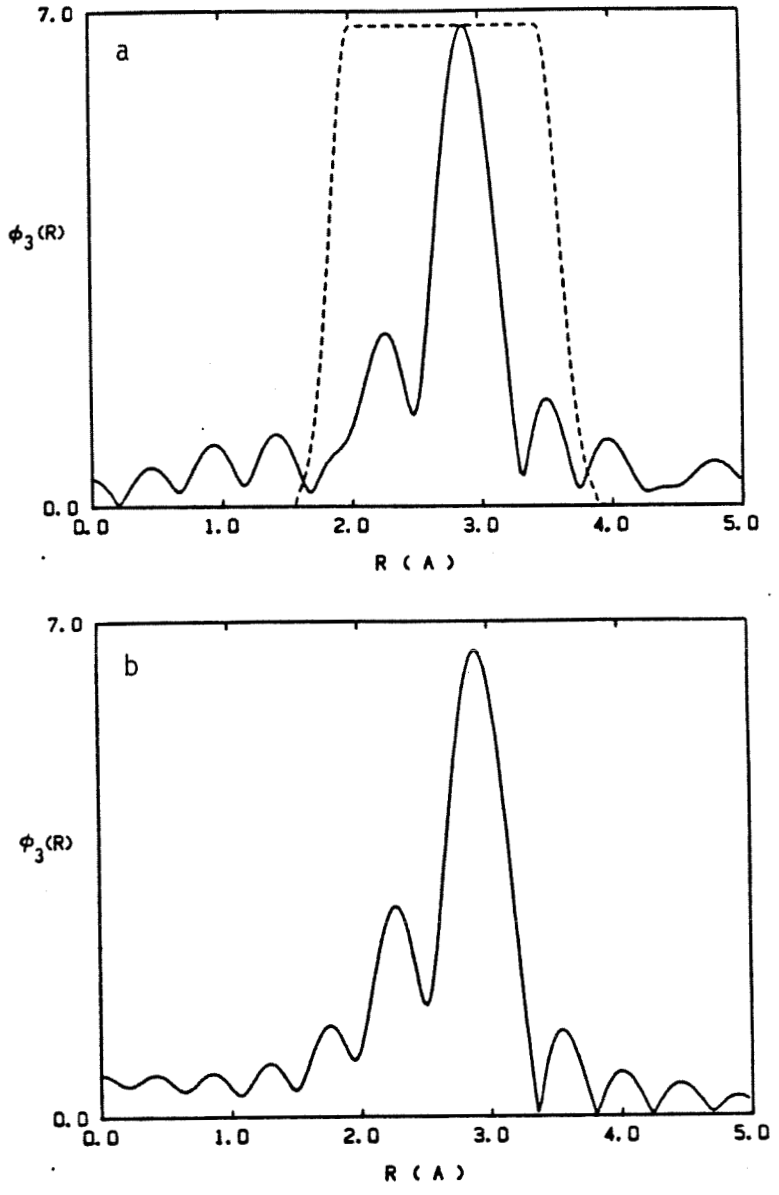

Figure 4.10 Periodograms of: a). Experimental spectrum for x=20 b). Simulated spectrum for a single La shell about an absorbing Ga atom.

when figure 4.10b is also considered. This figure shows the transform computed from a simulated EXAFS spectrum which was constructed assuming only a shell of La neighbours around the absorbing Ga atom. It is seen that the peak near 2.2 A is still present in the model even when no Ga neighbours were included! This emphasizes the fact that even comparatively strong peaks in the transform do not necessarily correspond to physical structures in the sample, and therefore care must be taken when interpreting the transform as a radial density function.

The reason for the anomalous peak is to be found in the complicated nature of the scattering functions for La, which are displayed in figure 4.11. This type of enhanced side lobe structure has been noted before [4.7], however earlier authors have attributed it only to the oscillatory nature of the back-scattering amplitude of a heavy atom (such as La). This would produce side bands in the Fourier transform in much the same way that amplitude modulation produces side bands in the spectrum of radio transmissions. However such modulation should produce a symmetric side lobe structure, i.e. enhanced side lobes of approximately equal size should be seen on either side of the main peak, not just on the low R side as seen in figure 4.10. In fact it is the convex nature of the nonlinearity in the scattering phase shift for the Ga-La pair that produces the low R asymmetry in the side lobe structure, although the oscillating nature of the back-scattering amplitude certainly contributes to the size of the effect.

Explanations for the effect aside however, the preceding discussion makes abundantly clear that if the EXAFS spectrum for this alloy contains contributions from both La and Ga neighbours, these contribu-

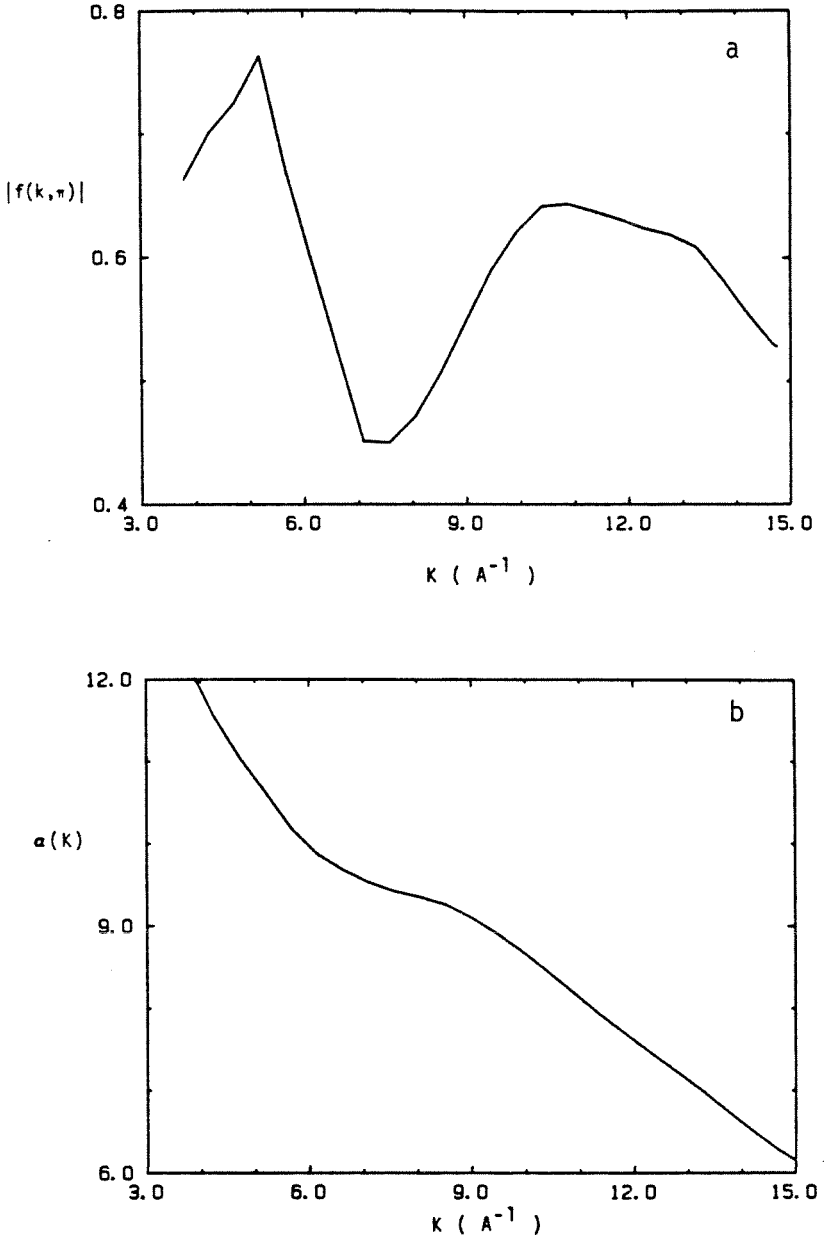

Figure 4.11 Theoretical scattering functions for a Ga-La pair.

a). La back-scattering amplitude (in Angstroms).

b). Total scattering phase shift (in radians).

Theoretical functions are taken from reference 4.3.

tions cannot be separately assessed by successively isolating the two main peaks in the Fourier transform. Consequently the analysis proceeds by applying the broad window displayed in figure 4.10a and testing whether a contribution from some Ga neighbours is needed to adequately model the resulting band-passed EXAFS spectrum. Consideration of figure 4.10 also brings out another point which has been all but ignored in the literature. The transform displayed shows no obvious physical structure beyond the primary peak and its low R side band (compare figures 10a and 10b). This is obviously due to the fact that in an amorphous material the higher order coordination shells are much broader than are those in a crystal and as a result the contribution of these shells is damped to the point where it essentially gets lost in the noise. Hence the primary effect of applying the window shown in figure 4.10 is that of a band pass filter acting on noise, rather than the explicit isolation of one main frequency band from a set of two or three. This noise rejection action of Fourier filtering has been completely ignored in the EXAFS literature, however it will be seen that attention should be given to this feature when analyzing the data.

In an earlier publication the analysis of the spectrum for x=20 was discussed, and a comparison was made between the results obtained when three different distributions were chosen for the Ga-La coordination shell of this glass[4.8]. Rather than repeat those results here, this discussion will be restricted to studies based on the peak shape which was found to be most satisfactory in that earlier work. The shape in question is that described by equation (2.12) with n=2. (See figure 2.6).

Since Ga is the minority constituent, and since the diffraction experiments by Williams (see chapter 1) indicated strong chemical ordering in these glasses, the EXAFS spectra were first analyzed under the assumption that only La neighbours are to be found around the absorbing Ga atom. The results of fitting such a model to the data for x=20 are summarized in figure 4.12. In constructing the k- axis for this spectrum E_o was originally chosen to be 10.3765 keV, or roughly 9 eV above the inflection point in the measured edge transition. As was done for the crystalline sample discussed in the previous section, the fitting proceeded by fixing the two parameters δE_o and σ at various values and using the optimization program to find the corresponding optimal values for N and R_o. This procedure was particularly necessary for the spectrum from the amorphous samples because of the strong correlation present between the phase and amplitude of the expression given in equation (2.11). Figure 4.12 displays this correlation by showing the optimal value obtained for the fit functional Φ_o at various selected E_o's. Values of δE_o between -5 eV and +5 eV were selected, and for each of these a curve giving the variation of N with σ was constructed on the basis of fits performed for various fixed σ. At all values chosen for δE_o the curve of N vs. σ was found to be essentially the same. The solid curve in figure 4.12 shows this N-σ correlation, while the error bars along this curve indicate the variation in the position of the curve as δE_o is allowed to vary between -3 eV and +3 eV. For each selected value of δE_o there naturally exists a curve showing the variation of the value of the fit functional as σ is allowed to vary. Two representative examples of this variation are given as dashed lines in the figure (for

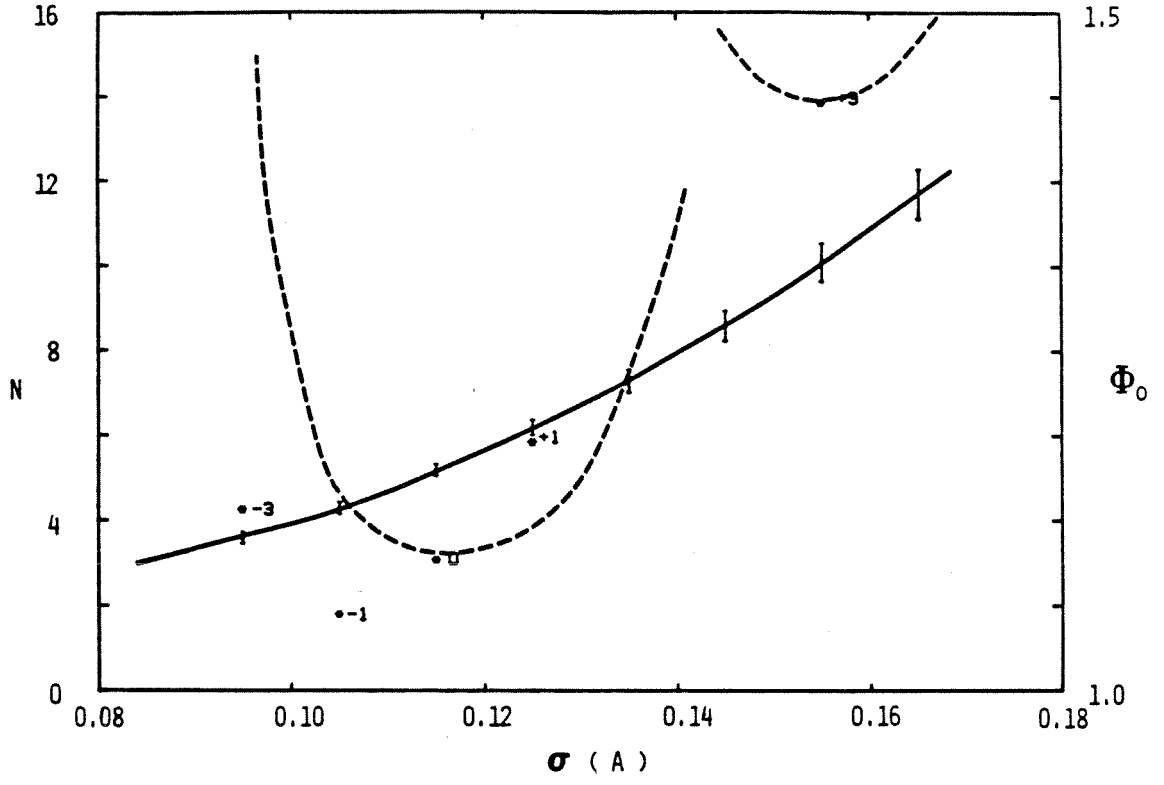

Figure 4.12 Correlation between σ and N for various E_o.
* E gives the optimal position of the Φ_o vs σ curve for δE_o = E. (dashed lines show the Φ_o curve for δE_o = 0.0 and 3.0 eV. See text for details)

δE_o= 0 eV and +3 eV). For other values of δE_o the curve of Φ_o vs. σ is represented by a single point (*) at the position where this curve reaches its minimum. It is seen that although the basic trend of N vs. σ does not vary with the threshold energy, the optimal position along this trend does vary considerably. It is also noted that if the value of E_o is chosen simply on the basis of a best fit criterion, then an unphysically small value of 4.3 is obtained for the coordination number of the absorbing atom.

Recall from the discussion of chapter 2 that the motivation for choosing E_o on the basis of the best fit was that an artificially good fit could not be obtained at an incorrect value of R as a result of allowing E_o to vary. This, however, assumes a symmetrically shaped distribution function, so that Σ of equation (2.11) is zero and the correlation between N, σ and E_o is negligible. As seen from equation (2.11), however, both E_o and Σ influence the nonlinearity of the sinusoid phase, and consequently such correlations cannot be neglected. Furthermore, the actual distribution of the sample considered will , in all likelihood, be slightly different from the model assumed in the fit, and an incorrect value for E_o might provide a fortuitous cancellation of the effects of this difference. Therefore the argument presented to support the treatment of E_o as a free parameter in the fitting process ceases to be valid in the case where an asymmetric peak shape is considered. For this reason the practice of choosing E_o on the basis of obtaining the best fit to a given set of data should not be used when the system under study is modeled with an asymmetric distribution. By the same token, the other methods of choosing E_o on the basis of linearizing the phase of the sinusoid in

the EXAFS expression cannot be used unless the structural problem has already been solved so that the contribution of Σ may be properly accounted for. Of the methods discussed in section 2.5 therefore, none is suitable for the experimental data being considered in this chapter. For this reason the remainder of the discussion in this chapter will be based on a threshold energy of 10.377 keV (corresponding to δE_o=0.5 eV in figure 4.12). This value is chosen based on the fact that it was found to be the best value in the crystalline standard compound.

The results obtained for a single shell fit under the above assumption for the threshold energy are summarized in table 4.2 and figure 4.13 for all three compositions studied. In obtaining these results the data were defined only on a relatively restricted interval in k-space (4.0 to 10.0 A^{-1}) due to the rapidly decaying signal, and the fit functional was the same as was used in the previous section for Ga_2La. In this case using half of the data resulted in a fit to approximately 80 points.

TABLE 4.2

Parameters obtained for a single La shell model for the Ga environment in $La_{1-x}Ga_x$ glasses.

x	N	σ	R_o	Φ_o
20	6.2	0.125	3.00	1.4
24	8.9	0.155	2.97	2.3
28	5.5	0.125	3.00	2.9

These values for the parameters were obtained using the dashed

curve given in figure 4.8 for the function $S_o^2(k)$. Roughly the same values for the parameters were obtained if this factor was taken to be 1.0 (with the exception of the width parameter, which was always approximately 10% larger if a constant S_o^2 was assumed). However the values of the fit functional invariably were larger if a constant overlap factor was assumed.

It is clear from the above table that the fit obtained for the $La_{80}Ga_{20}$ glass is much better than that obtained for the other two compositions, even though the noise level was less in the latter two spectra. This implies that the local environment of the Ga atoms in these materials does in fact change as the concentration of Ga is increased. At this stage, however, the analysis is unable to identify what form these changes have, although two possible explanations immediately present themselves. First of all, it is possible that as the concentration of Ga increases, some Ga-Ga contacts start to occur and the inadequacy of the above fits may be related to the neglect of such contributions to the spectrum in the model used. Alternatively, as the concentration of Ga is increased it is possible that, beyond a certain concentration between 20 and 24%, the effect of more Ga is to distort the prevailing La network in the structure, creating a consequent distortion of the local La shell about each Ga. Each of these two possibilities will be discussed in the next section.

Before proceeding on to the next section, however, a few more words are needed about the one shell fits. Most importantly it will be noted that the fit obtained for x=20 is not perfect, even though it is certainly superior to that seen at the other two compositions. The question then arises as to whether or not the errors in this fit are

due solely to the effects of noise in the original spectrum, or if the simple single La shell model inadequately describes this glass as well. To address this question a simulated EXAFS spectrum was constructed using a distribution given approximately by the parameters listed in table 4.2 for the x=20 data. Fifteen different noise realizations were then added to this simulated spectrum to provide fifteen simulated, noisy spectra. The level of noise chosen corresponded to a statistical fluctuation of .13% in a measured absorption coefficient, which is roughly the level seen in the data for x=20. Due to the amount of filtering and weighting that is applied to EXAFS spectra before actual physical parameters are determined, it is difficult to assess quantitatively the effect that noise in the measured spectrum has on the results obtained. However, when the noisy simulated spectra were processed in the same manner as were the experimental spectra, the fits obtained indicated that a value for the fit functional of about 1.5 ± 0.5 should be expected for the given level of noise. On this basis, therefore, it appears that the single La shell model for the Ga environment does adequately describe the measured spectrum at the composition x=20, but certainly not for x=24 or x=28.

From figure 4.12 the expected uncertainties for the parameters N and are ± 1.5 atoms and ± 0.02 A respectively (based on the points where the value of the fit functional increases by 30%). Using a similar criterion, the uncertainty in R_o is ± 0.02 A. Although not shown in the figure, the correlation between and R_o is such that the expected uncertainty in the position of the peak of the distribution is slightly less that the 0.06 A which might be expected from the

above discussion (recall that $R_{pk} = R_o + 2\sigma$). However these uncertainties neglect the possiblity of a systematic error which might be introduced by an incorrect choice for E_o. Table 4.3 lists the physical parameters found from optimal fits of various models to the three experimental spectra shown in figure 4.13. In this table the error intervals quoted account for the additional uncertainty introduced by the uncertainty in the threshold energy.

4.3 TWO SHELL MODELS

As indicated above the two most logical explanations for the failure of the single La shell model to describe the spectra measured for the alloys at x=24 and x=28 are that either the La distribution does not exactly follow the curve shown in figure 2.6 (as the previous section assumed), or there are, in fact, some Ga-Ga pairs in the glass even though none were indicated in the earlier diffraction experiment. In the discussion which follows each of these two models will be applied to the spectra obtained for the glasses with x=24 and x=28.

From table 4.2 it is apparent that a single La shell model of the Ga environment in the x=24 glass, while incomplete, does account fairly well for the major contribution to this environment (since the value of the fit functional is only about 50% larger than that expected). For this reason the majority of the effort expended in trying to find a better description, involved introducing a small perturbation onto the distribution found for the 1 shell model. Thus the first possibility mentioned above for the discrepancy in the 1 shell fit for this composition, was addressed by introducing a small

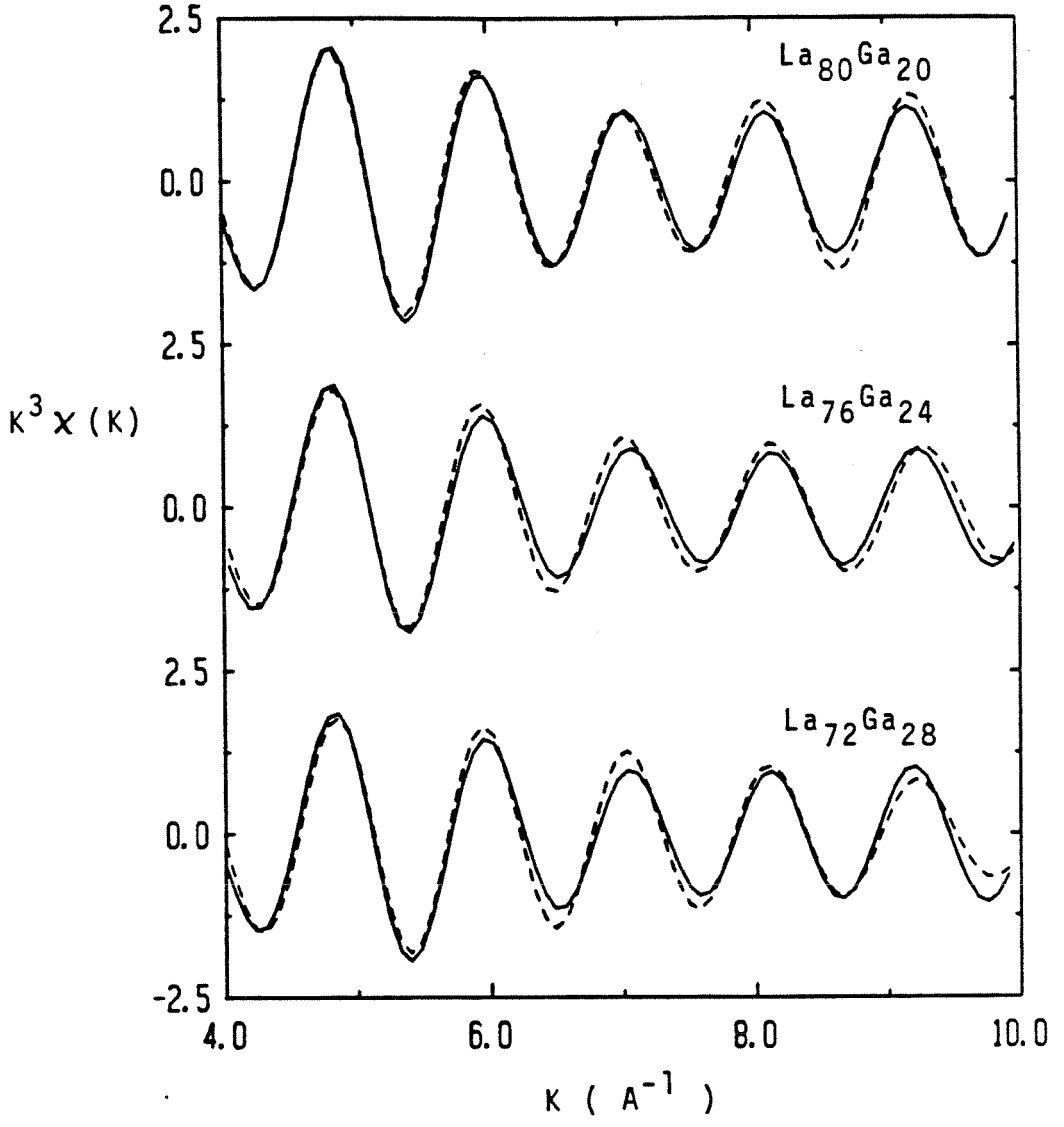

Figure 4.13 Best fits to filtered EXAFS spectra, based on a single La shell model for the Ga environment.

second subshell of La near the centre of the soft high R tail in the distribution of figure 2.6. This model will be referred to as a La doublet and the results obtained for this model are summarized in table 4.3, along with those found for the other cases discussed below. The introduction of such a second La subshell does indeed bring the value of the fit functional down to the region expected on the basis of the tests with the noisy simulations. The improvement in the fit is not particularly dramatic however, particularly considering the fact that the number of free parameters has doubled.

In contrast to the La doublet model, the model which assumes that some of the absorbing Ga atoms have Ga neighbours (referred to as the Ga pair model in subsequent discussion) does result in a dramatic improvement in the quality of the fit. In fact the value of the fit functional for this model is near the lower limit of the region of expected values, whereas the La doublet model gave a value closer to the upper limit of this range. It must be remembered, however, that, when noise is present in the data, a fit which produces too small a value for the fit functional is just as suspect as one which produces too large a value for this functional. Therefore this comparison of the two possible models is not truly able to distinguish between the two, even though one has produced a much "better fit". This point is also apparent if the two fits are viewed graphically as presented in figure 4.14. In this figure it is seen that the Ga-Ga pair model in fact achieves a smaller value of the fit functional primarily by following the data more closely at high k than does the La doublet model. However since the data have been weighted by k^3 the high k region of the filtered spectrum is subject to the greatest uncer-

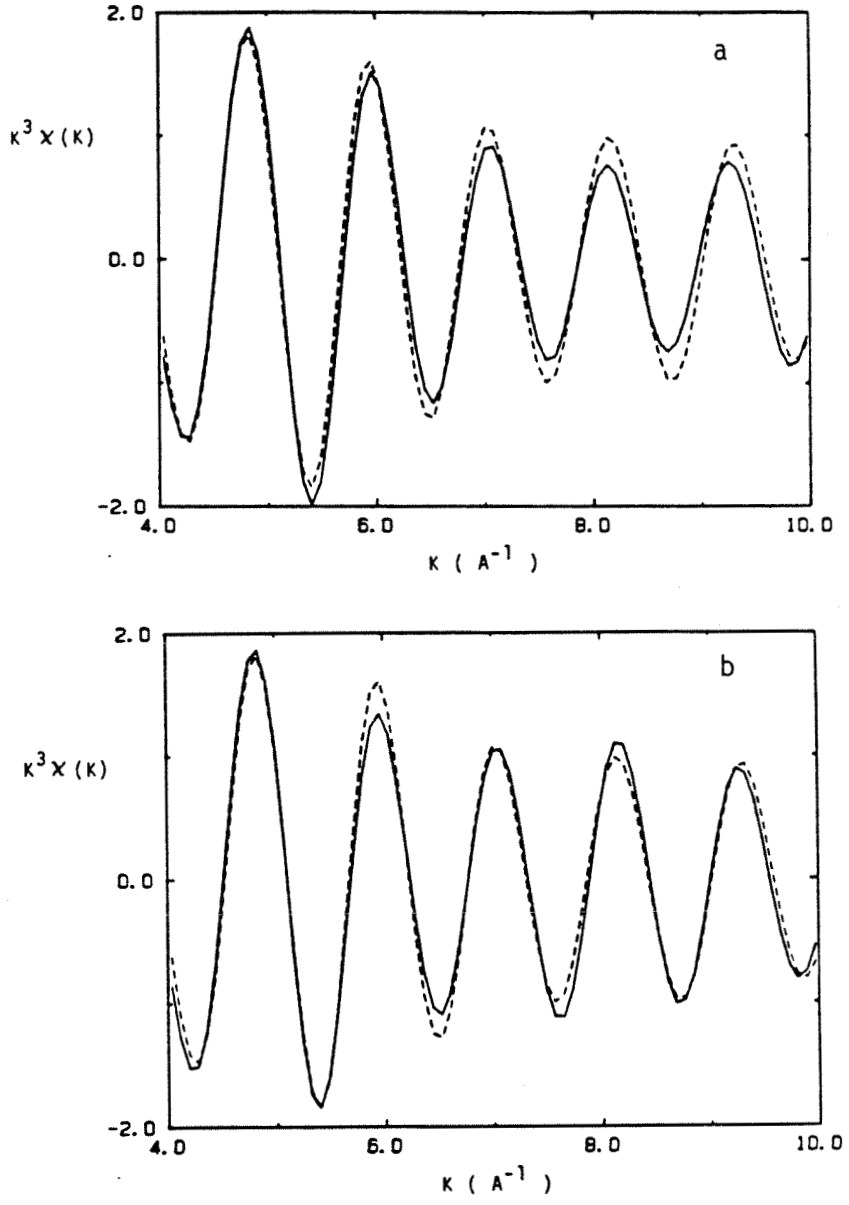

Figure 4.14 Best fits to filtered EXAFS spectrum for x=24 using a two shell model. a). La doublet model b). Ga pair model.

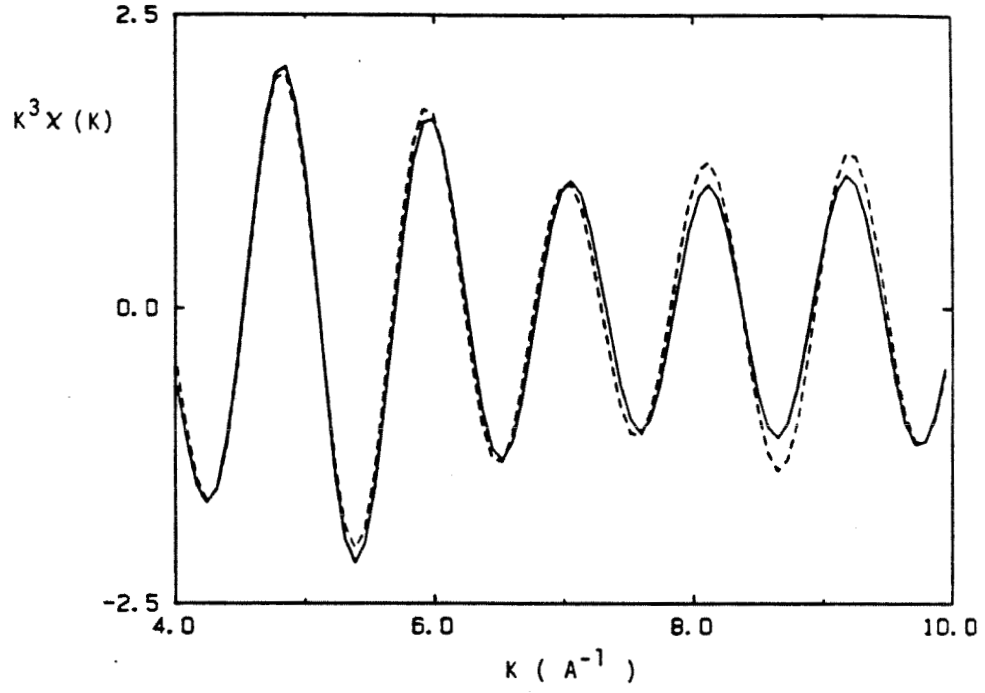

Figure 4.15 Best fit to filtered EXAFS spectrum for x=20 using a single La shell model.

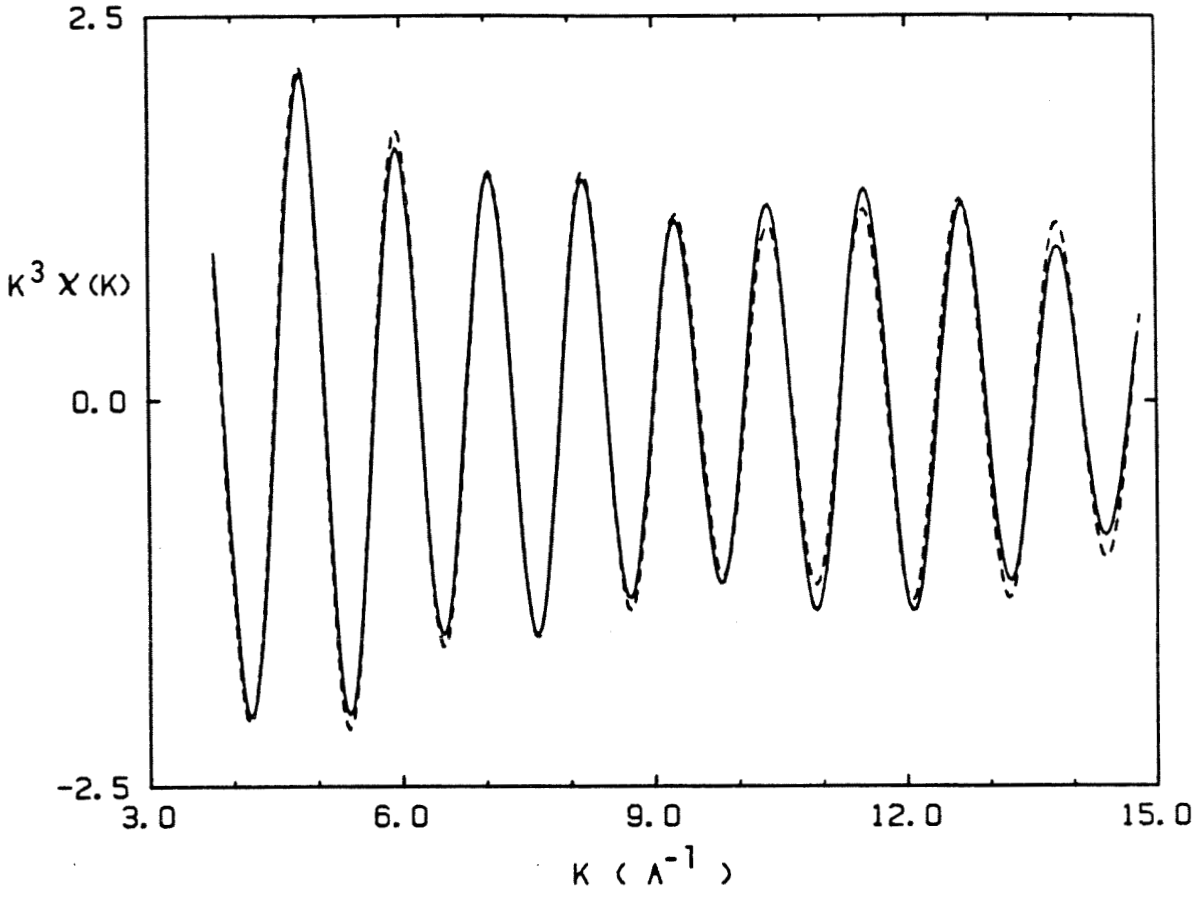

Figure 4.16 Simulated spectra for two possible local environments of Ga in $La_{76}Ga_{24}$. Solid line assumes a wide shell of 2.2 atoms while the dashed line assumes a narrow shell of 0.2 atoms. (See text for details).

tainty. In contrast to this, the 1 shell fit to the x=20 glass (reproduced in figure 4.15 for greater clarity) is seen to follow the data very well at low k and depart from the data somewhat at high k.

Table 4.3 does however indicate that the majority contribution to the spectrum at x=24 is the same, regardless of which model is assumed for the environment. In both cases the environment is dominated by approximately 9 La atoms at a distance of about 3.28 A. The best fit obtained using a model which allowed for Ga-Ga pairs contained only very few of these pairs (a coordination number of about 0.2 for Ga-Ga). However the correlation between the width of the distribution for these pairs and their number is so great that the value of the fit functional increases by only 30% if a rather broad distribution of up to 2 Ga neighbours is assumed for the absorbing Ga atom. Since the noise simulations of the previous section indicated that a 30% increase in the value of this functional could be expected simply on the basis of the noise in the data, this experiment is not adequate for an accurate measurement of the chemical short range order (CSRO) parameter. The uncertainties quoted in table 4.3 for this composition reflect this fact and were found in a manner analogous to that described above for the x=20 case.

Figure 4.16 demonstrates that extremely accurate measurements of EXAFS spectra will have to be made if the technique is to provide a reasonable measurement of the CSRO parameter in systems such as the one studied here. In this figure two simulated spectra are shown. In both cases the primary contribution to the spectrum is a shell of 9.3 La atoms just as indicated in table 4.3 for the glass at x=24. The two spectra differ only in the Ga shell assumed in the simulation. In

one case (dashed line) a distribution is assumed with N=0.2 but a width of 0.24 A, whereas in the second case (solid line) the distribution has N=2.2 with a width of 0.65 A. Clearly, in order to distinguish between these two curves it will be necessary to measure the spectra extremely accurately.

The results obtained by applying the two shell models discussed above to the spectrum for x=28 are shown graphically in figure 4.17. For this glass both of the models considered in this section provide an improvement over the result obtained with a single La shell fit, just as they did for x=24. In this case however each model provides a marginally inferior fit than it did for the glass at x=24. Also in contrast to the previous case is the fact that the two models indicate quite different values for the parameters describing the major contribution of the La shell. These facts would seem to indicate that neither model is accurately describing the La coordination of Ga at this composition. If this is the case, it is natural to suppose that allowing more freedom in the La shell of the model might be able to more closely approximate the true shape of the La distribution. However, in order to do this in the present context the number of free parameters would have to be increased to the stage where the extraction of meaningful physical information would be virtually impossible.

It is also possible that another model peak shape may be able to describe the local La arrangement found in this glass, however, finding the appropriate model is an impossible task in general. In chapter 5 an alternative method of analyzing EXAFS spectra is described which might be able to solve this problem. However, using the current method of analysis it appears that the only conclusion that

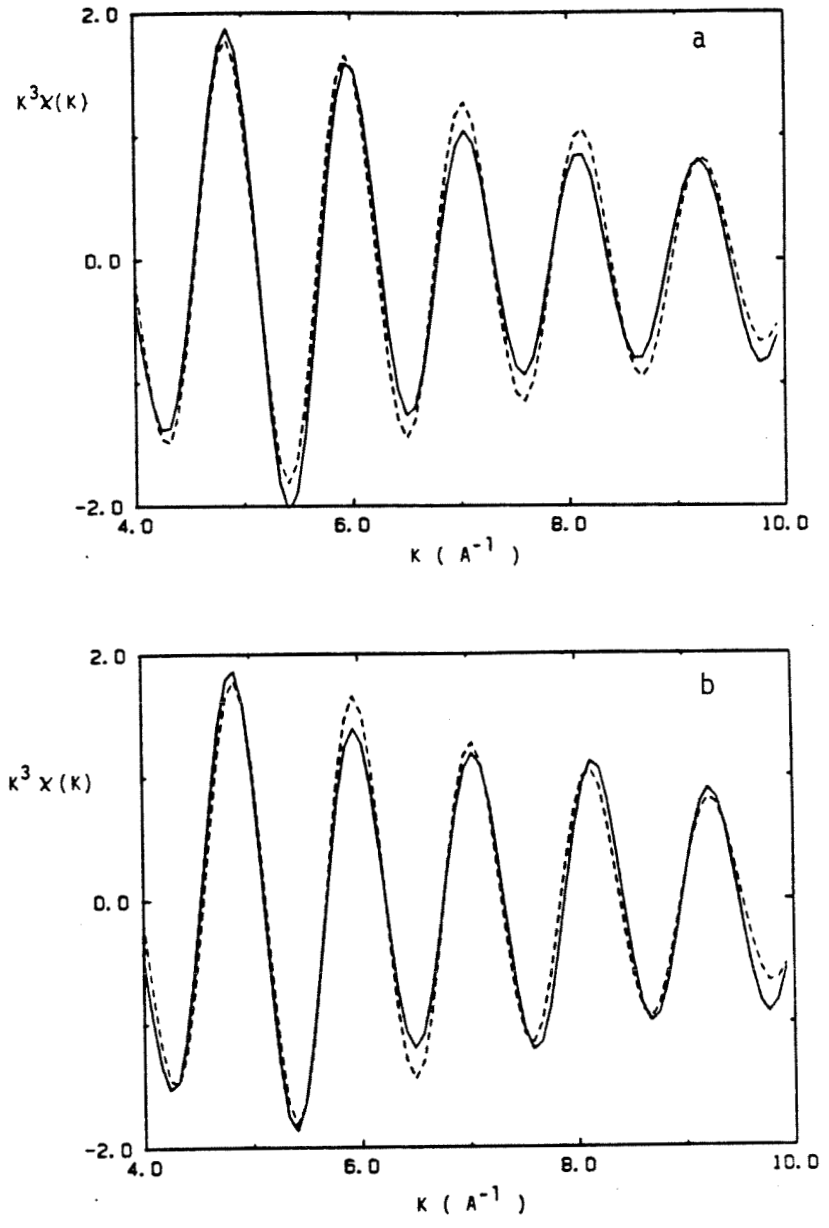

Figure 4.17 Best fits to filtered EXAFS spectrum for x=28 using two shell models. a). La doublet model b). Ga pair model.

TABLE 4.3

Summary of physical parameters found for La Ga glasses using EXAFS and X-ray diffraction.

x	Experiment	N_{La}	R_{La}	ΔR_{La}	N_{Ga}	R_{Ga}	ΔR_{Ga}	ϕ_o
20	Diffraction	7.8 ± 0.9	3.27 ± 0.05	0.14 ± 0.01	< 1	—	—	—
20	EXAFS 1xLa	6.2 ± 2	3.25 ± 0.05	0.43 ± 0.07	—	—	—	1.4
24	Diffraction	9.7 ± 0.9	3.22 ± 0.05	0.15 ± 0.01	< 1	—	—	—
24	EXAFS 2xLa	8.8 / 0.4 ± 3	3.28 ± 0.05 / 3.70 ± 0.1	0.53 ± 0.1 / 0.3 ± 0.2	—	—	—	1.7
24	EXAFS 1xLa + 1xGa	9.2 ± 3	3.28 ± 0.05	0.53 ± 0.07	$0.2^{+2}_{-0.2}$	2.6 ± 0.2	$0.2^{+0.6}_{-0.2}$	0.9
28	Diffraction	9.6 ± 0.9	3.25 ± 0.05	0.16 ± 0.01	< 1	—	—	—
28	EXAFS 2xLa	6.4 / 0.8 ± 3	3.26 ± 0.05 / 3.73 ± 0.1	0.46 ± 0.07 / 0.4 ± 0.2	—	—	—	1.8
28	EXAFS 1xLa + 1xGa	5.6 ± 3	3.25 ± 0.05	0.43 ± 0.07	$0.2^{+4}_{-0.2}$	2.7 ± 0.2	$0.2^{+0.6}_{-0.2}$	1.4

can be drawn from the spectrum for this composition is that the structure of the glass changes in going from x=24 to x=28 as well as from x=20 to x=24. The nature of the change between the former two compositions cannot be assessed on the basis of the current analysis.

4.4 COMPARISON WITH X-RAY DIFFRACTION RESULTS

The results discussed in the previous section have been translated into a form suitable for comparison with the X-ray diffraction results displayed in table 1.1. All the appropriate quantities are listed in table 4.3 for direct comparison. The most striking difference seen between the EXAFS and diffraction results is in the width the two techniques give for the distribution of La atoms around Ga atoms. The primary cause of this discrepancy is an error in the analysis of the diffraction experiment, and the source of this error is discussed briefly in the following paragraph.

Since no diffraction experiment can be performed to infinite momentum transfer, experimental RDF's (as discussed in chapter 1) will always be comprised of the true RDF convolved with an effective resolution function which is the Fourier transform of the truncation function applied to the experimentally obtained reduced interference function. In obtaining the results quoted in reference 1.3 the effects of this convolution were accounted for by simply subtracting the width of the peak in the Fourier transform of the truncation function from the width of the peak in the measured RDF. While the width of the convolution of two positive definite functions (such as a Gaussian resolution function with a Lorentzian line shape) may be reasonably well approximated by the sum of the widths of the two

functions, such a sum is a very poor approximation to the result of the convolution of two functions which are not both positive definite. Since the RDF shown in figure 1.2 is obviously not positive definite the above mentioned treatment of the effects of truncation in the diffraction experiment causes the quoted results to underestimate the true width of the distribution by about 0.25 A, which is the width of the resolution function. When this error is accounted for, the disagreement between the two experiments on the width of the distribution is greatly reduced.

The EXAFS and X-ray diffraction results are also seen to disagree considerably on the number of La neighbours the Ga atoms have at the composition x=28. It has already been suggested that the models used for analyzing the EXAFS spectrum are inadequate at this composition, however this is based on very indirect reasoning at best. Perhaps a more conclusive argument for the inadequacy of the models used is the fact that the disagreement between the EXAFS result and the diffraction result is less in the case where the La shell is modeled with greater flexibility. For both x=20 and x=24 the value for N based on the EXAFS measurement is less than that given by diffraction, although in both cases the discrepancy is within the interval of uncertainty in the EXAFS measurement. For these latter two compositions the difference is more likely due to a systematic error in E_o or in a reference function (such as $|f(k,\pi)|$ or S_o^2), rather than to a deficiency in the model.

A more detailed examination of table 4.3 indicates that the trend seen for R_{La} in the diffraction experiment is not present in the EXAFS results. For both experiments the amount of variation seen is within

the interval of uncertainty so perhaps a great deal of attention need not be paid to this observation. However, if the original values of the parameters are considered (see table 4.2 for example), it is seen that the R_o parameter in the fit is significantly less for the x=24 composition than for either of the other two. Therefore this may reflect the same feature which led to the reduced value for R at this composition as found in the diffraction experiment. The disagreement between the value given for the position of the peak in the La distribution would then be yet another indication of the limitations of the traditional method of analysis used in this chapter.

4.5 CONCLUSIONS

From the discussion of the previous two sections it is apparent that EXAFS measurements can provide a description of the majority contribution to the local environment of a specific atom in a metallic glass. However it is also clear that the EXAFS technique can also fail in certain cases, and it appears most likely that the greatest problem may be found in systems which contain distributions that are not well described by the model used for the analysis of the spectrum.

Moreover the correlation between the width and size of the distributions used in the analysis is sufficiently strong as to make accurate measurement of the CSRO parameter extremely difficult, if not impossible, in cases where the contributions of the various constituents cannot be isolated in the Fourier filtering stage of the analysis.

This study should not be taken as mere floccinaucinihipilification of the EXAFS technique however. It has been shown that EXAFS

spectra are indeed sensitive to changes in the local structure at specific sites in materials. The precise interpretation of these changes, however, will require extremely accurate measurements of the absorption coefficient (with a noise level of at most 0.03%) and the developement of more sophisticated methods of analysis. Preliminary studies of one such possible alternative method are presented in the final chapter of this thesis.

5 FREDHOLM INVERSION OF EXAFS DATA

5.1 MATHEMATICAL BACKGROUND

As was seen in chapter 2, the experimentally observed EXAFS function, $\chi(k)$, due to a single shell of neighbouring atoms, may be interpreted through the equation:

$$\chi(k) = -\frac{4\pi}{k}\left|f_i(k,\pi)\right|S_o^2(k)\int_o^\infty \rho(R)\,\sin\left[2kR + \alpha_i(k)\right]\,dR \tag{5.1}$$

Here the effects of resolution and other shells have been ignored. Given that the particular shell of interest is generally only non-negligible on a finite interval, the above may be effectively rewritten as:

$$\chi(k) = -\frac{4\pi}{k}\left|f_i(k,\pi)\right|S_o^2(k)\int_{R_1}^{R_2} \rho(R)\,\sin\left[2kR + \alpha_i(k)\right]\,dR \tag{5.2}$$

Traditionally, as described in chapter 2, the above expression has been used to obtain physical parameters by assuming some analytical form for $\rho(R)$ and computing the integral in (5.1) in closed form. The result is a model expression for $\chi(k)$ which depends on some finite set of parameters used in defining the $\rho(R)$. However, as indicated in chapter 4, it would be desirable to have an alternative method of analysis which would be essentially non-parametric.

Just such an alternative approach to analyzing EXAFS data has been proposed by Babanov et al.[5.1]. This latter method proceeds by noting that (5.2) is a Fredholm integral equation of the first kind for $\rho(R)$, which can be solved numerically. However, it must be noted

from the outset that this is by no means a trivial procedure. Indeed, integral equations of the first kind are one of the classic examples of an ill-posed problem. An explanation for this may be seen quite easily by considering Riemann's lemma which essentially states:

For any integrable function f:

$$\lim_{\lambda \to \infty} \int_0^1 f(R) \sin \lambda R \, dR = 0 \tag{5.3}$$

From this it is seen that any solution of (5.2) may have a very large, highly oscillatory function added to it which would only slightly perturb the right hand side of the equation. Conversely, it is clear that any small change in the left hand side (which for the purposes of this discussion will be determined from experiments of finite accuracy) could lead to large changes in the result obtained from any exact solution to (5.2). This is precisely what is meant by the phrase "ill-posed."

The fact that (5.2) cannot be solved exactly, however, does not imply that an accurate estimate of the solution ($\rho(R)$) cannot be obtained from a given set of data ($\chi(k)$). In fact a number of algorithms for obtaining approximate solutions to such equations exist, and in ideal cases these approximate solutions can approach the true solution with arbitrary accuracy[5.2].

Equations such as (5.2) are seen in many areas of the physical sciences, and a certain amount of terminology has been built up around such problems. The problem of determining $\chi(k)$, from a given $\rho(R)$, is called the "direct problem." The more difficult problem, finding $\rho(R)$ from a given $\chi(k)$, is called the "inverse problem." The process

by which $\rho(R)$ is obtained from $\chi(k)$ is referred to as "inversion."

Babanov et al. obtain an approximate solution to (5.2) through the regularization method of Tikhonov[5.3]. In this chapter a slightly different approach will be presented which borrows heavily from the geophysical literature of "Inverse Theory"[5.4]. Both methods involve minimizing some functional corresponding to the distance between the two sides of (5.2) in some norm (typically the L_2 norm). In both cases some mechanism must be provided for damping out the high frequency components of any potential solution. In Tikhonov's method this is done by adding a penalty functional to the functional being minimized, such that the penalty functional is large for highly oscillatory functions. Thus, for example, the object may be to minimize an expression such as the following:

$$|K f - x|_2 + \alpha |L f|_2 \tag{5.4}$$

Here K stands for the integral operator with the EXAFS kernel, α is called the regularization parameter, and L is some linear operator such as the identity or gradient operator. The value of the parameter α should be selected according to some knowledge the experimenter has about the inaccuracy of the left hand side of the integral equation. However, when similar methods are used in the inversion of Mossbauer data, the choice of α is often left up to more subjective criteria such as whether the $\rho(R)$ obtained (which in this case would be a distribution of hyperfine fields) looks "reasonable."[5.5]

The method which will be discussed in detail throughout the remainder of this chapter will be called "Singular Value Decomposi-

tion" (or SVD) inversion, for reasons which will become clear in due course. In this method the problems foretold by Riemann's lemma are controlled by expanding the function $\rho(R)$ in terms of a basis of eigenfunctions on some discrete R axis, and setting the coefficients of the more oscillatory functions in this expansion to zero. As was the case with α, the choice of which coefficients to set to zero can be obtained either from the known level of noise in the original data, or semi-arbitrarily on the basis of certain features of the solutions obtained.

The first step in any inversion procedure is to obtain a discrete algebraic equation which is equivalent to the analytic equation (5.2). This is done by first quantizing the R and k axes, and then approximating the integral on each of the subintervals (R_i, R_{i+1}) with some numerical quadrature formula. It is possible to use a relatively high order quadrature formula if interpolation is used to provide values for the integrand at points inside the subintervals [5.6]. However it is generally more advantageous to use a simple formula, such as the trapezoidal rule, and increase the fineness of the grid on the R axis if greater accuracy is required. The end result of this process is an algebraic equation, which will be very over-determined in all cases of practical interest. Such a system might appear as:

$$\sum_j K_{ij}\, \rho_j = \chi_i \tag{5.5}$$

Since this system is over-determined, however, it cannot in general be solved simply by computing K_{ij}^{-1} and using this operator on both sides of the above equation, as K_{ij} may not have an inverse.

Indeed, even if K_{ij}^{-1} did exist the fact that the underlying problem (i.e. equation (5.2)) is ill-posed will cause K_{ij} to be extremely poorly conditioned, and consequently its inverse could not be computed accurately. Even in the case where K_{ij}^{-1} does not exist, however, it is still possible to solve (5.5) for ρ_j in a least squares sense, and furthermore to do so in such a way that the components of the problem which are causing the instabilities can be identified.

It can be proven that any real matrix, K, of rank k, may be expressed as a product of three matrices as follows[5.7]:

$$K = U\ R\ V^T \tag{5.6}$$

where, if K is an m x n matrix, U and V are orthogonal matrices (m x m and n x n respectively) and R is a diagonal matrix of rank k. Furthermore, algorithms exist for the computation of such an expansion and the diagonal elements of R are uniquely defined, non-negative real numbers, which can be arranged in non-increasing order. This expression for K is called its Singular Value Decompostion, the diagonal elements of R are called its Singular Values and the columns of V are called its singular vectors. Since the inversion of an orthogonal matrix is manifestly stable, the problems encountered when inverting K must arise solely from the poor conditioning of the diagonal matrix R.

At this stage, therefore, the original problem has been converted to the approximately equivalent* problem:

$$\text{(5.7)} \qquad \text{minimize} \quad |R\,y - g|_2 \quad ; \quad \text{where} \quad y = V^T \quad \text{and} \quad g = U^T x.$$

Note at this point that if (5.7) is used in conjunction with (5.6) the minimization problem may involve as many as 50 or more variable parameters (the number of points on which $\rho(R)$ is to be defined). However in this case the minimization is linear and consequently the problem is far easier than the minimizations performed in chapter 4, even though the number of parameters is considerably larger. In the following discussion the compact notation $R\,y \cong g$ will be used to represent the minimization of the L_2 norm of the difference between $R\,y$ and g. From (5.7) it is seen that the solution desired, ρ, may be easily obtained from the solution to the more straightforward problem, $R\,y \cong g$. Since V is orthogonal, its columns span the vector space in which the solution vector is defined. Therefore, (5.7) can be thought of as an equation determining the coefficients for the expansion of the solution of (5.5) in terms of this basis. The stability needed for inversion of the original integral equation of interest will come from setting some of the coefficients in this expansion to zero. To see how this selection is to be made, consider the expanded version of equation (5.7) given on the following page.

---

* By this is meant equivalent to the extent allowed by the procedures of quantization and numerical quadrature.

$$
(5.8) \qquad \begin{bmatrix} R_1 & & & \\ & R_2 & & \\ & & \ddots & \\ & & & R_n \end{bmatrix} \begin{bmatrix} y_1 \\ y_2 \\ \vdots \\ y_n \end{bmatrix} \equiv \begin{bmatrix} g_1 \\ g_2 \\ \vdots \\ g_n \\ g_{n+1} \\ \vdots \\ g_m \end{bmatrix}
$$

Three things should be noted about this equation:

1). If R has rank $k < n$, then elements $y_{k+1} \ldots y_n$ are completely undetermined

2). The L_2 norm difference between the two sides of (5.8) is at least $\sum_{i=k+1}^{m} |g_i|^2$.

3). The minimum norm of this difference is obtained if the y_i are chosen according to $y_i = g_i / R_i$ for $i=1, \ldots k$.

From these three points it is clear that, if $R_{k+1}, \ldots R_n$ are zero, then the elements y_i $i=k+1, \ldots n$, will be completely undetermined, and therefore the solution will not be unique. It must be remembered however that the above calculations are being performed on a computer, starting with data of finite accuracy, so that the meaning of "zero" must be defined.

In most practical cases encountered none of the singular values will be identically zero, or even zero to within the precision of the computer being used. However, often R_1 (the largest singular value by convention) may be five or six orders of magnitude greater than R_n (the smallest), and it will be recalled that the ratio of these two

quantities defines the condition number for the diagonal matrix R. Furthermore, as indicated in the preceding discussion, it is the size of this condition number which is at the heart of the problem. Consequently, it is reasonable to question whether these smaller elements should be kept as non-zero, particularly when some minor perturbation of the problem could cause some of them to be zero anyway.

Based on the above discussion, consider what would happen if some of the smaller singular values were in fact zero, since they might well have been so under a slightly different set of circumstances. First, as noted above, any solution would then be non-unique. This, however, may not be a serious problem since the unique solution to the full rank problem is of no practical use. To get around this non-uniqueness of the solution to least squares problems it is conventional to take the minimum norm solution (i.e. that unique solution which minimizes $|y|_2$ as well as the residual norm). By examining equation (5.8) it is clear that this corresponds to setting $y_i = 0$ for all i for which $R_i = 0$. For the problem being discussed here this choice has an advantage in addition to simply providing uniqueness, for it is found empirically that the singular vectors corresponding to the smallest singular values tend to be the most oscillatory. Hence setting the undetermined y_i to zero corresponds to eliminating the most oscillatory components of the solution.

The number of singular values which are to be treated as non-zero is called the pseudo-rank of the problem (denoted k_p), and for any given problem its value depends on a such factors as the noise in the data and the precision of the computer used to perform the calculations. Therefore some procedure must be applied to select the appro-

priate pseudo-rank, since it cannot be known a priori for any given problem. As mentioned earlier one choice for the pseudo-rank (k_p) would be based on having the residual norm equal to that expected on the basis of the noise. However, even if no knowledge of the noise level is assumed a reasonable selection may still be possible. As increasingly large k_p are considered the residual norm will decrease while the norm of the solution will increase. Typically, beyond a certain point, increasing k_p will provide only a marginal decrease in the residual norm and this will be obtained only at the expense of a very large increase in the norm of the solution. Such a large norm for the solution would be indicative of the fact that some highly oscillatory components have been introduced into the solution, and therefore a smaller k_p should be considered. Reference 5.7 should be consulted for a more detailed discussion on the selection of the pseudo-rank.

Implementing these ideas for the case of simulated EXAFS spectra yields results such as that shown in figure 5.1. In this figure the solid line represents a density function which was used to construct an EXAFS spectrum on the basis of equation 5.2, using the scattering functions corresponding to Ga-Ga pairs. The dashed line represents the results of applying the inversion procedure described above. In this case k_p was taken to be 10. For this case the spectrum was simulated without noise (at least none beyond that inherent due to computational error) using a symmetrically shaped shell of La atoms around an absorbing Ga atom. The $\chi(k)$ was defined on $4 - 15\ A^{-1}$ and 70 data points within this interval were used as input to the inversion routine after first weighting the data by a factor of k^3. The

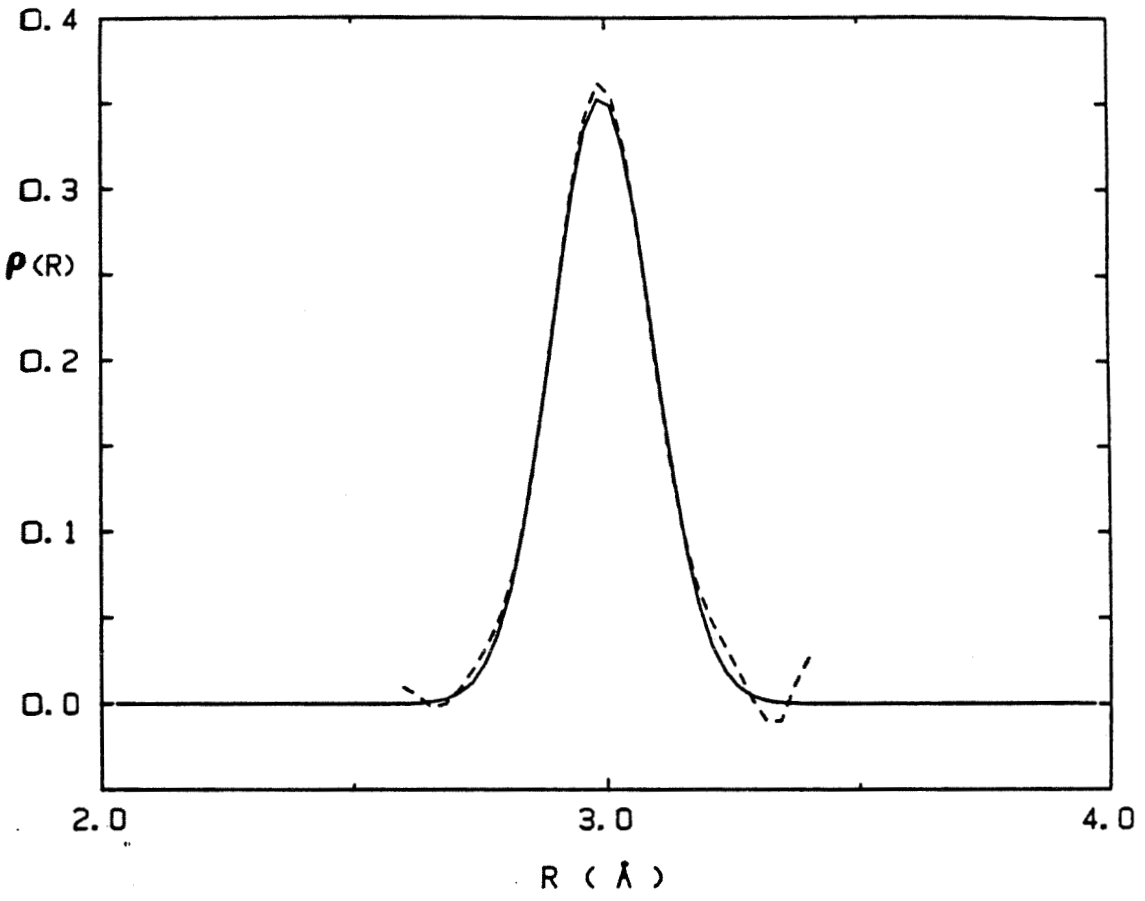

Figure 5.1 SVD inversion for a symmetric distribution. Solid line gives the distribution used in computing the simulated spectrum. Dashed line gives the SVD inversion of that spectrum.

output of the inversion was defined on 30 points between 2.9 and 4.3 A, k_p was taken to be 9, and the trapezoidal rule was used in the construction of the algebraic equation (5.5). It is clear that the method provides a reasonable description of the input distribution in this ideal case, even though no explicit constraints were imposed on the solution as was done by Babanov et al. However, careful observation of figure 5.1 reveals that the solution obtained does make some excursions into the unphysical regime of negative density. This problem is of little consequence however, particularly since the least squares minimization can be performed under the constraint that the solution be nonnegative (see chapter 23 of reference 5.7).

Although the results displayed in figure 5.1 are most gratifying, it is important to note that the traditional methods of EXAFS analysis perform adequately under such ideal circumstances as well. For this reason it is imperative that the new method also be tested under the more demanding circumstances brought about by asymmetric peak shapes, noisy, truncated data sets (truncated at both low and high k) and inexact threshold energies and scattering functions. The next section treats these problems in greater detail.

5.2 INVERSION IN NON-IDEAL CASES

A major concern for the purposes of this thesis is how the analysis method presented above will handle an asymmetric peak when the data are truncated at about 4.0 A^{-1}. Figure 5.2 demonstrates that this simple combination of features presents no serious problem, although it is seen that for this problem constraining the solution to be non-negative does help. Again no noise has been introduced in the

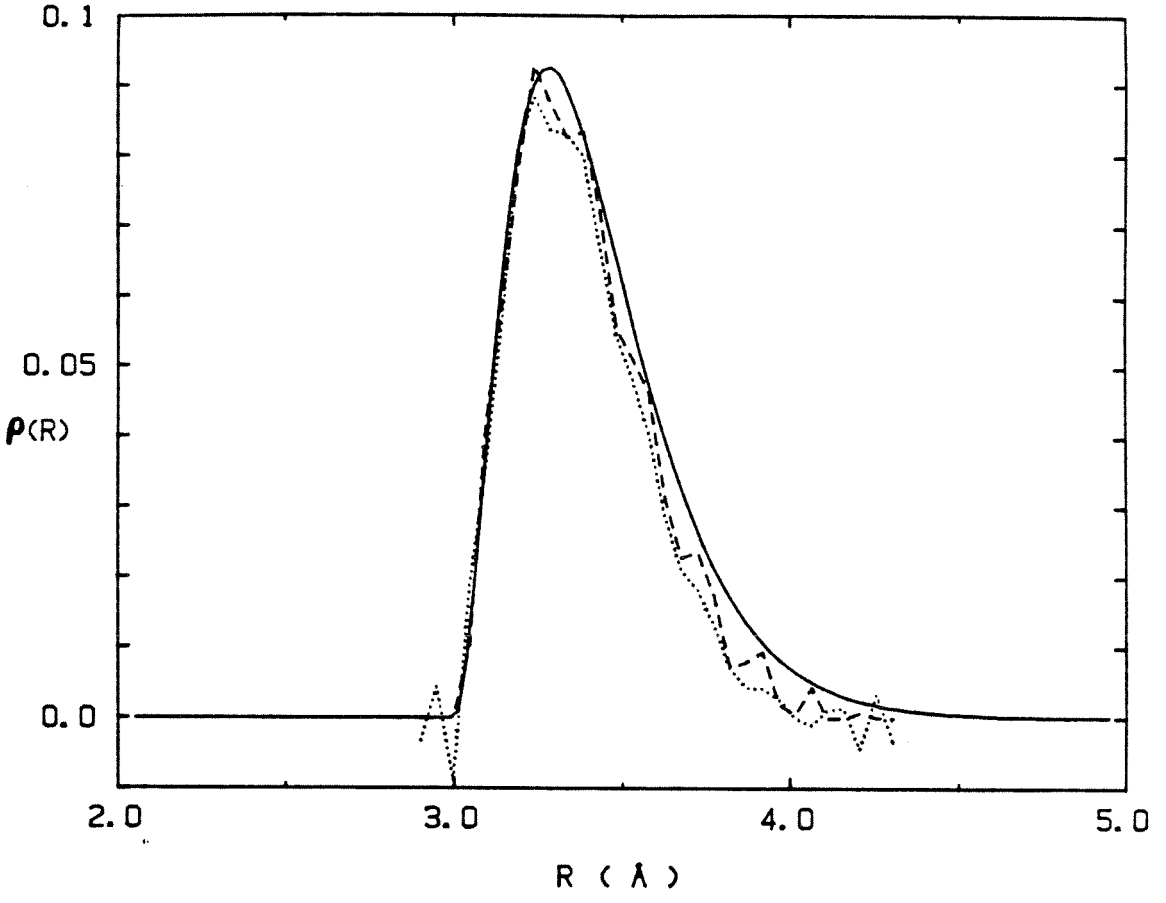

Figure 5.2 SVD inversion for an asymmetric distribution. Simulated spectrum was defined on 4.0 to 15.0 A^{-1}. Dotted line gives the inversion without constraints, the dashed line gives the inversion computed under non-negative constraints.

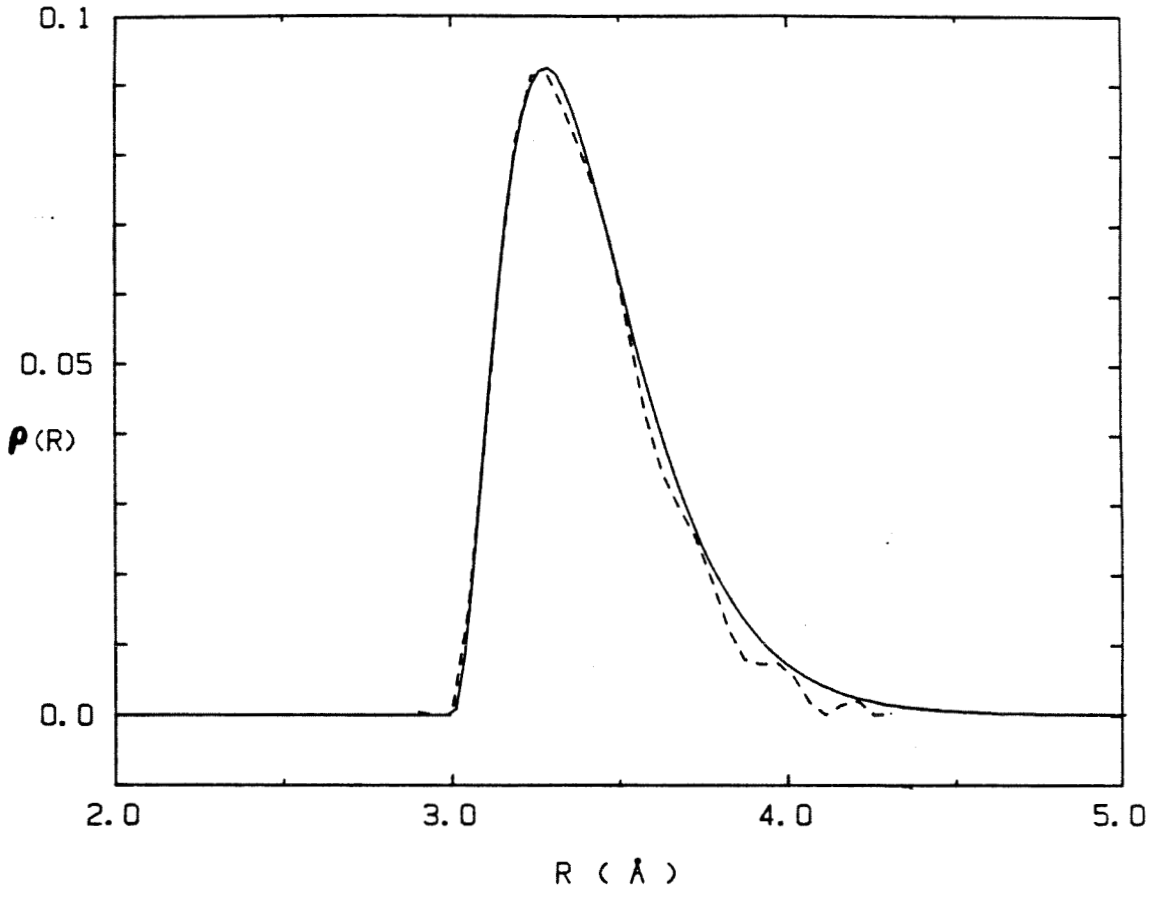

Figure 5.3 Result for constrained inversion of data defined only on the restricted interval 4.0 to 10.0 A^{-1}.

simulation used, and no filtering has been performed so the test is still not rigorous. However, as before, the result is encouraging. A key feature that should be pointed cut here is that much poorer results are obtained if the inversion is performed from a data set containing only 50 points, rather than the 70 used to produce figure 5.2a. On the other hand, no significant improvement was obtained as a result of expanding the problem so that 150 data points were used to determine the density function on 50 points along the same interval of the R-axis. Thus a fairly large data set is needed, but beyond a certain point nothing is gained by going to larger systems. Naturally the amount of computer time required for larger systems increases rapidly with the size of the linear system.

When the constraint of non-negativity is imposed the question of the selection of the pseudo-rank of the problem is solved in a straightforward manner. When too small a k_p is selected it is found empirically that the resulting constrained least squares system has inconsistent constraints. Generally it was found that a value of k_p which was one or two larger than this cut-off value produced the best results when compared with the density function use in simulating the spectrum. For the above test a pseudo-rank of $k_p = 22$ was used for the constrained solution while $k_p = 19$ was used for the unconstrained solution. All the results reported below were based on simulations on a smaller interval of k-space than that used above and in these cases a value of $k_p = 15$ or 16 was found to be appropriate. Again the interested reader is referred to reference 5.7 for a more detailed exposition on the selection of the pseudo-rank.

Figure 5.3 demonstrates that limiting the available data set at

large momentum transfer also has little effect on the results obtained. In fact the inversion obtained from a more restrictive k-space interval is superior to that shown in figure 5.2a, due to errors encountered in the numerical quadrature at the higher values of k. This test, as well as all those discussed below deal with constrained solutions.

The model distribution used in figures 5.2 and 5.3 is simply a single shell of the type used in chapter 4. However, as discussed in chapter 4, one of the short-comings of the more traditional methods of analysis is that the experimenter may be left wondering if the failure of a given model to describe the data is due to a failure of the physical model in general, or simply its inability to follow subtle changes in the peak shape. Thus a real test of the possible usefulness of the new method would be whether or not it is able to pick out such subtle differences between two possible peaks. To assess this aspect of the problem three different model distributions were considered, as shown in figure 5.4a. The SVD inversions of the corresponding EXAFS spectra are show in figure 5.4b. It is seen immediately that the trends present among the three models are also present in the inversions, although the detailed reproduction of the more complicated peaks is not as true as that for the unperturbed peak (solid line in the figure). The same pseudo-rank ($k_p = 15$) was used for all three cases.

All tests up to this point have been conducted using simulated EXAFS spectra to which no noise has been added. To assess the effects that noise in the data can have on the procedure, some inversion tests were performed on noisy simulations and the results of some of these

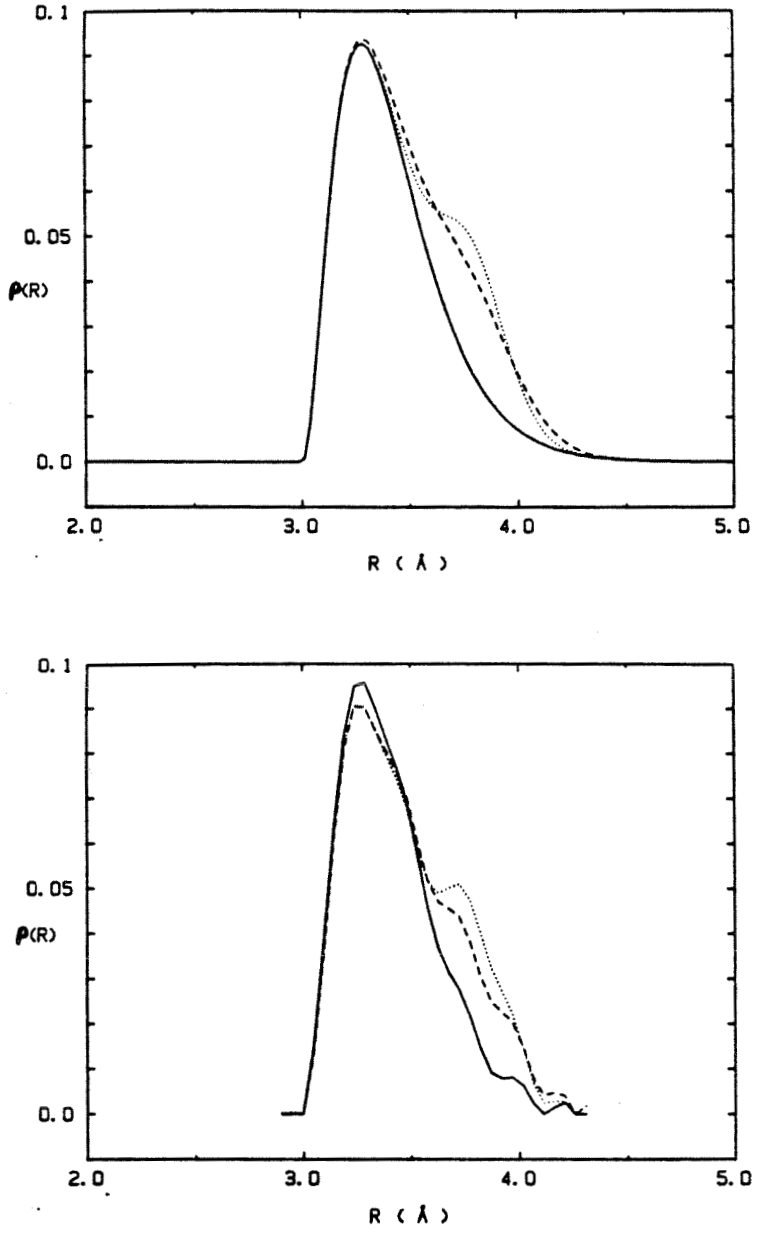

Figure 5.4 Test of the sensitivity of the method to changes in the distribution shape. a). The three different distributions used. b). Results for inversion of data constructed from the three distributions shown in a). Line types in the two figures correspond.

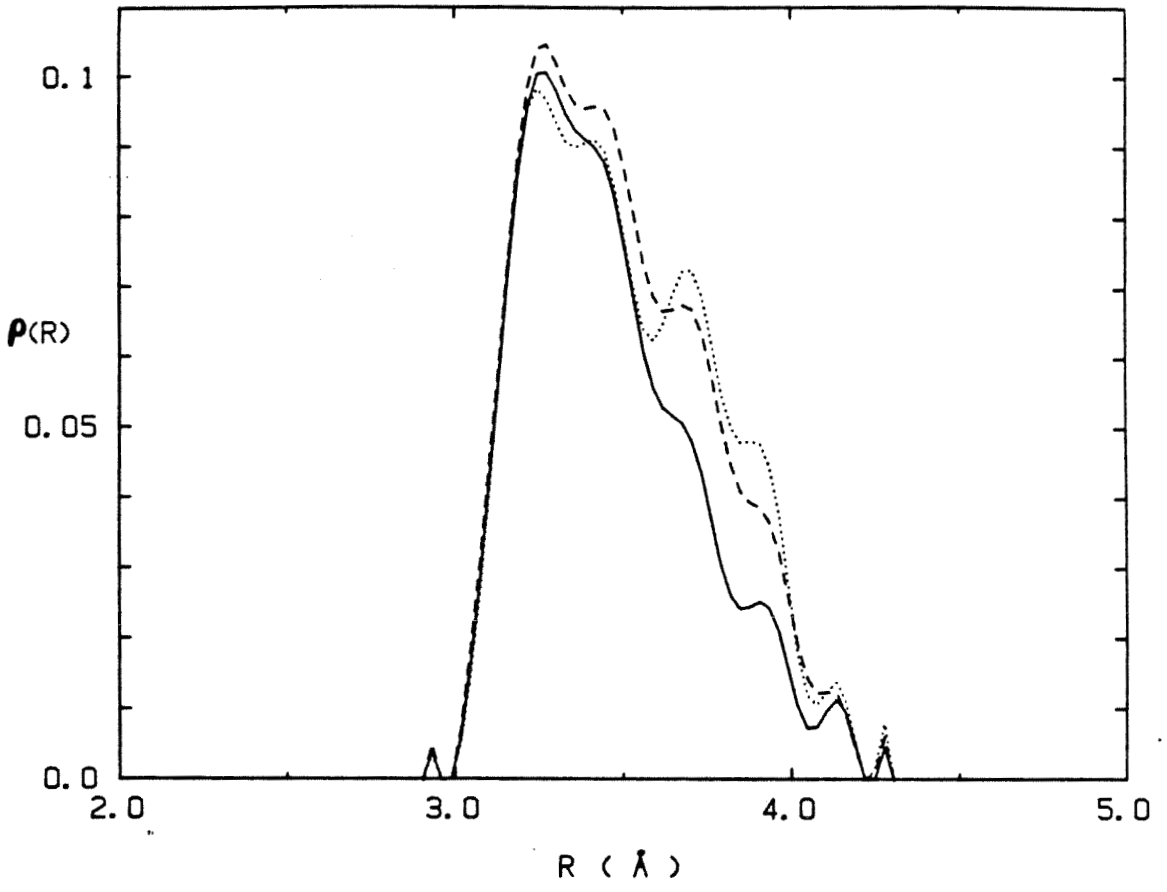

Figure 5.5 Inversion results corresponding to the distributions of figure 5.4a). with .03% noise added to the simulated spectrum before the computation of the inversion.

tests are displayed in figure 5.5. The noise level was simulated by adding a Gaussian random variable to the spectrum used for figure 5.3, its magnitude corresponding to a 0.03% noise level in an EXAFS measurement (or 1/3 the noise level seen earlier in the Ga_{24} experiment of chapter 4). To further reduce the effects of this noise the simulated spectrum was passed through a band pass filter, just as described in chapter 4, although in this case a much wider band pass was used (0 to 5 A with no taper). Due to the effects of the noise the results of the inversion exhibit sharp features which were not present in the input distributions, however, as in figure 5.4b the correct trend from one distribution to the next is reproduced even in the presence of noise. Thus a certain level of noise can be present in the data without destroying the viability of the method. Tests conducted with noise levels closer to those present in the data considered in chapter 4, however, gave much poorer results. Therefore it appears that the method discussed, as presented here, cannot be used on those data.

As noted above, the filter used in creating the inversion shown in figure 5.5 was much wider than that used on the experimental data presented in chapter 4. This is because it was found that the inversion method encountered serious difficulties when a more restrictive band pass window was used. As an example of this, figure 5.6b was created from the same data as figure 5.5, except for this case the window used to define the band pass filter had a 20% taper on each end of its range. The result of this is a significant distortion of the side lobe structure of the main peak in the transform, and a consequent minor distortion of the EXAFS spectrum, as shown in figure 5.6a.

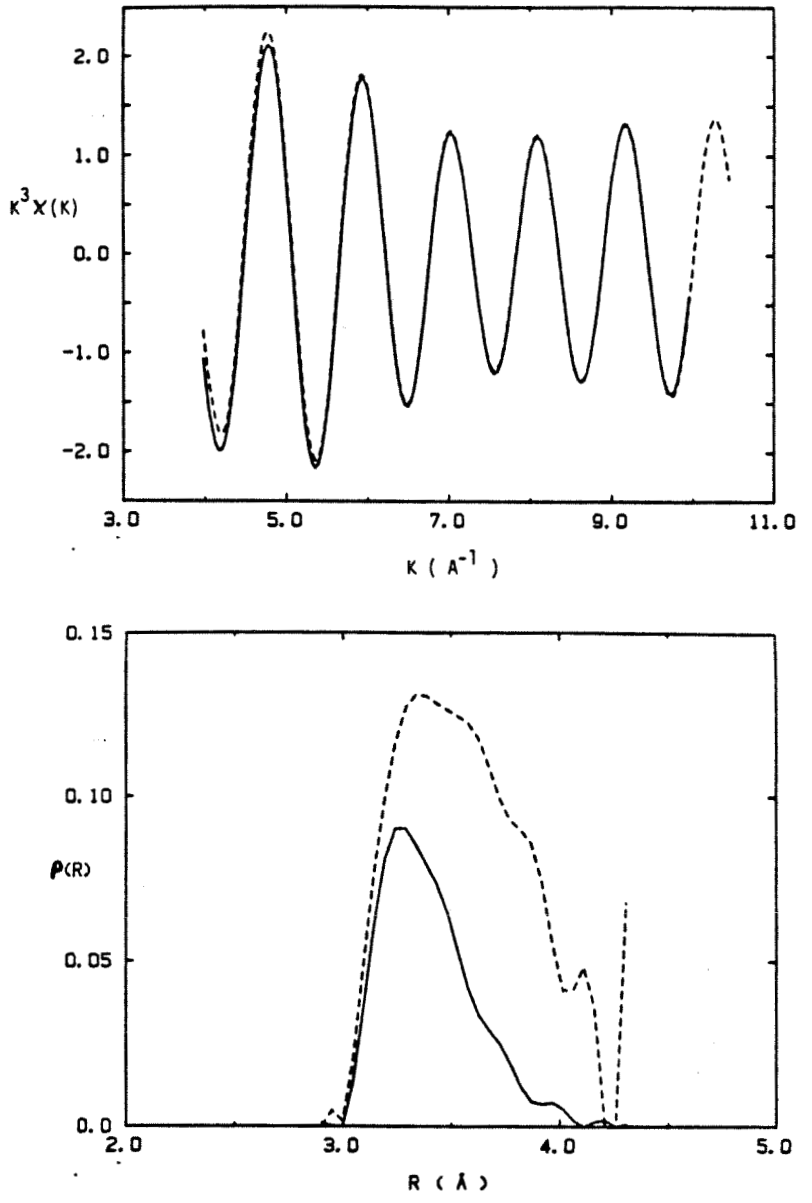

Figure 5.6 Effects of a restrictive band pass filter (0.0 to 6.0 A^{-1} with 20% taper on each end) on:
a). The simulated spectrum (dashed line shows the filtered spectrum), and b). The resultant inversions (Solid line gives the inversion of the unfiltered spectrum).

However figure 5.6b shows that this very minor distortion of the input data can lead to very significant differences in the results of the inversion, and once again emphasizes the inherent instability of the integral equation. Similar problems were encountered when the threshold energy was chosen incorrectly (by 2 eV say), although in this case the result actually improved if non-negative constraints were removed from the solution. This indicates that some fraction of the problems encountered here may be due to a deficiency in the algorithm used to implement the non-negative constraints. Indeed the algorithm used has been only quite recently developed and there is reason to believe that it is inadequate for many applications[5.8].

As described in this section, therefore, SVD inversion will not be able to fulfill the task originally envisioned. That is, it will not be possible to use it in order to invert a spectrum which corresponds to a single shell in the Fourier transform of a measured spectrum, after this contribution has been isolated by a narrow band pass filter. This is due to the distortions introduced into the scattering functions $\alpha(k)$ and $|f(k,\pi)|$ by the filter. To fully appreciate this fact, it must be realized that the distortion introduced by the filter depends not only on the parameters of the window (such as its position and shape), but also on the specific shape of the peak in the density function. This is illustrated in figure 5.7, where the inversions presented are based on data filtered with a rather narrow band pass (1.5 to 4.0 A^{-1}). The scattering functions used were determined from an identically filtered spectrum, which had been constructed assuming a peak shape given by the solid curve of figure 5.4. In other words the amplitude and phase functions of the simulated, filtered spectrum

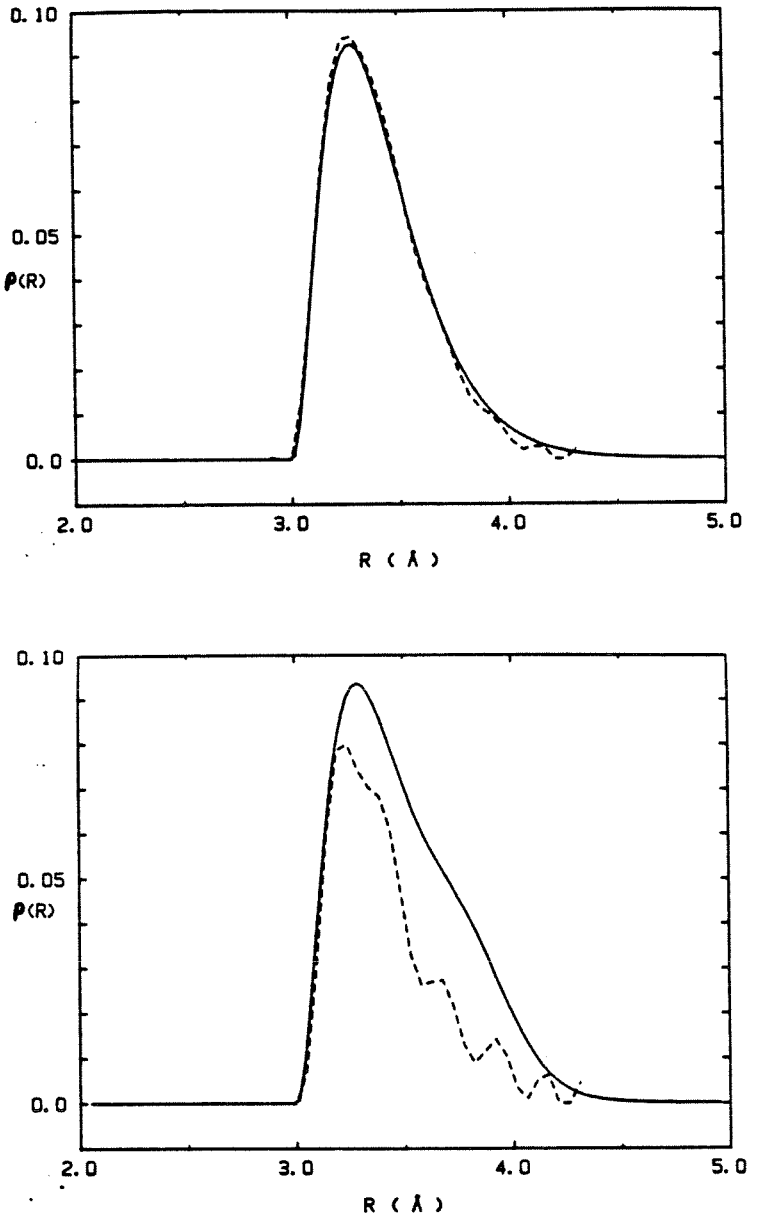

Figure 5.7 a). Inversion of a filtered spectrum for a simple distribution when distorted scattering functions are used. b). Inversion of the filtered spectrum corresponding to a more complex distribution when the same scattering functions are used.

were extracted in the same manner as was used in chapter 4 to determine $S_o^2(k)$ for Ga_2La. Naturally, under these conditions the inversion is able to extract the density function for the same spectrum which was used to determine the scattering functions, since the distortions introduced by the filter are precisely accounted for. However, if the same scattering functions are used to invert a spectrum which corresponds to a slightly distorted density distribution the result is unacceptable, as seen in figure 5.7b. Therefore the problems demonstrated in figure 6 cannot be rectified merely by using distorted scattering functions computed from a simulated spectrum, since the distribution used will undoubtedly differ somewhat from the distribution in the material under study.

5.3 HOPE FOR THE FUTURE

Although the discussion of the last section indicates that the simple application of SVD inversion described here will not be adequate for inversion of real EXAFS data, the method should not be dismissed out of hand. In particular it has been noted that the failure mode of the method is most often to give a distribution which has far too large a coordination number, and/or has very sharp kinks. It may be possible to control these problems if additional constraints are put on the solution, as has been done by Babanov for regularization inversion. The early results presented at the start of section 5.2 are encouraging enough that the investigation of possible refinements such as those mentioned could prove most beneficial. In addition the use of a more robust algorithm for the implementation of the non-negative constraints could provide a considerable improvement over the performance seen here.

APPENDIX: SOFTWARE DESCRIPTION

During the course of the research described in this thesis a rather extensive amount of computer software was developed for the analysis of EXAFS data. This software is designed to run on a PDP-11/23 computer under the RT-11 operating system, and it assumes that a VT105 graphics terminal is available. The individual programs in this package are reasonably well documented. However an overview of how these programs relate to each other, as well as some background on the reasons for selecting various algorithms, should be useful for future users. The purpose of this appendix is to provide such an overview.

I DATA STRUCTURES

The RS232 interface of the PDP-11/23 is most easily accessible through the MINC BASIC operating system. For this reason a BASIC program called MICROT or MICROC (depending on whether the data were recorded in constant time or constant counts mode) is used to transfer data from the EXAFS spectrometer controller to the host computer. Each of these two programs create two ASCII files which consist of a sequence of numbers, one ASCII floating point number per record. In the following discussion such files will be referred to as "transfer files."

The EXAFS controller works with numbers in a BCD representation, however MINC BASIC only accepts data transfers in ASCII form, and furthermore it ignores the parity bit of the ASCII byte. To bypass

this problem, the controller breaks each number to be sent to the computer into a base 100 representation, and sends a 7 bit binary number for every numeral in this representation. In other words, "2698642." would be sent as 2_2-69_2-86_2-42_2. Each numeral sent will be interpreted by the MINC BASIC routine "CIN" as a legal ASCII character (since it will lie between 0 and 128). The routine "ASC" may then be used to convert this character into the numerical value of its ASCII code, and this may then be used to reconstruct the original number. The end result of all of this rather involved conversion is that the MINC has a binary version of a number which started off in a BCD representation in the controller. The complexity of this procedure is necessitated by the fact that MINC BASIC ignores the most significant bit of the transfer byte, and the fact that the controller was designed before this limitation of the MINC transfer system was known.

A large number of intermediate data files are generally created during the analysis of a typical EXAFS spectrum. In order to save space on the floppy disks used for mass storage, all of these files are stored in binary form rather than as ASCII files. The only exceptions to this rule are the "transfer files" created by the two MINC BASIC programs to store the raw data. All other files are created as "unformatted" FORTRAN files with a specified record length of 6 words. The first record contains two integers and two real numbers, as follows:

NDAT NVECT XORIGN XSTP

All subsequent records will have 1, 2, or 3 real numbers, the specific number present in a given file being specified by the number NVECT in

the first record. NDAT specifies the number of records following the first, corresponding to the number of data points represented.

For most circumstances data used by this software can be defined on a uniformly spaced axis for the independent variable. In such cases, the NDAT values for this independent variable are given by:

(A.1) $$X(I) = XORIGN + (I-1) * XSTP \qquad I=1,NDAT$$

In such a case the records 2 through NDAT+1 in the file will give the dependent variable values for up to three sets of data (i.e. up to three functions of the independent variable). For example, in some files X will be a distance axis in real space and the records after the first will define the real and imaginary parts, and the magnitude of a Fourier transform defined on that axis.

In cases where the independent variable cannot be expressed on a uniformly spaced grid, XSTP in the first record will be set to zero. In this case each subsequent record will have at least two real numbers, the first being the value of the independent variable at some point, and the other one or two giving the corresponding values of the dependent variables. Naturally in this case a maximum of two dependent variables may be given in the file, and the value of XORIGN is arbitrary, allowing it to be used to pass some additional information to the program using the data file.

Two programs were written to allow the user to "see" what is inside one of these binary data files, since they cannot be written out directly. These programs, PLTFIL and FIGFIL, allow the user to

obtain a listing of the numbers in the file either on the terminal or a printer. They also allow any of the dependent variables to be plotted as a function of the independent variable, either on the terminal or on an HP9872B four colour plotter. The contents of different files may also be plotted on the same graph using these programs. PLTFIL is designed to provide "quick and dirty" plots of data, whereas FIGFIL is designed to be more flexible, allowing the production of graphs of suitable quality for publication. Most of the figures in this thesis were produced using FIGFIL.

Two other programs have also been included in the package for working with these data files. These are ASC2BN and BN2ASC, which convert to and from ASCII representations of the data contained in the files as described above. These programs are needed for transfering data to other computers, such as a VAX, where different word sizes etc. would make it impossible to access the binary version of the files directly.

II PRELIMINARY DATA PROCESSING

Preliminary data analysis consists of all processing between the transfer of the data to the computer (as described above) and those programs used to determine the values of physical parameters. Five major programs are used in performing these operations.

L2CALB

This program provides a calibration of the spectrometer in the manner described in chapter 3. The lines used in the calibration are

selected interactively with the user specifying the channel number to be used, guided by a graph of the spectrum with a linear or logarithmic vertical axis. The calibration is specified by giving the change in the Bragg angle associated with a single step of the stepping motor, and an offset (the number of steps between a Bragg angle of zero and a reading of .000000 on the spectrometer controller).

SEPAVG

This program accepts as input either a standard binary data file, or ASCII "transfer" files. Its purpose is to either separate two different experiments from a given transfer file, or to add several experiments together as a form of signal averaging. The program accounts for the mode of data collection (constant counts or constant time), as well as any variation in the number of steps taken per channel during the data collection. The output from this program consists of a standard binary data file, whose independent variable gives the number of motor steps taken from the starting point to each subsequent channel, and whose dependent variables are the number of incident and transmitted beam counts. If any dead time correction is needed for the transmitted beam channel, then it is applied in this program.

MUISL

The purpose of this program is to convert the independent variable from "number of steps" to photon energy, and to isolate the resonant part of the absorption coefficient (i.e. to perform the pre-

edge background removal). In addition it allows for the removal of "glitches", in the rare case when such action is necessary. The energy scale may be constructed purely on the basis of the step size and offset found by using L2CALB on a separate measurement of the source output, but more often a slight variation of this procedure is used. The energy range covered in the measurement of a typical edge will generally contain one or two characteristic lines in the spectrum of the tube. This is insufficient to provide a reasonable calibration using L2CALB, however it will certainly be enough to establish a "fixed point" on the energy axis corresponding to the known position of one of these lines. The step size obtained from an earlier application of L2CALB on a wider energy interval may then be combined with this fixed point to provide a very satisfactory calibration, whose reproducibility will be even better than the intrinsic reproducibility provided by the spectrometer itself.

CHICLC

This program takes the isolated absorption edge provided by MUISL and calculates the EXAFS function χ according to the discussion of chapter 2. All routines dealing with splines were taken from the book " A PRACTICAL GUIDE TO SPLINES" written by Carl de Boer[2.17]. In addition this program provides a preliminary guess for the threshold energy E_0, by finding the major inflection point of the measured edge transition. The output file created defines the EXAFS function χ on a non-uniform energy axis.

CHIANX

This program converts the independent variable to photo-electron wave vector from photon energy, and performs the Fourier band-pass filtering needed to isolate the contribution of various atomic shells. The initial guess for E_o computed by CHICLC is passed to this program in the variable XORIGN, and the user may accept this value or specify another. Alternatively the input may be given directly in terms of a uniformly spaced wave vector axis. This is useful when dealing with files created by the simulation programs which will be discussed below. The type of input used in any given case can be flagged by the variable XSTP, since the output from CHICLC is always non-uniform, where as all files created with respect to a wave vector axis are uniformly spaced.

After computing the wave vector value appropriate for each data point the program uses Lagrange interpolation to construct a uniformly spaced "k" axis. The data can then be weighted and windowed in the manner described in chapter 4 (using either k^m weighting, or weighting with respect to a known set of scattering functions). The Fourier transform is computed using a pruned FFT routine with the data padded to a total of up to 4096 points. Windows of various shapes may be applied to both the input to the transform and to the transform itself, thus providing the flexibility needed in assessing the effects of such procedures. The output is a band pass filtered spectrum, and optionally, the amplitude and phase functions associated with a specified shell of neighbours (see reference 2.21).

EXPCRT

This program takes the amplitude and phase function output of CHIANX and derives the specific functions $|f(k,\pi)|$ and $\alpha(k)$ based on user supplied values for the known parameters N, σ, R, and FWHM (the experimental resolution), for either a Gaussian or a Crozier-Seary peak shape.

III CURVE FITTING

The nonlinear least squares curve fitting program used in this thesis is base on the variable metric function minimization algorithm of Fletcher and Powell[4.5]. Although this algorithm is not specifically tailored for least squares minimization (as are some other algorithms), its flexibility was useful in addressing some of the problems encountered in fitting to EXAFS spectra.

This algorithm, like all multi-dimensional optimization algorithms, works by choosing a certain direction in parameter space and then minimizing along this direction. Another direction is subsequently chosen and minimization along this direction is performed, etc. In the Fletcher-Powell algorithm the search direction is taken as:

$$\underset{\sim}{d}^{(i)} = - H^{(i)} \underset{\sim}{g}^{(i-1)} \tag{A.2}$$

where $g^{(i-1)}$ is the gradient at the point that the one-dimensional search along $d^{(i)}$ starts. Although intuition might suggest that the

best direction to search would be along the path of steepest descent (corresponding to taking $H^{(i)}$ in the above to be the identity matrix), this is often not the case, particularly when the equipotentials of the function being minimized are extremely oblate (as is the case for EXAFS curve fitting). The Fletcher-Powell algorithm constructs a sequence of positive definite "metrics" $H^{(i)}$ which converge toward the inverse of the Hessian of the function being minimized (assuming that the function is reasonably well approximated by a quadratic form in the neighbourhood of the minimum). It is useful to note that if the function being minimized is in fact a quadratic function of the parameters, and $H^{(i)}$ is the inverse Hessian, then a one-dimensional minimization along the direction given by (A.2) will exactly minimize the functional.

$$f = \frac{1}{2} \sum_{i,j} G_{ij}\, x_j x_i + b\, x + c \tag{A.3}$$

$$\partial_i f = \sum_j G_{ij}\, x_j + b_i \tag{A.4}$$

Obviously from this, it is seen that the condition $\nabla f = 0$ is satisfied for that x determined by the equation:

$$\underset{\sim}{x} = -G^{-1}\, \underset{\sim}{b} \tag{A.5}$$

where $\underset{\sim}{b}$ is the gradient of the functional at $\underset{\sim}{x} = 0$. This is then the motivation for the variable metric algorithm. For a detailed discussion of the actual manner in which it is carried out the reader is referred to the original paper by Fletcher and Powell[4.5].

IV FREDHOLM INVERSION

For the most part the procedures involved with this type of analysis have been adequately outlined in chapter 5, and the references given therein. The implementation of the constraints on the solution is, however, somewhat more involved, and is not fully described in the references.

Lawson and Hanson provide a routine "NNLS", which is designed for minimizing a sum of squares under a non-negative constraint. However, this routine is not designed to handle "rank deficient" problems, and therefore it cannot be used directly on the very poorly conditioned problems seen in chapter 5. For this reason the procedure used in chapter 5 is to first perform the singular value decomposition on the original problem in order to obtain a reduced problem such as (5.8). At that point the least squares problem to be solved is of the form:

$$R^{(m)} \underset{\sim}{y}^{(m)} \cong \underset{\sim}{g}^{(m)} \qquad \underset{\sim}{y}^{(m)} = K^T \underset{\sim}{x} \quad \underset{\sim}{x} > 0. \tag{A.6}$$

In this $R^{(m)}$ is an m x m diagonal matrix and m is the selected pseudo-rank. By appropriate selection of the pseudo-rank this system will be sufficiently well conditioned as to allow its use with a least squares algorithm designed for full rank problems. Unfortunately, however, at this point the constraints of non-negativity for x have been transformed into the inequality constraint $K^{(m)} \underset{\sim}{y}^{(m)} > 0$. Thus equation (A.6) defines a problem of the form LSI in the notation of

Lawson and Hanson. Chapter 23 of reference 5.7 describes how this problem may be rewritten in terms of a "Least Distance Programming" problem, and appendix C of this reference provides a subroutine for the solution of such problems.

This, then, is the procedure used for the computation of constrained solutions in chapter 5. However, as pointed out in that chapter, the algorithm used in the subroutine provided by Lawson and Hanson, while mathematically rigorous, is not numerically robust and therefore in future work perhaps a more robust algorithm should be employed.

REFERENCES

CHAPTER 1

1.1) W. Klement Jr., R. H. Willens, and P. Duwez, Nature 187, 869 (1960).

1.2) B. D. Cullity, Elements of X-ray Diffraction, second edition, Addison-Wesley, Reading, Mass. (1978).

1.3) A. Williams, Ph.D. Thesis, California Institute of Technology, Pasadena, Ca. (1981).

1.4) G. S. Cargill III, J. Appl. Phys. 41, 12 (1970).

1.5) J. D. Bernal, Nature 185, 68 (1960).

1.6) D. S. Boudreaux, and H. J. Frost, Phys. Rev. B23, 1506 (1981).

1.7) R. B. Schwarz, and W. L. Johnson, Phys. Rev. Lett. 51, 415 (1983).

1.8) P. H. Gaskell, J. Non-cryst. Sol. 32, 207 (1979).

1.9) C. L. Briant, and J. J. Burton, Phys. Stat. Sol. b85, 393 (1978).

1.10) D. R. Nelson, Phys. Rev. B28, 5515 (1983).

1.11) H. S. Chen, in Amorphous Metallic Alloys, ed. by F. E. Luborsky, Butterworths, London, Engl. (1983).

1.12) S. Steeb, and P. Lamparter, J. Non-cryst. Sol. 61, 237 (1984).

1.13) P. Fuoss, P. Eisenberger, W. K. Warburton, and A. Bienenstock, Phys. Rev. Lett. 46, 1537 (1981).

CHAPTER 2

2.1) C. G. Barkla, and C. A. Sadler, Phil. Mag. 16, 550 (1908).

2.2) C. G. Barkla, and C. A. Sadler, Phil. Mag. 17, 739 (1909).

2.3) W. L. Bragg, Proc. Camb. Phil. Soc. 17, 43 (1913).

2.4) M. Siegbahn, Spectroscopy of X-rays, translated by G. A. Lindsay, Oxford Univ. Press, Oxford, Engl. (1925).

2.5) W. Kossel, Z. Physik 1, 119 (1920).

2.6) D. Coster, Z. Physik 25, 83 (1924).

2.7) D. Coster, and J. H. Van der Tuuk, Nature 117, 586 (1926).

2.8) R. de L. Kronig, Z. Physik 70, 317 (1931).

2.9) R. de L. Kronig, Z. Physik 75, 468 (1932).

2.10) A. I. Kozlenkov, Bull. Acad. Sci. U.S.S.R. Phys. Ser. 22, 968 (1961).

2.11) A. I. Kozlenkov, Bull. Acad. Sci. U.S.S.R. Phys. Ser. 28, 794 (1964).

2.12) H. Hall, Rev. Mod. Phys. 8, 358 (1936).

2.13) E. Merzbacher, Quantum Mechanics, second edition, Wiley, New York, N. Y. (1970).

2.14) J. J. Boland, S. E. Crane, and J. D. Baldeschwieler, J. Chem. Phys. 77, 142 (1982).

2.15) P. Eisenberger, and B. Lengeler, Phys. Rev. B22, 3551 (1980).

2.16) International Tables for X-ray Crystallography Vol. III sec. 3.2, ed. by N. F. M. Henry, and K. Lonsdale, Kynoch Press, Birmingham Engl. (1952).

2.17) C. De Boor, A Practical Guide to Splines, Springer Verlag, New York, N. Y. (1978).

2.18) J. J. Boland, F. G. Halaka, and J. D. Baldeschwieler, Phys. Rev. B28, 2921 (1983).

2.19) W. H. McMaster, N. Ker Del Grande, J. H. Mallet, and J. H. Hubbel, Compilation of X-ray Cross Sections, National Technical Information Service, Springfield, Va. (1969).

2.20) F. Schmuckle, P. Lamparter, and S. Steeb, Z. Naturforsch. 37a, 572 (1982).

2.21) P. A. Lee, P. H. Citrin, P. Eisenberger, and B. M. Kincaid, Rev. Mod. Phys. 53, 249 (1981).

2.22) A. V. Oppenheim, and R. W. Schaffer, Digital Signal Processing, Prentice Hall, Englewood Cliffs, N. J. (1975).

2.23) P. Eisenberger, and G. S. Brown, Sol. Stat. Comm. 29, 481 (1979).

2.24) E. D. Crozier, and A. J. Seary, Can. J. Phys. 58, 1388 (1980).

2.25) B. K. Teo, H. S. Chen, R. Wang, and M. R. Antonio, J. Non-Cryst. Sol. 58, 249 (1983).

2.26) L. V. Azaroff, X-ray Spectroscopy, McGraw Hill, New York, N. Y. (1974).

CHAPTER 3

3.1) P. Pietrokowsky, Rev. Sci. Instr. 34, 445 (1963).

3.2) "METADI" diamond polishing compound, manufactured by Buehler Ltd. Evanston Ill. 60204.

3.3) see ref. 2.21).

3.4) E. A. Stern, and K. Kim, Phys. Rev. B23, 3781 (1981).

3.5) A. Williams, Rev. Sci. Instr. 52, 193 (1983).

3.6) J. A. Bearden, Rev. Mod. Phys. 39, 78 (1967).

3.7) G. S. Knapp, and P. Georgopolos, in Laboratory EXAFS Facilities-1980, ed. by E. A. Stern, A.I.P. Conf. Proc. No. 64 (1980).

3.8) Useful references for this procedure are the following:

a). S. I. Salem, and P. L. Lee, Atomic Data and Nuclear Data Tables 18, 233 (1976).

b). S. I. Salem, and C. W. Schultz, Atomic Data 3, 215 (1979).

c). G. C. Nelson, B. G. Saunders, and S. I. Salem, Atomic Data 1, 378 (1969).

3.9) J. J. Spokas, and R. D. Meeker, Med. Phys. 7, 135 (1980).

3.10) F. Comin, L Incoccia, and S. Mobilio, J. Phys. E16, 83 (1983).

CHAPTER 4

4.1) W. G. Moffatt, Handbook of Binary Phase Diagrams, General Electric Co., Schenectady, N. Y. (1978)

4.2) W. H. Shull, D. G. Naugle, S. J. Poon, and W. L. Johnson, Phys. Rev. B18, 3263 (1978).

4.3) B. K. Teo, and P. A. Lee, J. Amer. Chem. Soc. 101, 2815 (1979).

4.4) B. Lengeler, and P. Eisenberger, Phys. Rev. B21, 4507 (1980).

4.5) R. Fletcher, and M. J. D. Powell, Comput. J. 6, 163 (1963).

4.6) E. A. Stern, B. A. Bunker, and S. M. Heald, Phys. Rev B21, 5521 (1980).

4.7) P. Rabe, G. Tolkiehn, and A. Werner, J. Phys. C12, 899 (1979).

4.8) D. V. Baxter, A. Williams, and W. L. Johnson, J. Non-Cryst. Sol. 61, 409 (1984).

CHAPTER 5

5.1) Yu. A. Babanov, V. V. Vasin, A. L. Ageev, and N. V. Ershov, Phys. Stat. Sol. b105, 747 (1981), Phys. Stat. Sol. b108, 103 (1981).

5.2) J. N. Franklin, Math. Comput. 28, 889 (1974).

5.3) A. N. Tikhonov, and Y. Y. Arsenin, Solutions of Ill-posed Problems, translated by F. J. Washington, Halsted Press, New York, N. Y. (1977).

5.4) R. L. Parker, Ann. Rev. Earth Planet. Sci. 5, 35 (1977).

5.5) K. Unruh, private communication.

5.6) L. E. Hazelton, private communication.

5.7) C. L. Lawson, and R. J. Hanson, Solving Least Squares Problems, Prentice Hall, Englewood Cliffs, N. J. (1974).

5.8) R. J. Hanson, private communication.